UNIVERSITÀ DEGLI STUDI DI PADOVA

Head Office: Università degli Studi di Padova

Department of Chemical Sciences

Ph.D. COURSE IN: Science and Engineering of Materials and Nanostructures (SIMN)

SERIES XXXV

Preparation of PVDF/TiO_2 core/shell nanofibrous membranes and investigation of piezo-potential effect on the photocatalytic performance

The thesis is written with the financial contribution of China Scholarship Council (CSC)

Coordinator: Prof. Giovanni Mattei
Supervisor: Prof. Michele Modesti
Co-Supervisor: Prof. Martucci Alessandro

Ph.D. student: Jiayi Yin

Abstract

Piezo-photocatalysis, combining piezoelectricity with photocatalysis, is considered as a novel strategy to improve photocatalytic efficiency. A piezo-potential is generated on a piezoelectric material under strain, which accelerates the movement of photogenerated electrons and inhibits the recombination between photogenerated charge carriers. In addition, the piezoelectric field as a kind of built-in electric field is not easy to be screened by the chargers and it has an infinite promoting effect on photocatalysis due to the oscillatory external strain. This thesis aims to investigate the effect of piezo-potential on photocatalytic performance of hybrid PVDF/TiO_2 core/shell nanofiber membrane.

The thesis is divided into three parts: introduction, experimental investigation, and conclusions, as shown in the graphical abstract. Within the experimental investigation, a detailed study of the piezoelectric properties of electrospun PVDF nanofiber membrane has been carried out at the beginning, subsequently, the preparations of PVDF/TiO_2 core/shell nanofiber membranes have been accomplished according to three different approaches, and finally, the piezo-photocatalytic activities of the PVDF/TiO_2 core/shell nanofiber membrane have been evaluated.

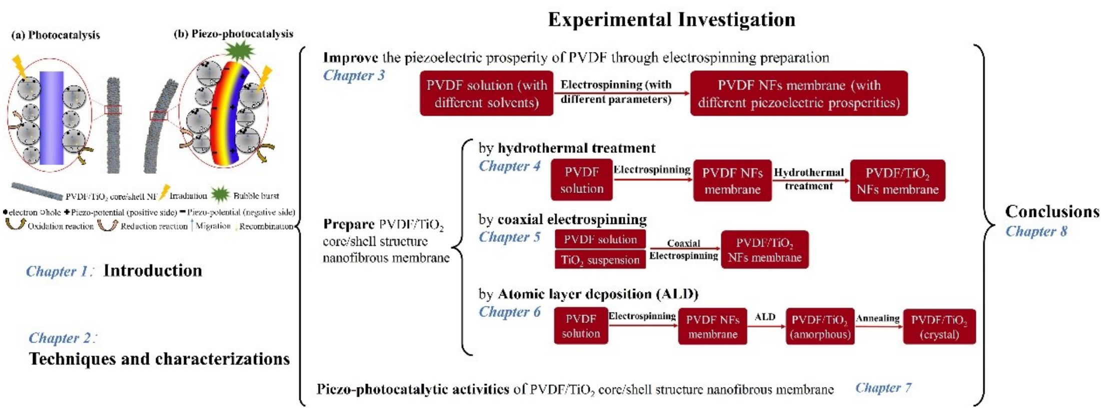

Graphical abstract of this thesis.

In Chapter 1, photocatalysis and piezoelectricity have been introduced first to build a background from fundamentals and challenges to applications. Then, the effect of the built-in potential of piezo-photocatalyst on photocatalytic activity has been illustrated comprehensively, and the development of piezo-photocatalysts from integrated to hybrid piezo-photocatalysts has been introduced. In the end, a hybrid PVDF-TiO_2 core-shell nanofiber membrane has been proposed as a piezo-photocatalyst.

Sample preparation techniques and main characterizations used in the thesis are introduced in Chapter 2.

The piezoelectric properties of PVDF cast films have been intensively studied, indicating that solvents with higher dipole moments can endow PVDF cast films with higher piezoelectric properties. The effects of solvent and electrospinning parameters on morphology and piezoelectric properties of PVDF nanofibrous membranes are studied, as detailed in Chapter 3.

Hydrothermal treatment is a convenient method to synthesize TiO_2 semiconductor, but conventional hydrothermal treatment always requests a high temperature and a long treating time to obtain TiO_2 with good morphology and high crystallinity, which could damage the polymeric support (PVDF electrospun membrane). Chapter 4 has introduced a PVDF/TiO_2 core/shell composite nanofibrous membrane (CNM) obtained by microwave-assisted hydrothermal treatment on an electrospun PVDF membrane. The effects of hydrothermal process parameters (solution, heating temperature, and treatment time) on the structure (morphology, crystal, etc.) and photocatalytic properties of PVDF/TiO_2 CNM have been investigated.

To achieve high photocatalytic efficiency of TiO_2, commercial TiO_2, P25 (80% anatase and 20% rutile), is applied to prepare PVDF/TiO_2 CNM. In Chapter 5, the PVDF/TiO_2 core/shell nanofiber membrane has been prepared by coaxial electrospinning adopting PVDF solution and TiO_2 (P25) suspension as core and shell feeds, separately. The effects of coaxial electrospinning parameters (solvent and TiO_2 concentration in shell suspension, as well as the feed rates of PVDF and TiO_2 solutions) on the morphology, property, and photocatalytic performance of PVDF/TiO_2 CNMs have been investigated.

In Chapter 6, atomic layer deposition (ALD) is applied to promote a uniform and controllable growth of a TiO_2 layer on the surface of PVDF NFs, and post-treatment annealing is employed to crystalize TiO_2. The parameters of ALD and annealing treatment have been studied to obtain the PVDF/TiO_2 CNM with the optimal properties, and the effect of TiO_2 thickness on the photocatalytic activity of PVDF/TiO_2 CNM has been investigated.

Three types of PVDF/TiO_2 core/shell nanofiber membranes prepared via the aforementioned approaches are compared in Chapter 7. The PVDF/TiO_2 core/shell nanofiber membrane prepared by coaxial electrospinning has shown excellent photocatalytic efficiency and economic preparation, which consequently has been used to investigate piezo-photocatalysis.

A summary of the thesis and an outlook for future work on piezo-photocatalysis are reported in Chapter 8.

Acknowledgments

First, I would like to thank my supervisor Prof. Michele Modesti and co-supervisor Prof. Martucci Alessandro for giving me the opportunity to start a doctoral life at the University of Padova and for all the support I received throughout the three-year study.

I would like to express my appreciation to Assoc. Prof. Martina Roso, who assisted me with my experiments and results. Without her help, I am afraid my Ph.D. study would be more difficult.

Then, I wish to express my thanks to all the members of Polymer Engineering Group (PEG), the group of Prof. Modesti. They helped me to adapt to a new life, taught me to use various instruments, gave me a lot of help in experiments and life, and organized interesting activities. To me, they are more like friends than colleagues.

I would also like to appreciate the researchers who helped me with some experiments and characterizations, especially Dr. Chuanyu Sun.

Thanks for the opportunity and financial support provided by China Scholarship Council (No. 201908440509).

I would like to thank Dr. Guilhem Rival, my mentor during my 4-month study at INSA Lyon, for helping me to gain a better understanding of piezoelectric effect. I am grateful to all the members of LGEF for their help. I had a fulfilling and comfortable period there.

I also want to thank all my friends I met in Padova and Lyon for their help and company. I will remember all the wonderful times that we had.

I would like to appreciate my family for all the support and help they gave to me. I also want to thank the "ocean" who companied and cared me.

In the end, I really want to appreciate myself for the growth and progress I did. Keep up the good work and life in the future!

Jiayi Yin

28/09/2022

Table of content

Chapter I Introduction

1.1 Photocatalysis and photocatalyst

Photochemistry refers to the chemical changes caused by absorbed light. Photosynthesis is a typical natural photochemistry, green leaf generated carbohydrates and oxygen after absorbing the blue and red components of sunlight, which is the basis of human life. The foundations of semiconductor photochemistry were laid by Gerischer, Pleskov, et al. in the 1960s[1], and the light-driven reactions were studied on well-defined bulk monocrystalline semiconductors then. Later, solar cells composed of semiconductors (mainly single crystals) and redox electrolytes were developed. The possibility of using illuminated semiconductor/electrolyte junctions to split water was explored by Fujishima and Honda in 1972.[2] However, the demands for high efficiency and long-term chemical stability restricted the development of photochemistry. In 1991, O'Regan and Grätzel reported a work about mesoporous dye-sensitized solar cells.[3] Since then, photochemistry has progressed from well-defined single crystal bulk materials to high surface area nanostructured electrodes. By now, the study of nanostructured semiconductors is still a hot field of photochemistry.[4]

Catalysis is a phenomenon in which a catalyst accelerates the rate at which a chemical system reaches equilibrium without being consumed. Photocatalysis is a combination of photochemistry and catalysis that occurs in the presence of light and photocatalysts. Semiconductors can be excited by light energy and act as photocatalysts to accelerate the reaction rate.

The discovery of TiO_2 as a photocatalyst for water splitting by Fujishima and Honda was a remarkable start in the field of photocatalysis.[2] Since then, semiconductors with appropriate electronic structures (e.g., TiO_2, ZnO, Fe_2O_3, CdS, and ZnS) have been widely adopted as photocatalysts for various applications.[5]

Photocatalysis is initiated by absorbed photons with energy equal to or higher than the bandgap energy of the photocatalyst. As shown in Figure 1.1, an electron (e^-) jumps from the valence band (VB) to the conduction band (CB) under irradiation in femtoseconds, leaving an unfilled place namely hole (h^+) in the VB. e^- and corresponding h^+ are called electron-hole pair. When these electrons and holes are somehow trapped on the semiconductor surface, they undergo reduction and oxidation reactions with absorbed pollutant or molecule (called direct photocatalysis) or absorbed O_2 or H_2O to produce reactive oxygen species (ROS), which react with pollutant or molecule (called indirect photocatalysis). To gain a clear understanding of the photocatalytic mechanism, a series of reactions are postulated:

Photoexcitation:	$Semiconductor + hv \rightarrow e_{CB}^- + h_{VB}^+$	(1.1)
Entrapment of electron:	$e_{CB}^- \rightarrow e_{TR}^-$	(1.2)
Entrapment of hole:	$h_{VB}^+ \rightarrow h_{TR}^+$	(1.3)
Recombination of electron-hole pair:	$e^- + h^+ \rightarrow heat$	(1.4)
Generation of ROS:	$O_2 + e^- \rightarrow O_2^{\cdot -}$	
	$O_2^{\cdot -} + e^- + 2H^+ \rightarrow H_2O_2$	
	$O_2^{\cdot -} + H_2O_2 \rightarrow {}^{\cdot}OH + OH^- + O_2$	
	$H_2O_2 + e^- \rightarrow {}^{\cdot}OH + OH^-$	
	$H_2O + h^+ \rightarrow H^+ + {}^{\cdot}OH$	
	$OH^- + h^+ \rightarrow {}^{\cdot}OH$	
	$2{}^{\cdot}OH + h^+ \rightarrow H_2O_2$	(1.5)

In equation (1.5), the ROS are generated in based forms (eg. $O_2^{\cdot -}$ H_2O_2, ${}^{\cdot}OH$) and other forms through various routes according to special photocatalytic reactions.

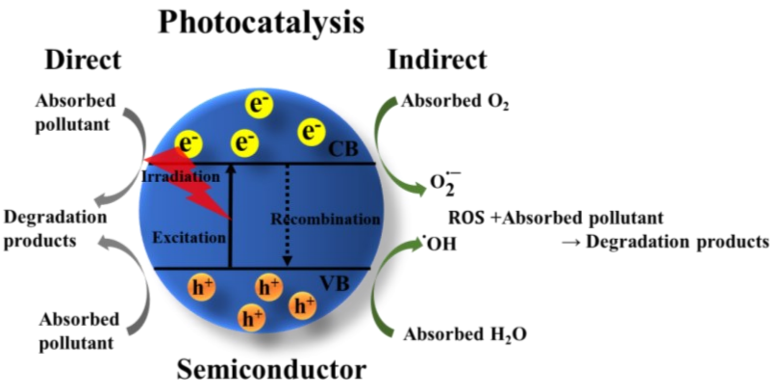

Figure 1.1 General mechanism of photocatalytic pollutant degradation.

Photocatalysis as a popular and practical technology has attractive features: 1). Photocatalysis occurs at ambient temperature and pressure; 2). Only light and oxygen are required, both of which are easily obtained from solar irradiation and air; 3). The final degradation products are environmentally friendly, like H_2O, CO_2, and other inorganic substances; 4). Photocatalysts are durable and reusable.

However, some features of photocatalysts limit their development: 1). The recombination rate of electron-hole pairs is high; 2). Reaction products are produced in close proximity (on the surface of the small particle), which makes it easy for reverse reactions of intermediate chemical species to occur; 3). Semiconductor photocatalysts are prone to agglomeration, resulting in reduced surface reaction sites; 4). Most photocatalysts are wide-bandgap semiconductors that are sensitive to UV light, which only accounts for 5% of solar energy. 5). The powdered catalysts after applications, especially in a liquid environment, are difficult to recover and reuse. The first three features are the reasons for the limited photocatalytic efficiency of most photocatalysts.

1.1.1 Strategies to enhance the photocatalytic performance

Considering the advantages and disadvantages of photocatalysts, various strategies, mainly to increase the reactive sites and control the band-edge potential, are investigated by researchers to enhance the photocatalytic activity.[6,7]

1.1.1.1 Morphology

The morphology of semiconductors, including size, shape, geometry, texture, etc., affects the catalytic efficiency from various aspects, such as surface area, active site, optical property, electron transport, and crystal orientation. In general, the smaller the particle size, the larger the surface area, the more active sites per volume (or mass), the shorter the distance for photogenerated charge carriers to reach the surface reaction sites, the higher the irradiation absorbance, but also the higher the recombination rate of electron-hole pairs, the smaller bending of band structures. Therefore, regarding the morphology of particles, both positive and negative effects need to be considered.

TiO_2 is one of the most investigated catalysts, and its morphology has been altered (partial results are shown in Figure 1.2) to study the effect of morphology on catalytic efficiency. Koci et al.[8] investigated the effect of TiO_2 nanoparticles size in the range of 4.5 to 29 nm on CO_2 reduction and found that TiO_2 nanoparticles with size of 14 nm as the optimum size exhibited the highest yield of CH_4 and CH_3OH. Xu et al.[9] reported that TiO_2 nanosheets were 5.8-fold more efficient than cuboids in photocatalytic reduction of CO_2 to CH_4 due to higher surface area. Macak et al.[10] demonstrated that the high-aspect-ratio TiO_2 nanotubular layers had superior photocatalytic properties compared to nanoparticle P25 layers. Other morphologies of TiO_2, such as nanorod[11] and nanowire[12], were prepared and studied, which showed excellent catalytic efficiency.

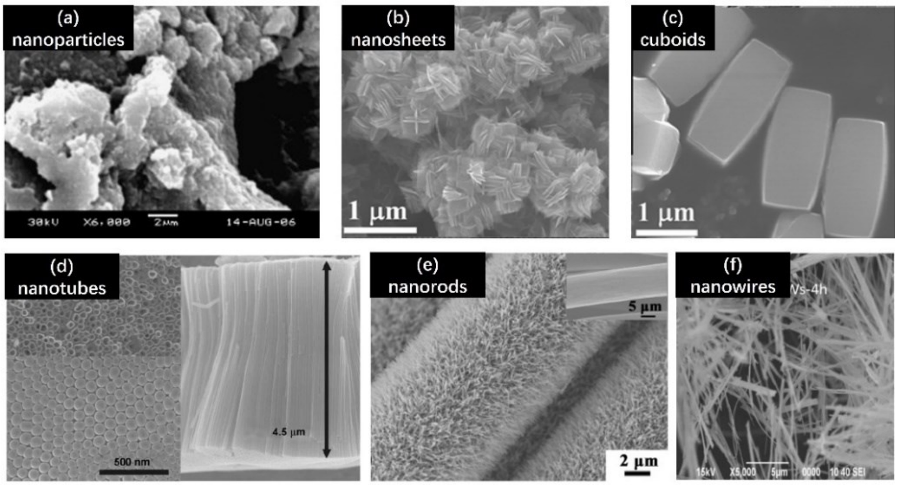

Figure 1.2 SEM image of TiO_2 (a) nanoparticles[8], (b) nanosheets[9], (c) cuboids[9], (d) nanotubes[10], (e) nanorods[11], and (f) nanowires[12].

1.1.1.2 Doping

The addition of impurities to pure substances is called doping, which is divided into cationic/metal doping (like Al, Cu, Fe) and anionic/non-metal doping (like N, S, F).[13] The crystal lattice of photocatalysts as well as their VB and CB positions change after doping with different dopants. Doping leads to a bathochromic shift, which means a decrease in bandgap or the addition of an intra-bandgap state, enabling a semiconductor to harness more photons from the visible light of solar insolation. Compared with mono-doped semiconductors, co-doping is more attractive because it could result in higher photocatalytic activity and more beneficial characteristics. The band structures of semiconductors before and after doping in three ways are summarized in Figure 1.3.[7]

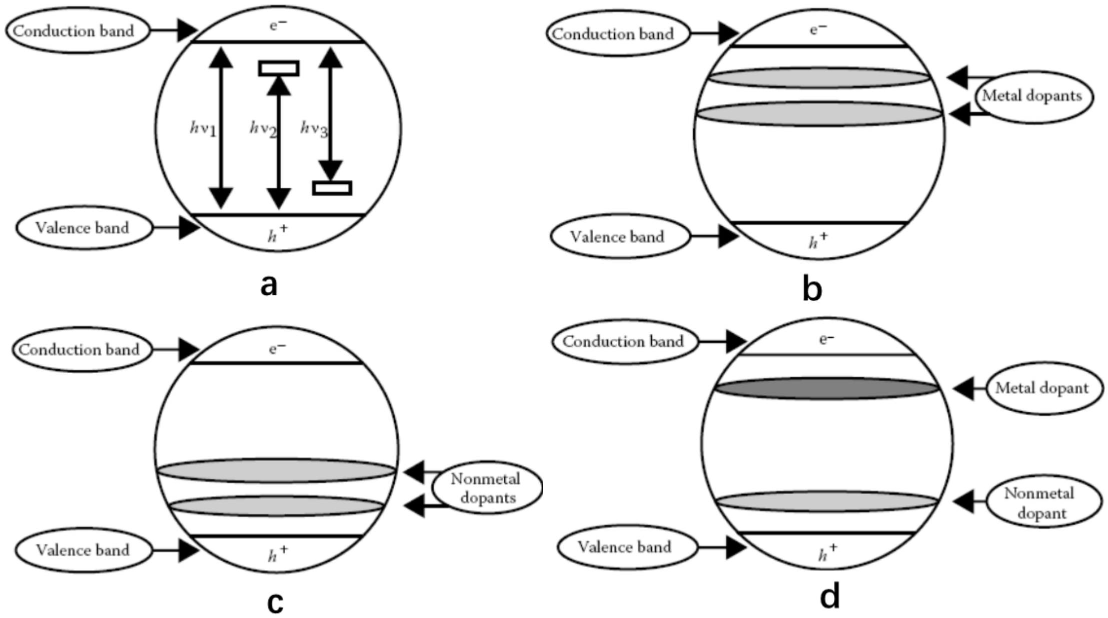

Figure 1.3 Band structure of photocatalyst (a) barely, with (b) metal dopant, (c) non-metal dopant, and (d) metal-nonmetal co-dopant. (hv_1, hv_2, and hv_3 represent the bandgap for bare, metal-doped, and nonmetal-doped semiconductors, respectively.) [7]

Cu, Fe, and Al were adopted to dope TiO_2 by dip coating method[14]. After comparing the optical absorption spectra of the non-doped and metal-doped TiO_2 films, narrowing bandgaps were observed in Fe- and Cu-TiO_2 films. Meantime, the Cu-TiO_2 film was effective for visible-light photocatalysis, while Fe- and Al- TiO_2 films hardly showed visible-light photocatalytic activity.

1.1.1.3 Coupled with semiconductor

Coupling semiconductors with different band positions can generate a built-in field in the interface, which promotes interfacial charge transfer and suppresses electron-hole pair recombination. Each type of semiconductor composite has its own electrons or holes transition between semiconductors depending on band structures, as shown in Figure 1.4.[6] For the first three methods in Figure 1.4(a-c), electrons or holes transition to sites with lower reduction or oxidation potential, thereby reducing the redox potential of hybrid composites. The Z-scheme and vectorial electron transfer process in 1.4(d-f) are popular methods because they increase the redox potential.

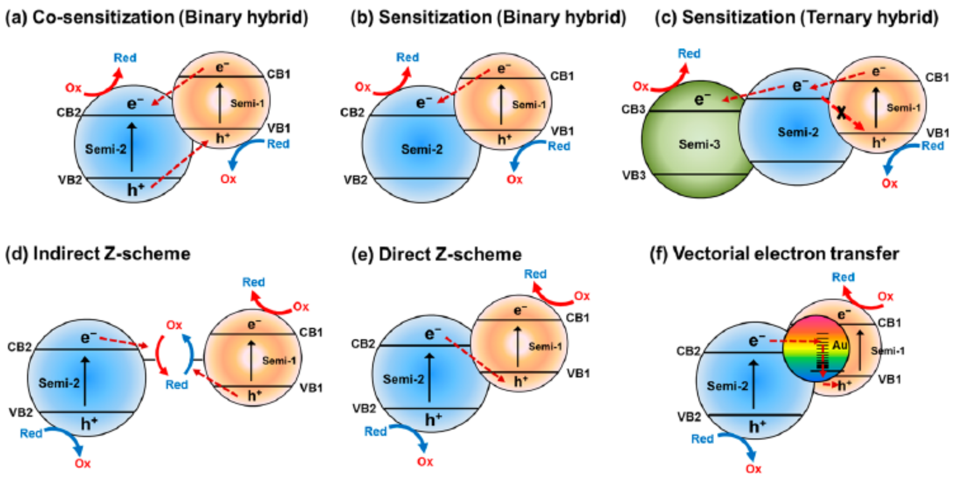

Figure 1.4 Schematics of electron transfers in semiconductor composite systems.[6]

CdS and TiO_2 form a Z-scheme system, which has attracted much attention as a catalyst. CdS is irradiated with light of lower energy than TiO_2 particles, then the photogenerated electrons can transit from CdS to TiO_2, while holes remain in CdS. Hence, the photocatalytic efficiency can be increased, and wide illumination can be utilized. When CdS quantum dots were combined with TiO_2, it was reported that the short circuit photocurrent was increased from 0.22 to 7.82 mA/cm^2 and the cell efficiency was as high as 4.15%[15], the efficiency of the incident photon to charge carrier was doubled[16], etc.

1.1.1.4 Dye sensitization

Most photocatalysts are only sensitive to UV light due to the wide bandgap, whereas visible light is the major portion of solar light. Dye sensitization mainly focuses on improving the light absorption and extending the light absorption range (from UV to visible) of semiconductors. Among various dyes with redox properties and visible light sensitivity, ruthenium (II) complexes with metal porphyrins have been widely utilized as sensitizers. When the dyes are exposed to visible or solar light, they can inject electrons to the CB of semiconductors, starting a catalytic reaction quickly and efficiently.

Ru^{II}(2,2'-bipyridyl-4,4'-dicarboxylate)$_2$-(NCS)$_2$ (N3 dye) adsorbed Cu(0.5 wt%)-Fe(0.5 wt%)/TiO_2 catalyst was prepared and photocatalytically produced methane under concentrated natural sunlight.[17] The methane production rate was improved from 0.281 to 0.617 μmol/g-cat h after N3 dye decoration and the excellent photoactivity of the N3 dye adsorbed TiO_2 catalyst was ascribed to its full visible light absorption.

1.1.2 Applications

1.1.2.1 Degradation of organic contaminants

Photocatalysis has obvious effects on degrading various organic contaminants. Photogenerated electrons, holes, and ROS degrade pollutants through redox processes, as shown in Figure 1.1. If photocatalysis results in a complete degradation of contaminants and the final products are CO_2, H_2O, or ionized halides, this photocatalysis is called mineralization. In most cases, organic pollutants are only degraded into compounds with smaller molecule weight and less toxicity. Therefore, the mineralization of organic contaminants into environmentally friendly products is the goal that should be pursued in the field of photocatalytic degradation.[18]

It should be emphasized that during the photodegradation of organics, light energy is possible to break C-H and C-O bonds, resulting in the degradation of pollutants to a certain extent. Therefore, it is necessary to evaluate whether a photoreaction on new material is a photocatalytic process, a simple redox reaction, or a light-induced chemical reaction.

1.1.2.2 Water splitting

Photocatalytic water splitting has received extensive attention due to the economic and environmental benefits of harnessing solar energy to produce the clean fuel H_2.[19] Photogenerated electrons, holes, and ROS undergo oxidation and reduction with water molecules to produce O_2 and H_2. Thermodynamically, the overall water splitting reaction is an uphill reaction with a large positive change in Gibbs energy (ΔG^0 = 238 kJ mol^{-1}). Therefore, the water splitting reaction is an energy-consuming and tough process.

The current successful photocatalytic systems for overall water splitting can be divided into two primary approaches. One approach is to use a single photocatalyst with sufficient potential to split water into H_2 and O_2. In this system, the photocatalyst should have suitable band-edge positions, that is, the conduction band edge must be at higher energy than the reduction potential of hydrogen (plus overpotentials) and the energy of the valence band edge must be lower than the oxidation potential of water (plus overpotentials). The energy band diagram of common catalysts, the redox potentials of water splitting and CO_2 reduction are shown in Figure 1.5.[20] In practice, a limited number of bulk semiconductors meet the criteria for water splitting.

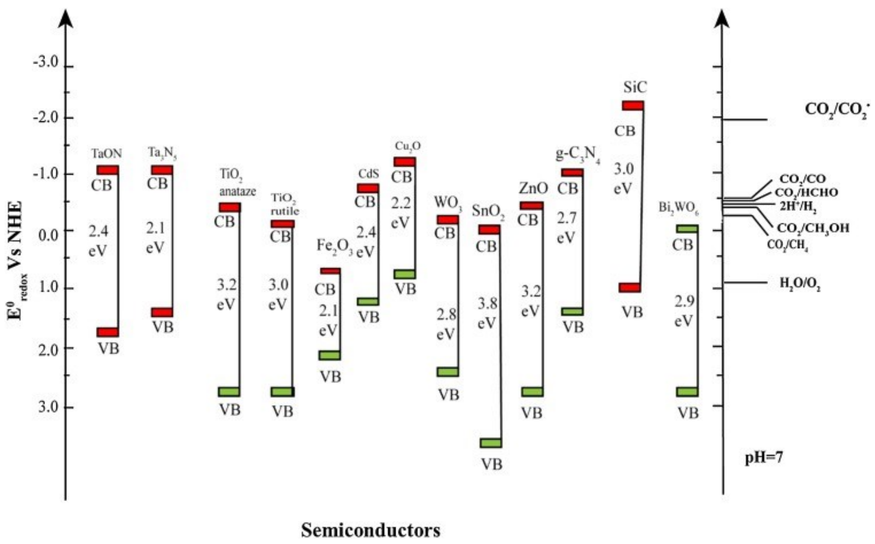

Figure 1.5 Bandgap energies of various semiconductor catalysts relative to the redox potentials at pH 7 of compounds involved in water splitting and CO_2 reduction.[20]

Another approach is to apply a two-step excitation mechanism using two different photocatalysts, one for reduction and the other for oxidation, as depicted in Figure 1.6.[6] Compared with the one-step water splitting system, the two-step system has a wider light absorption range and separates the evolving H_2 and O_2 processes. A semiconductor employed here only satisfies either the water reduction or oxidation potential for one side of the system.

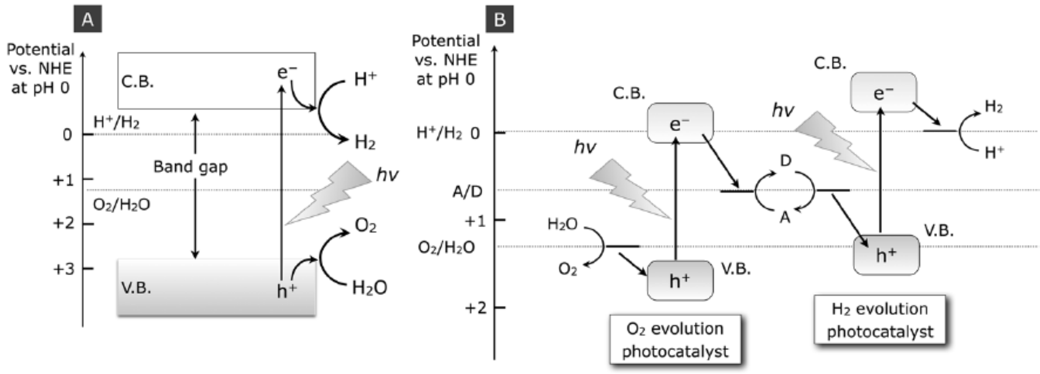

Figure 1.6 Schematic energy diagram of photocatalytic water splitting for (A) a one-step and (B) a two-step photoexcitation system.[6]

1.1.2.3 CO_2 photoreduction

Photocatalytic reduction of CO_2 into fuels and chemicals using solar energy appears to be a promising technology to curb globa1 warming, partially meet the energy requirements, and produce no toxic products or residues in the process.[21] To achieve overall CO_2 photoreduction, the energy structure of semiconductors requires that the CB must be at a more negative potential than CO_2 reduction potentials, while the top of the VB must be at a more positive potential than the H_2O oxidation potential.

In addition, photocatalytic reduction of CO_2 with H_2O into hydrocarbon fuels (like CH_4, CH_3OH) is an uphill reaction with a highly positive change in Gibbs free energy, as shown in the following equations:

$$CO_2 + 2H_2O \rightarrow CH_3OH + 3/2O_2 \ (\Delta G^0 = 702.07\ kJ\ mol^{-1})$$

$$CO_2 + 2H_2O \rightarrow CH_4 + 2O_2 \ (\Delta G^0 = 818.17\ kJ\ mol^{-1})$$

Therefore, input energy is required to overcome these reaction barriers with the assistance of photocatalysts. A series of products (e.g., CO, HCHO) can be produced through various photocatalysis, depending on the number of electrons and protons involved in chemical reactions.

1.2 Piezoelectricity and piezoelectric material

When mechanical strain is applied, certain materials generate electric charges on their surfaces and the number of charges is proportional to the mechanical strain. This phenomenon is called the direct piezoelectric effect, which was discovered in quartz by the Curie brothers (Pierre and Jacques Curie) in 1880.[22] These specific materials are called piezoelectric materials and exhibit an inverse phenomenon, that is, the generated geometric strain is proportional to the applied electric field. This is defined as the converse piezoelectric effect, discovered by Gabriel Lippmann in 1881. A schematic diagram of (direct and converse) piezoelectricity is shown in Figure 1.7.[23] With the deepening understanding of piezoelectric effects, piezoelectric quartz electrometers have been brought into practical applications, and artificial piezoelectric materials have been investigated and widely used.

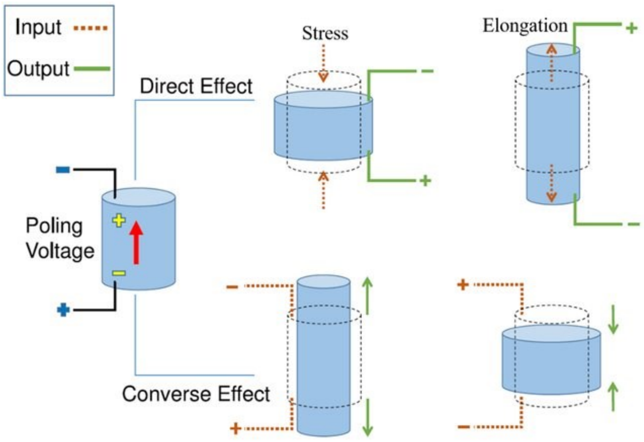

Figure 1.7 Direct and converse piezoelectric effect.[23]

To better understand piezoelectricity, it is necessary to relate it to pyroelectricity and ferroelectricity because of their interesting interrelationships in terms of crystal structure.[24] Of all 32 crystallographic classes, 21 are non-centrosymmetric, and 20 of them are piezoelectric. The 10 polar ones have pyroelectricity, meaning the spontaneous polarization of material responses to the change in temperature. Then 5 of the pyroelectric groups have ferroelectricity, which means the spontaneous polarization can be reversed by an outer electric field. Additionally, a dielectric material is an electrical insulator that can be polarized under an external electric field. Clear schematic diagrams of the classification of the 32 point groups and the relationship among dielectric, piezoelectric, pyroelectric, and ferroelectric materials are shown in Figure 1.8.

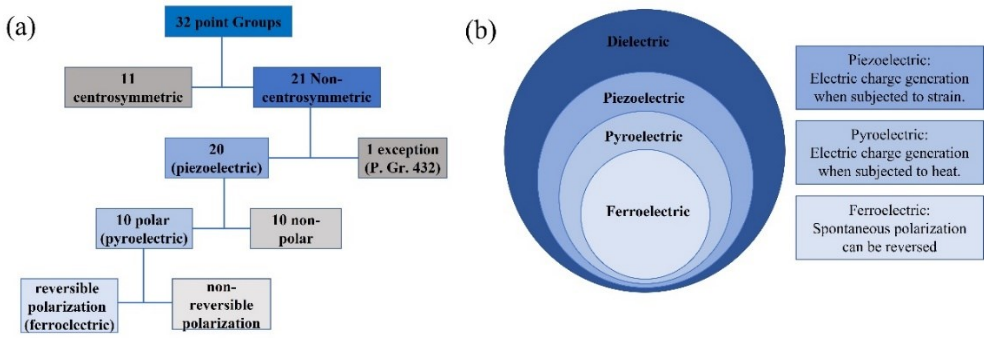

Figure 1.8 Schematic representation of piezoelectricity, pyroelectricity, and ferroelectricity based on (a) crystal symmetry and (b) the relationship.

As mentioned above, 10 of the 20 piezoelectric point groups are polar and the other 10 are non-polar. For the unit cells with polar point groups, the positive and negative charge centers are separated, and spontaneous polarization exists even without mechanical excitation. In contrast, the polarization on the unit cells with non-polar point groups is generated only under mechanical excitation.

A non-centrosymmetric crystal structure is a prerequisite for piezoelectric materials. In Figure 1.9(a), after applying an external force on one unit cell with a centrosymmetric structure, the positive and negative charge centers still overlap as without the force. Therefore, there is no net polarization (P) before or after applying force, indicating that materials with centrosymmetric crystals are non-polar and non-piezoelectric. On the contrary, for the unit cells with non-centrosymmetric crystals (in the category of materials with non-polar point groups) in Figure 1.9(b), the centers of positive and negative charges coincide when no force is applied. However, when an external force is applied, the centers of the positive and negative charges no longer coincide, and a dipole moment is produced. Thus, the overall polarization in the non-centrosymmetric crystal occurs under strain.

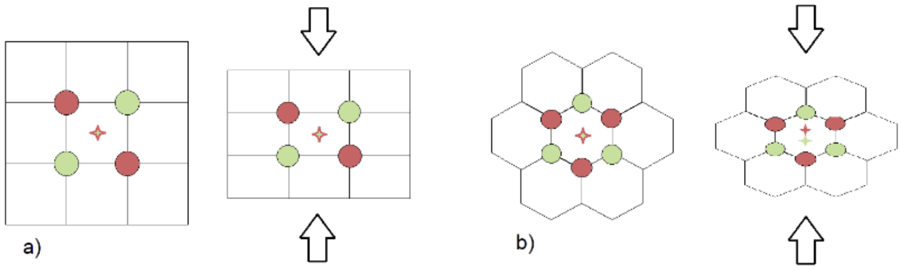

Figure 1.9 External force acting on an ionic crystal with (a) and without (b) centrosymmetric structure.[25]

For piezoelectric materials, the appearance of piezoelectricity also depends on the crystal orientation. Any region with locally uniform polarization is defined as a domain and the boundary separating two domains is called a domain wall. Single crystalline piezoelectric materials, as shown in Figure 1.10(a), have their own strongest piezoelectric properties because of the aligned dipole moments in the crystal. However, when the direction of dipole moment in each domain is random (Figure 1.10(b)), no net or low polarization appears in the material. To appear or increase the piezoelectric effect in polycrystalline piezoelectric materials, poling treatment under a strong electric field can be performed. During poling, the dipole moments in different domains move as closely as possible to the electric field direction, as shown from Figure 1.10(c) to (d). The high temperature of poling treatment promotes the movement of dipole moments, but the temperature should be below the Curie temperature, above which a material dissipates its piezoelectric properties.

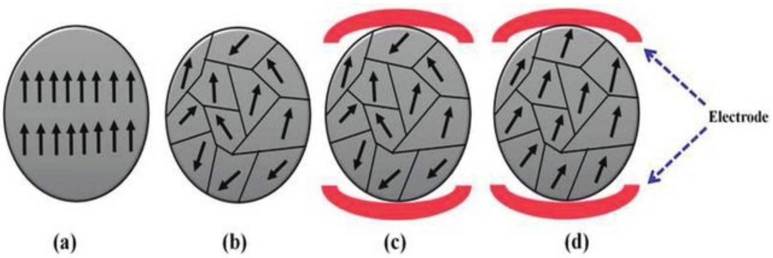

Figure 1.10 Dipole arrangement in (a) mono-crystalline and (b) poly-crystalline material. (c, d) polarization of polycrystalline material in presence of an electric field to generate piezoelectricity.[26]

1.2.1 Category of piezoelectric materials

In general, piezoelectric materials can be divided into four categories: single crystals, polycrystalline ceramics, piezo-polymers, and piezo-composites. Each category has its characteristics and is adopted in various applications. Table 1.1 shows the typical piezoelectric parameters of representative piezoelectric materials.[27]

Table 1.1 Piezoelectric properties of representative piezoelectric materials.[27]

Parameter	Quartz	$BaTiO_3$	PZT 4	PZT 5H	(Pb,Sm) TiO_3	PVDF-TrFE
d_{33} (pC/N)	2.3	190	289	593	65	33
g_{33} (10^{-3} Vm/N)	57.8	12.6	26.1	19.7	42	380
k_t	0.09	0.38	0.51	0.50	0.50	0.30
k_P		0.33	0.58	0.65	0.03	
$\varepsilon_3^X/\varepsilon_0$	5	1700	1300	3400	175	6
Q_M	$>10^5$		500	65	900	3–10
T_C (°C)		120	328	193	355	

d_{33}, g_{33}: piezoelectric constants; k_t, k_p: thickness and planar coupling factors; ε : dielectric constant; Q_M: mechanical quality factor; T_c: Curie temperature.

1.2.2.1 Single crystals

Natural or artificial single crystalline piezoelectric materials are monocrystal and have one domain with oriented dipole moments. Typical single crystals include quartz, Rochelle salt (potassium sodium tartrate tetrahydrate), ZnO, lithium niobate ($LiNbO_3$), lead magnesium niobate/lead titanate (PMN-PT), etc.[28] Single crystals are anisotropic, so the properties of specific materials are related to the cutting direction and bulk or surface wave propagation.

Quartz, a well-known piezoelectric material, exists in two forms: normal α-quartz and high-temperature β-quartz. α phase is the only piezoelectric phase, which undergoes a phase transition to β phase at 537 °C. In addition, quartz exhibits an extremely high mechanical quality factor, $Q_M > 10^5$, which enables quartz to work under large stress or high frequency. ZnO is hexagonal wurtzite and belongs to the P63mc space group. Single crystal ZnO has piezoelectricity and pyroelectricity, and its spontaneous polarization is formed along its longitudinal direction (c-axis). Whereas polycrystalline ZnO with random crystalline orientations exhibits weak or no piezoelectric properties. The point space of the $LiNbO_3$ ferroelectric phase is 3m, and its polarization direction is along the c-axis. Single crystalline PMN-PT has a large electromechanical coupling factor, which means a high conversion efficiency between electrical and mechanical energy.

Although single crystals have been very influential piezoelectric materials, they are somewhat overshadowed by polycrystalline ceramics with better piezoelectric performances.

1.2.2.2 Polycrystalline ceramics

Polycrystalline ceramics have multiple domains with aligned or random orientations of dipole moments. When the domains have different orientations of dipole moments, the materials need to be polarized to align these dipole moments, generating piezoelectricity. Perovskite-structured materials with the molecular formula ABO_3 (A is a larger metal atom and B is a smaller metal atom) are an important class of piezo-ceramics. Two-dimensional (2D) layered materials, such as transition metal dichalcogenides (TMDs), group IV monochalcogenide, group III-V buckled honeycomb, and black phosphorus, exhibit excellent piezoelectric effects due to their special 2D structure.[29]

Lead zirconate titanate (PZT, $Pb[Zr_3Ti]O_3$) has a superior piezoelectric coefficient and attracted attention in energy harvesting and storage applications.[30] However, these applications are limited by brittleness, a high Young's modulus of 50 GPa, and a maximum tensile strain of 0.2%.[30] Barium titanate ($BaTiO_3$) was first synthetized as a piezoelectric material in the early 1940s[31] and is a potential piezoelectric ceramic because of the high piezoelectric coefficient and the lack of poisonous lead. Single crystal $BaTiO_3$ also has the piezoelectric effect, much lower than the polycrystalline one. 2D layered materials have a non-centrosymmetric structure on a monolayer, and the layers are bonded by van der Waals force. Taking MoS_2 as a representative, the polarization in each Mo-S unit endows the monolayer MoS_2 with strong piezoelectricity. The non-centrosymmetry of single-layer MoS_2 may disappear when layers with opposite polarization directions are stacked, so the piezoelectricity of MoS_2 appears in odd-layers form and gradually decreases with the stacking of layers.

Although polycrystalline ceramics always exhibit excellent piezoelectric properties, their applications are easily limited by brittleness, high cost, low stability, and large electric loss, especially in high-frequency systems.

1.2.2.3 Piezo-polymers

Due to small permittivity, piezo-polymers have small piezoelectric *d* constants (electric output under stress) and large g constants (stain under electric field). Besides, piezo-polymers are lightweight, flexible, and elastic, making themselves highly responsive to water or the human body. Last but not least, piezo-polymers have a low value of Q_M, allowing for a wide resonance bandwidth.

Polyvinylidene fluoride (PVDF), the most investigated piezo-polymer, was first discovered by Kawai in 1969[32]. The d_{33} value of commercial PVDF polarized piezoelectric film has reached -20~-26 pC/N. Differing from most piezoelectric materials, PVDF has a negative d_{33} value instead of a positive one, which means that PVDF will be compressed under a positive electric field. PVDF has three common phases: α, β, and δ phases. The β phase exhibits the highest dipolar moment per unit cell and the greatest piezoelectricity due to the TTT (all-trans) planar zigzag chain conformation. PVDF-trifluoroethylene (PVDF-TrFE) has a higher piezoelectric power density (312.85 mW cm^{-3})[33] than PVDF (81.3 mW cm^{-3})[34] because TrFE monomer brings the third fluorine to the unit cell and a higher tendency to form piezoelectric β phase. Besides PVDF and its copolymers, other polymers including polyamide (PA), polylactic acid (PLA), and polysulfides also have piezoelectric effect.

Despite the relatively low piezoelectric effects, the intrinsic properties of piezo-polymers create an opportunity to overcome the shortcomings of piezo-ceramics.

1.2.2.4 Piezo-composites

Piezo-ceramics and piezo-polymers have their own characteristics for applications. To obtain piezoelectric materials with good properties in broad or specific fields, piezoelectric composite is a popular strategy because their properties can be tailored by different materials and fractions of each material.[35] When ceramics with superior piezoelectric properties are combined with polymers with mechanical flexibility, the composites that combine the merits of both materials become advanced piezoelectric materials. The geometry of two-phase composites can be classified into 10 categories according to the dimensional connectivity of each phase (as shown in Figure 1.11): 0-0, 0-1, 0-2, 0-3, 1-1, 1-2, 1-3, 2-2, 2-3, and 3-3.[36]

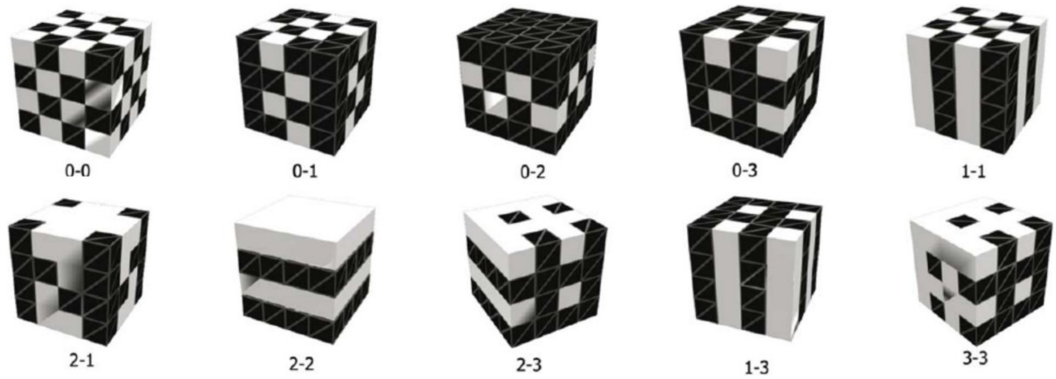

Figure 1.11 The 10 connectivity patterns in a two-phase composite.[36]

Piezo-composite can be the composite between the piezo-ceramic and piezo-polymer or non-piezoelectric polymer. The former exhibits lower piezoelectric than the latter due to the opposite sign on the piezoelectric constants.

Kitayama and Sugawara reported the first piezoelectric-based composites, made of PZT powder and PVDF, which was similar in flexibility to PVDF but had higher piezoelectric performance than PVDF.

1.2.2 Applications

Before introducing the applications of piezoelectric materials, the definitions of actuator, transducer, and sensor are given first. A transducer is any device that converts one form of energy into another. An actuator is a device that converts energy into motion or mechanical energy, so it is a specific type of transducer. When the output of a transducer is in a readable format, the transducer is called a sensor.

Piezoelectric materials as transducers are used in various fields such as daily life, industry, and marine, some of which are introduced below.

1.2.2.1 Sonar systems

Sonar plays an important role in underwater detection, underwater communication, underwater imaging, and fish detection, as shown in Figure 1.12.[37] Electrostatic transducers were originally used as sound sources and were later replaced by piezoelectric and magnetostrictive transducers, and piezoelectric transducers are generally superior in terms of efficiency and application size.

During World War I, Paul Langevin and his coworkers fabricated an ultrasonic submarine detector using quartz. Since then, the applications of piezoelectric materials in sonar systems have been developed. Piezoelectric transducers used in sonar systems can emit sound pulses, a process of converting electric energy into mechanical vibrations, and collect echoes or sounds reflected by objects, in contrast to the previous process. In general, piezo-ceramics with a high Q_M are preferred in the sonar field because of the high-power generation and no heat generation.

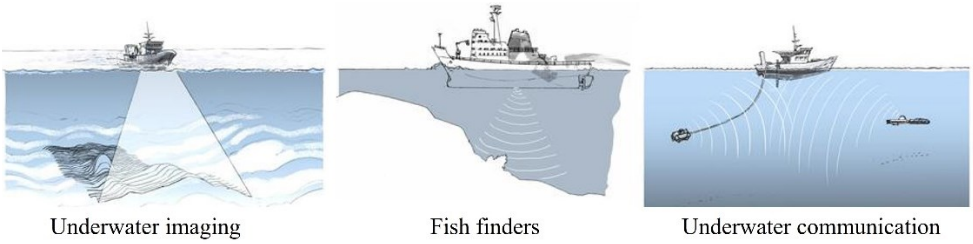

Figure 1.12 Piezo-based applications for different types of sonar systems.

1.2.2.2 Energy harvesting

Energy harvesting is a process that captures trace amounts of energy from one or more surrounding energy sources and stores the captured energy as electrical energy for later use. The energy crisis can be alleviated as more unused energy, such as vibration and human motion, is utilized. On the other hand, energy-harvesting technology can be used as a self-power source for devices with even small sizes, because conventional batteries have limited lifespans, which can stop the work of the device and cause inconvenience. Figure 1.13 summarizes some types of piezoelectric energy harvesting systems.

The piezoelectric energy harvesting process consists of three main steps: 1). Mechanical-mechanical energy transfer (piezoelectric transducers should receive the ambient energy efficiently); 2). Mechanical-electrical energy conversion (piezoelectric transducers should have a high electromechanical coupling factor); 3). Electrical-electrical energy transfer (instantaneous electrical energy should be accumulated or stored in a capacitor for later use).

Kim et al.[38] first investigated the ability to harvest electrical energy from mechanical vibrations in dynamic environments, such as an automobile engine, through a "cymbal" piezoelectric transducer. Uchino et al.[39] developed intelligent clothing (IC) with a piezoelectric energy harvesting system using flexible piezoelectric textiles as a general power source for charging portable equipment such as cellular phones, health monitoring units, or medical drug delivery devices.

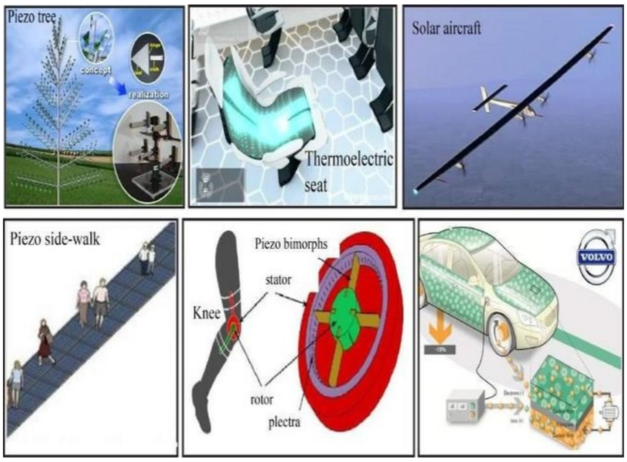

Figure 1.13 Piezo-based applications for different types of energy harvesting systems.[40]

1.3 Piezo-photocatalysis and piezo-photocatalyst

1.3.1 Piezo-photocatalysis

The foundation and characteristics of photocatalysis are mentioned in Chapter 1.1. A major feature limiting the efficiency of photocatalysts is the rapid recombination of photogenerated charge carriers. Establishing an internal electric field caused by an electrochemical potential difference in photocatalysts is a common solution to drive the charge carriers to different directions, separating the sites of oxidation and reduction reaction, and thereby enhancing the photocatalytic activity[41,42]. The methods of building internal field in photocatalysts are associated with interfaces, such as polymorph boundaries in uniform material, solution/photocatalyst interfaces, metal cocatalyst-photocatalyst junctions, and p-n junctions. However, they have limited functional scale because the electric field is saturated by charge carriers or absorbed ions, and disappears.[41]

The internal field can also arise from polarization.[43,44] The effects of the ferroelectric field on the photochemical reaction were investigated through in situ characterizations, and the results showed that the photocatalysts with a ferroelectric field exhibited higher reaction efficiency than the bare photocatalysts. Because the reduction reactions take place on the positive end of ferroelectric domains and oxidation reactions occur on domains in the opposite orientation. When $BaTiO_3$ was illuminated with UV light in an aqueous lead acetate or $AgNO_3$ solution, oxidized Pb ($Pb^{2+}\rightarrow PbO_2$) and reduced Ag ($Ag^{2+}\rightarrow Ag$) accumulated on the surfaces of domains with opposite polarization, as shown in Figure 1.14(a-c).[45] Similar research and phenomenon (shown in Figure 1.14(d-f)) have been reported in TiO_2 films coated on $BaTiO_3$ substrates.[46] These phenomena implied that the static dipolar fields in each domain separated photogenerated carriers and that the reduction and oxidation reactions occurred on spatially distinct areas of the catalyst surface.

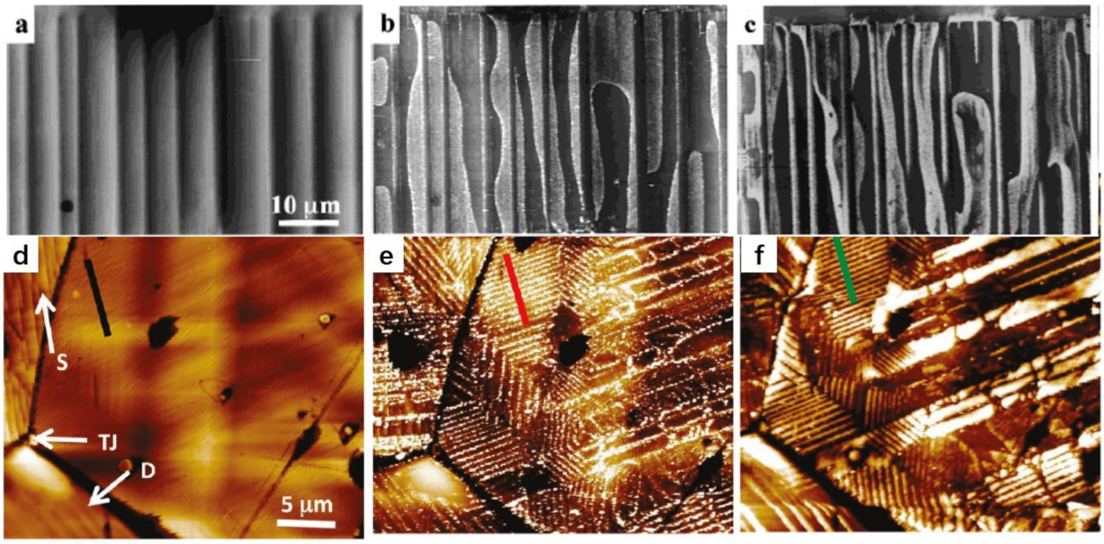

Figure 1.14 Topographic AFM images of (a-c) the {001} surface of a $BaTiO_3$ single crystal[45] and (d-f) the TiO_2 film coated on $BaTiO_3$ substrates[46]. (a, d) before the reactions, (b, e) after the reactions in an aqueous $AgNO_3$ solution, and (d, f) after the reactions in an aqueous lead acetate solution. The white contrast in (b, c, e, f) corresponds to Ag or PbO_2 deposits.

There are more piezoelectric materials than ferroelectric materials as introduced in Chapter 1.2.1. The polarization on ferroelectric materials is spontaneous, while the polarization on piezoelectric materials is generated under strain. Therefore, piezoelectric materials are widely adopted for photocatalytic activity, namely piezo-photocatalysis. Applying strain on a piezoelectric material creates a piezo-potential, which provides a driving force for photogenerated carriers to move in different directions. The piezo-potential also induces band bending at the interface of hybrid piezo-photocatalysts. In this case, the motion of electrons is accelerated while the recombination between photogenerated charge carriers is restrained, thereby enhancing the efficiency of redox reactions.

In contrast to other methods of constructing static internal fields, the piezoelectric field on piezo-photocatalysts can be altered by the amplitude of external strain and reconstructed under oscillatory stress, serving as a long-range dynamic electric field throughout the material. Therefore, piezo-photocatalysis is considered as one of the promising research topics for advanced photocatalytic activities.[47,48]

Piezo-potential is a core factor determining the piezo-photocatalytic performance and is defined as follows[48]:

$$V_p = \frac{w_x T_k d_{xy}}{\varepsilon_0 \varepsilon_{r,x}}$$

Where, V_p is the piezo-potential, w_x is the width of the piezoelectric material in the x dimension; T_k is the applied stress in the k dimension; d_{xy} is the piezoelectric moduli; ε_0 is the electrical permittivity of free space; $\varepsilon_{r,x}$ is the relative permittivity in the x dimension. From the equation, the piezo-potential is dependent on the piezoelectric property, dimension, applied external stress, and the dielectric property of the piezoelectric material.

The effect of the ferroelectric field on photocatalysis has been studied before the advent of piezo-photocatalysis, which provides tremendous support for the development of piezo-photocatalysis in this decade. Research on piezo-photocatalysis includes the discovery of piezo-photocatalysis, the development of piezo-photocatalyst, the sensibility from UV to visible light, the wide applications ranging from pollutant degradation to other complicated photocatalytic activities, etc.

1.3.2 Piezo-photocatalysts

The development of piezo-photocatalyst is the main aspect of piezo-photocatalysis research. Various piezo-photocatalysts have been proposed, and they are classified into two categories: integrated piezo-photocatalysts and hybrid piezo-photocatalysts.

1.3.2.1 Integrated piezo-photocatalysts

Integrated piezo-photocatalysts are piezoelectric materials with photocatalytic properties. The piezoelectric field generated under strain acts as a built-in electric field to facilitate the movement of electrons and suppress the recombination of charge carriers in the bulk.[47] The detailed explanation is already mentioned in Chapter 1.3.1. Generally, it is difficult for integrated piezoelectric photocatalysts, mainly piezoelectric ceramics with appropriate band gaps, to have excellent piezoelectric and photocatalytic properties at the same time.

Singh et al.[49] coupled piezoelectric, semiconducting, and photoexcited properties in $NaNbO_3$ to improve the efficiency of photocatalytic activities. The efficiencies under different experimental conditions were compared in Figure 1.15(b and c). It showed that the photodegradation rate under light and ultrasonic vibration was higher than the one under light and physical mixing, and much higher than the one without light. Besides, the photocurrent density enhanced from 0.78 to 1.02 mA/cm^2, and about an 8% improvement in the incident photon to current conversion efficiency under the piezo assistance.

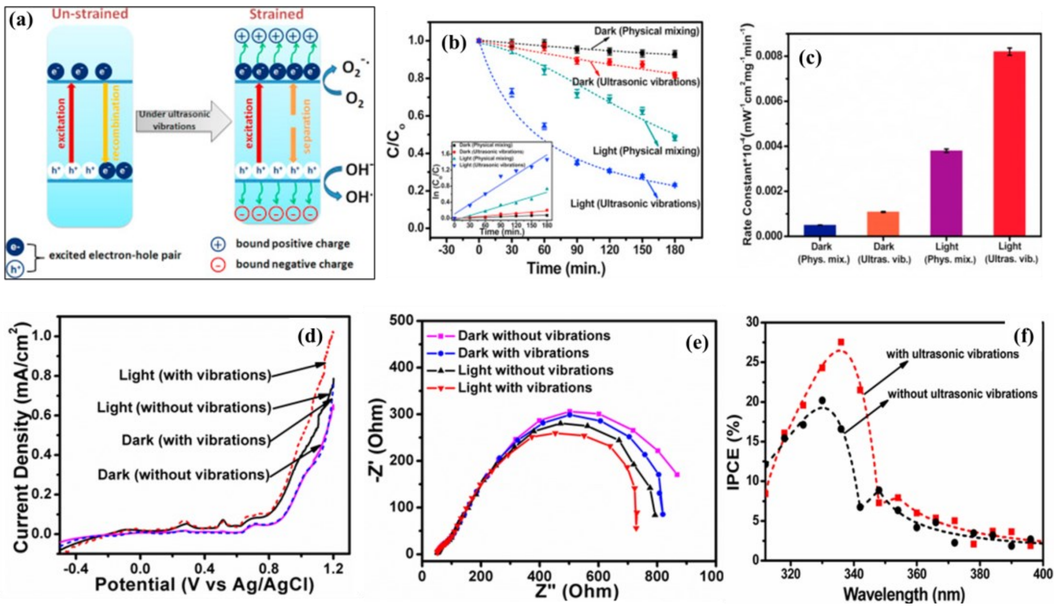

Figure 1.15 (a) Schematic diagrams showing the mechanism of the photogenerated charge carriers separation in the un-strained and strained $NaNbO_3$ nanorods, (b) photocatalytic degradation efficiency performed under different experimental conditions, Inset of Fig. (b) shows kinetics fit to the data, (c) degradation rate constants, (d) current-potential curves (e) electrochemical impedance spectra, (f) incident photon to current conversion efficiency of $NaNbO_3$ nanorods.[49]

Thakur et al.[50] synthesized uniform large-area WS_2 monolayer on Al_2O_3 substrate by chemical vapor deposition and investigated piezo-catalysis of WS_2 monolayer for bacterial disinfection and organic pollutant degradation. The MB degradation rate constants of photocatalysis, piezo-catalysis, and combined piezo-photocatalysis over the WS_2 monolayer were 0.0134 min^{-1}, 0.0171 min^{-1}, and 0.0280 min^{-1}, respectively. Xue et al.[51] grew ZnO nanowires (NWs) vertically aligned on carbon fibers, as shown in Figure 1.16. The MB degradation over ZnO NWs in piezo-photocatalysis was enhanced based on photocatalysis or piezo-catalysis due to the piezo-potential on ZnO NWs.

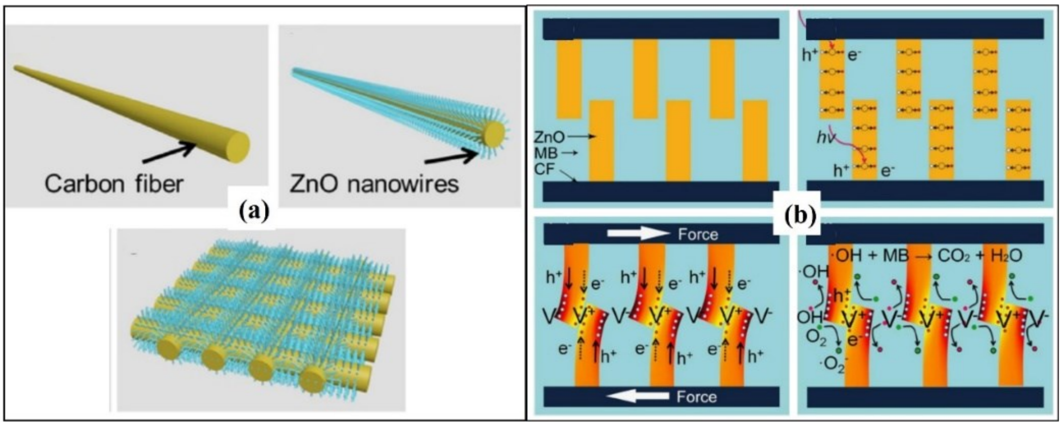

*Figure 1.16 Schematic images showing (a) the fabrication process of the woven ZnO NWs/*carbon fibers*, and (b)the working mechanism for the piezo-photocatalytic activity of ZnO NWs.*[50]

1.3.2.2 Hybrid piezo-photocatalysts

Hybrid piezo-photocatalysts consist of at least two components, namely photocatalysts and piezoelectric materials. For hybrid piezo-photocatalysts, the piezoelectric polarization on piezoelectric material provides a driving force for the movement and separation of generated charge carriers in photocatalysts[47]. And due to the piezoelectric field, band bending formed in the interface of hybrid piezo-photocatalysts can enhance the redox potential. However, there may be charge losses during transport across different materials, limiting the number of electrons and holes on the surface and inhibiting band bending.

The effect of ferroelectric material polarization on the photochemical reaction on photocatalysts has been investigated by in situ characterizations in the works of the Rohrer group.[52,53] Silver was reduced on two TiO_2 films with different thicknesses on ferroelectric $BaTiO_3$ substrates, and the silver deposit pattern in Figure 1.17(b and d) was consistent with the domain structure of the ferroelectric substrate in Figure 1.17(a and c). This meant that the dipolar fields from the domains in ferroelectric substrates penetrated the TiO_2 film and influenced the motion of the photogenerated charge carriers in TiO_2. However, the match between the Ag deposit pattern and domain structure on the 100 nm TiO_2/$BaTiO_3$ (Figure 1.17 (b)) was weaker than that on the 10 nm TiO_2/$BaTiO_3$ (Figure 1.17(d)). It can be explained that as the TiO_2 film thickness increases, the potential from the $BaTiO_3$ substrate will be screened more completely by the semiconductor, and charge carriers are less affected by the ferroelectric substrate. The Ag deposit pattern on 10 nm TiO_2/$BiFeO_3$ (Figure 1.17(h)) was correlated well with the domain structure obtained by the PFM images in Figure 1.17(e and f) instead of the topographic image in Figure 1.17(g). It is strong evidence that the polarization on substrate affects the motivation of photogenerated charge carriers in semiconductor, which contacts with ferroelectric material.

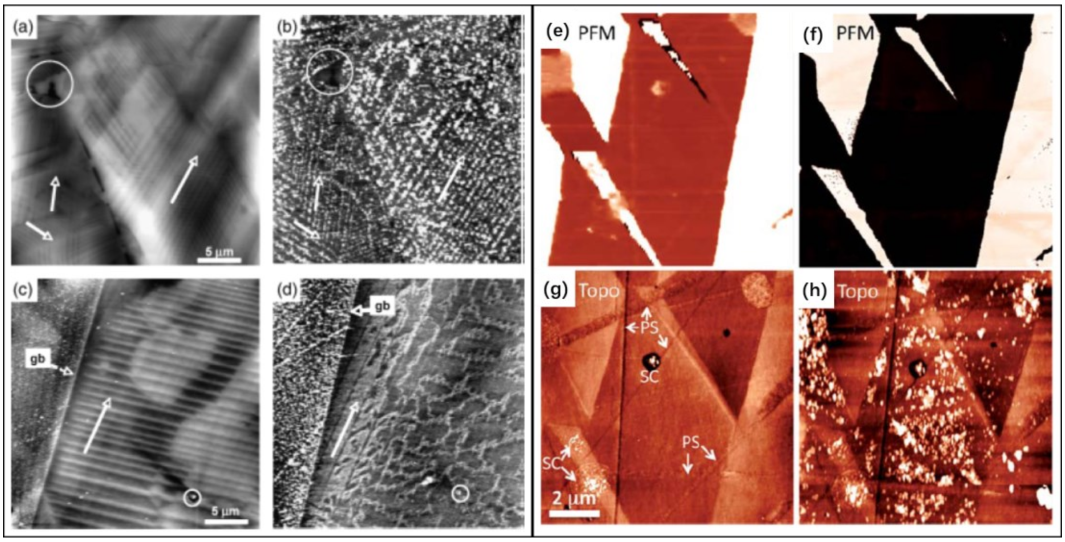

Figure 1.17 AFM images of 10 nm TiO_2 films on a $BaTiO_3$ substrate (a) before reaction, (b) after reaction, AFM images of 100 nm TiO_2 films on a $BaTiO_3$ substrate (c) before reaction, (d) after reaction.[52] PFM phase images of (e) bare $BaFeO_3$ substrate, (f) 10 nm TiO_2/$BiFeO_3$, Topographic image of 10 nm TiO_2/$BiFeO_3$ (g) before reaction, (h) after reaction.[53]

A detailed mechanistic explanation of the band bending formed at the interface of TiO_2 and $BiFeO_3$ as well as at the interface of TiO_2 and solution were also given.[53] When bulk TiO_2 was in contact with the solution, the charges flowing to the solution led to upward band bending at the interface of TiO_2 and solution. When negative (or positive) domains appear at the interface of TiO_2 and $BiFeO_3$, the energy bands of TiO_2

bent upward (or downward), as shown in Figure 1.18(a) (or Figure 1.18(b)), which promoted the transfer of holes (or charges) from TiO_2 to $BiFeO_3$ and oxidation (or reduction) reaction on TiO_2.

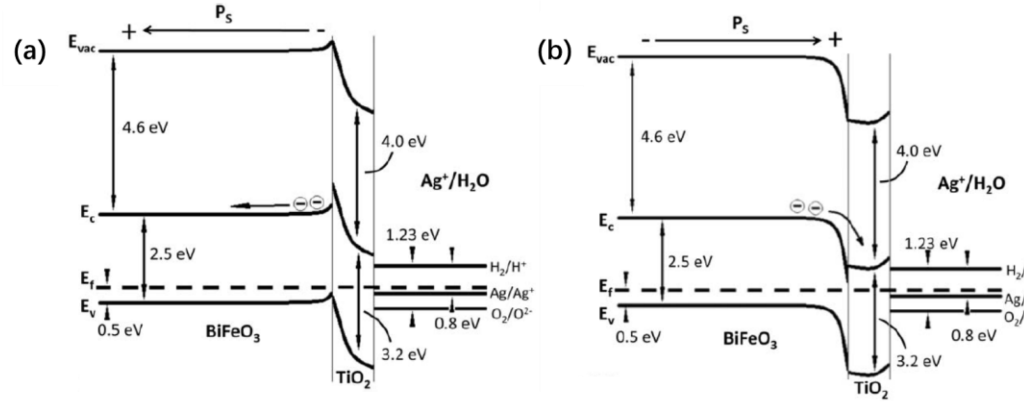

Figure 1.18 Schematics of the band structure of $BiFeO_3/TiO_2/H_2O$ with the polarization (PS) of $BiFeO_3$ (a) pointing away from $BiFeO_3/TiO_2$ interface, and (b) pointing towards $BiFeO_3/TiO_2$ interface. [53]

As described in Chapter 1.2.1, piezo-ceramics and piezo-polymers have their own characteristics as piezoelectric materials. Therefore, hybrid piezo-photocatalysts based on inorganic piezo-ceramics and organic piezo-polymers are separately introduced below.

1.3.2.3 Hybrid piezo-photocatalysts based on inorganic piezo-ceramics

When piezo-ceramics are used for hybrid piezo-photocatalysts, an obvious effect of piezo-photocatalysis can be observed due to the strong piezo-polarized field. However, the applications are inhibited due to the physical properties of ceramics, such as brittleness and difficulty in recovery.

Inoue et al.[54,55] reported that the macroscopic photocatalytic activities of a thin TiO_2 and NiO film were enhanced by a poled ferroelectric $LiNbO_3$ substrate. ZnO has been used as an integrated piezo-photocatalyst, and the photocatalytic efficiency can be further improved by combining ZnO with other piezoelectric materials or photocatalytic materials. Ordered and vertical CuS/ZnO heterostructure nanowires were grown on stainless steel mesh, enabling the recovery of CuS/ZnO from the treated solution.[56] Further, the CuS/ZnO nanocomposite obtained large deformation under strain and generated a high piezoelectric field because of the mesh support and CuS/ZnO alignment. The schematic diagrams of CuS/ZnO nanocomposite during the piezo-photocatalytic process and methylene blue (MB) degradation activities are shown in Figure 1.19(a-d). In conclusion, the CuS/ZnO nanowires supported on mech exhibited the strongest MB degradation under solar and ultrasound, much higher than that under solar only. You et al.[57] synthesized ZnO@TiO_2 core-shell nanofibers by hydrothermal treatment for methyl orange (MO) degradation. The schematic diagram, structure, and MO degradation activities of ZnO@TiO_2 nanofibers are shown in Figure 1.19(e-g). The degradation of ZnO@TiO2 under mechano-/photo- bicatalysis was superior to that under mechano- or photo- catalysis due to the piezo-photocatalytic effect.

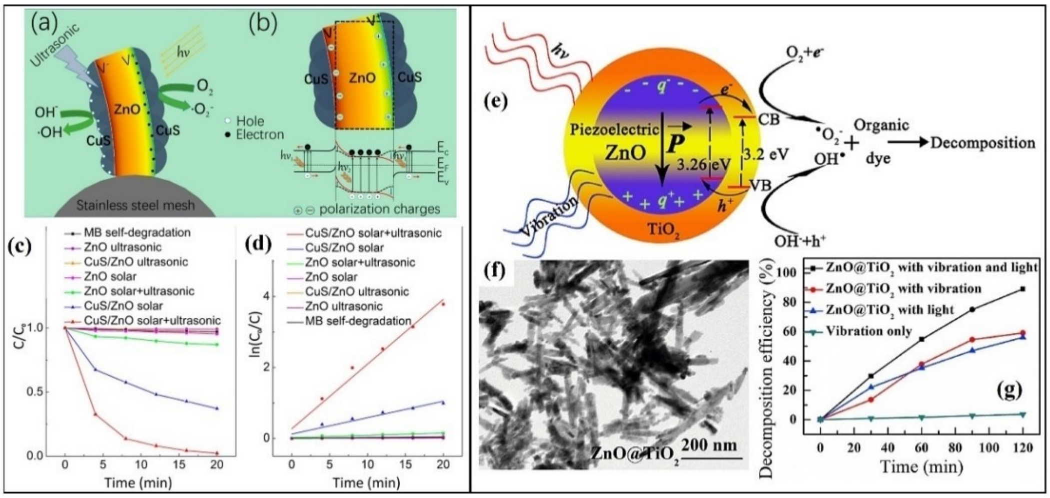

Figure 1.19 Schematic illustration of (a)the piezo-photocatalytic process and (b) the energy band of CuS/ZnO nanowires on stainless steel mesh, (c) MB degradation profiles, (d) photocatalytic degradation kinetic curves.[56] (e) Schematic diagram of the mechano-/photo- bi-catalysis and (f) TEM image of ZnO@TiO_2 core-shell nanofibers, (g) the MO decomposition efficiencies.[57]

$BaTiO_3$ is a potential piezo-ceramics due to its high piezoelectric coefficient and nontoxicity, so it is often combined with other materials for photocatalytic activity. Zhou et al.[58] proposed a piezoelectric ZnO/$BaTiO_3$ heterostructure. The piezoelectric potential difference on ZnO/$BaTiO_3$ was 414.40 mV, which was higher than that of

$BaTiO_3$ (409.50 mV) and ZnO (33.00 mV). The rhodamine B (Rh B) degradation by different catalysts (blank, ZnO, $BaTiO_3$, and ZnO/$BaTiO_3$) under different parameters (visible light, UV light, visible light, and ultrasound, as well as UV light and ultrasound) are shown in Figure 1.20(a-d). Under the excitations of ultrasound (120 W) and simulated sunlight (100 mW cm^{-2}), the oxidation reaction rate constant of ZnO/$BaTiO_3$ for Rh B degradation was up to 0.12 min^{-1}, which was 1.5 and 2 times that of $BaTiO_3$ and ZnO, respectively. Ferroelectric $BaTiO_3$ nanocrystals were combined with photocatalyst Ag_2O to form an Ag_2O-$BaTiO_3$ hybrid photocatalyst, and Rh B degradation was used to evaluate the catalytic efficiency.[59] From the photodegradation activities in Figure 1.20(g-j), the degradation rate of the Ag_2O-$BaTiO_3$ hybrid under ultrasonic and UV irradiation was stronger than that of P25, Ag_2O, and Ag_2O-$BaTiO_3$ physical mixture under the same conditions, as well as than that of Ag_2O-$BaTiO_3$ hybrid under only ultrasonic irradiation and only UV light.

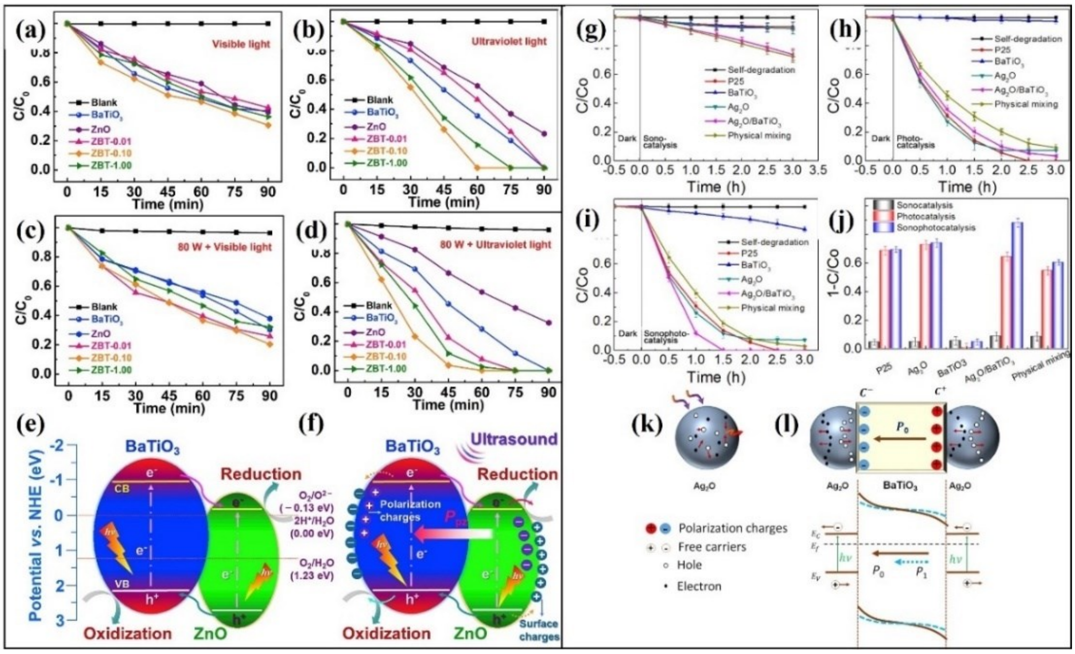

Figure 1.20 (a-d) Contaminant degradation as a function of time for $BaTiO_3$, ZnO, and ZnO/$BaTiO_3$ under different parameters (80 W: the power of ultrasonic), (e, f) schematic mechanisms in ZnO/$BaTiO_3$ mediate.[58] Degradation of Rh B as a function of irradiation time for (g) sonocatalysis, (h) photocatalysis, and (i) sonophotocatalysis in the presence of different catalysts, (j) Rh B degradations under different situations, schematic mechanisms in (k) an Ag_2O nanoparticle and (l) in Ag_2O–$BaTiO_3$ hybrid nanocubes when excited by photons.[59]

1.3.2.4 Hybrid piezo-photocatalysts based on organic piezo-polymers

Piezoelectric polymer films exhibit high sensitivity to mild, discontinuous, or low-frequency stress, making them ideal hybrid piezo-photocatalysts for piezo-photocatalysis. Furthermore, polymer films endow the piezo-photocatalysts with recoverability for sustainable applications. As a typical piezoelectric polymer, PVDF has been widely combined with nanostructured semiconductors to fabricate hybrid piezo-photocatalysts for enhanced photocatalytic efficiency.

PVDF-TiO_2 and PDMS-TiO_2 composite films were prepared by coating the mixture solution of TiO_2 and polymer on glass sheets and their photocatalytic activities were compared, which was the first time to introduce PVDF into a photocatalyst system.[60] From the Rh B degradations under different conditions in Figure 1.21(a-b), the order of photodegradation efficiencies is U-L-PVDF-TiO_2 (95%) > U-L-PDMS-TiO_2 (70%) > S-L-PDMS-TiO_2 (43%) ≈ S-L-PVDF-TiO_2 (38%). Furthermore, the photocatalytic efficiency of PVDF-TiO_2 film under ultrasound and UV light was increased by 55% and the k value became 5.42 times higher compared with those under magnetic stirring and UV light, while it is only 30% and 1.67 times for the PDMS-TiO_2 film. These results indicated that ultrasonic wave vibration boosted the photocatalysis of PVDF-TiO_2 at a higher level than that of PDMS-TiO_2 due to the piezoelectric effect on PVDF.

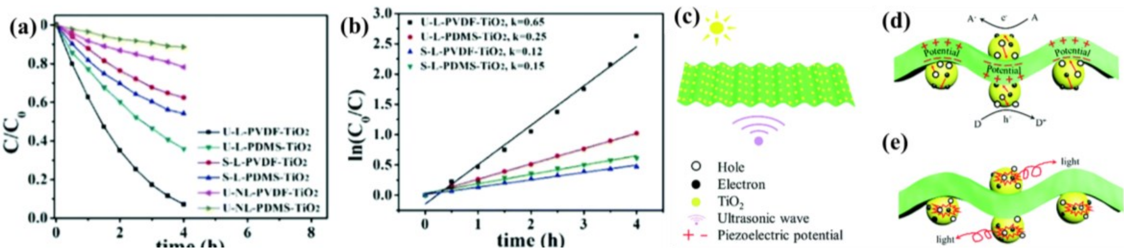

Figure 1.21 (a, b) The photocatalytic Rh B degradation curves of the PDMS-TiO_2 film and PVDF-TiO_2 film under ultrasound + UV light (U-L), magnetic stirring + UV light (S-L), and ultrasound (U-NL), the generation of charge carriers on (d) PVDF-TiO_2 film and (e) PDMS-TiO_2 film.[60]

The polymer states in hybrid piezo-photocatalysts have progressed from flat films to microfiber membranes and nanofiber membranes, with increased surface area and easily deformable polymer properties. Dong et al.[61] prepared hybrid PVDF/TiO_2 nanofibers membranes through electrospinning PVDF and tetrabutyl titanate (precursor of TiO_2) solution followed by annealing treatment. The hybrid PVDF/TiO_2 nanofibers membrane can be used as a self-powering/self-cleaning electronic-skin (e-skin) to detect body motions (as shown in Figure 1.22(b)) and degrade MB dye in solution (as shown in Figure 1.22(a)). The degradation activities of hybrid PVDF/TiO_2 membrane under ultrasonic (mechanical vibration) and UV was faster than that under only UV, and much faster than those under only ultrasonic (mechanical vibration), no ultrasonic (mechanical vibration) and UV. And the higher frequency of mechanical vibration resulted in faster degradation activity. Besides, compared to pure PVDF and pure P25, more MB can be degraded within 40 min using the e-skin under ultrasonic and UV irradiation.

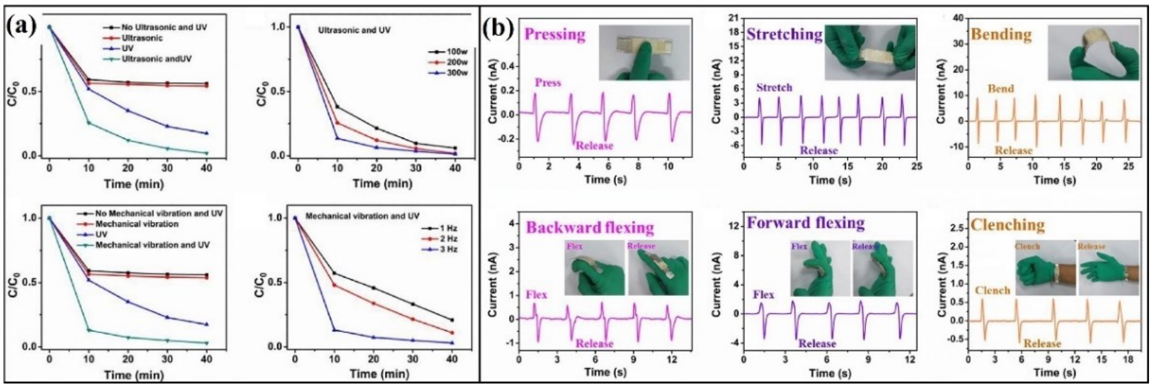

Figure 1.22 (a) MB degradation catalyzed by polarized PVDF/TiO_2 nanofibers film under different conditions, (b) piezoelectric current outputs of the e-skin under different body motions.[61]

For the preparation of most hybrid piezo-polymer photocatalysts, the photocatalysts are added to polymer solutions, and then the mixed solutions are used to prepare films or fiber membranes. Notably, due to the uniform distribution of photocatalysts throughout the whole volume, only a part of photocatalysts are placed on the surface of films or fibers, which blocks most of the photocatalysts and reduces the reactive sites on photocatalysts. Therefore, advanced preparation methods should be employed to solve this problem.

Sn_3O_4/PVDF hybrid film was synthesized by hydrothermal treatment on PVDF film in the Sn^{2+} precursor solution.[62] The schematic diagram of the growth mechanism of Sn_3O_4/PVDF hybrid film was given in Figure 1.23(a). Due to the high electronegativity of F atoms, XPS and Raman results confirmed that the coordinated bond between F ion and metal ion was a key condition for the synthesis of Sn_3O_4 on the PVDF film surface, which made Sn_3O_4/PVDF hybrid film hydrophilic and Sn_3O_4 directly participate in the photocatalytic system. The photocatalytic activities of Sn_3O_4/PVDF hybrid film and other catalysts were performed via Rh B degradation under different water flow speeds and different distances between the photocatalyst and the vibration source, as shown in Figure 1.23(b and c). The results illustrated that the higher flow speed or shorter distance resulted in the higher degradation rate due to the built-in electric field of the PVDF film.

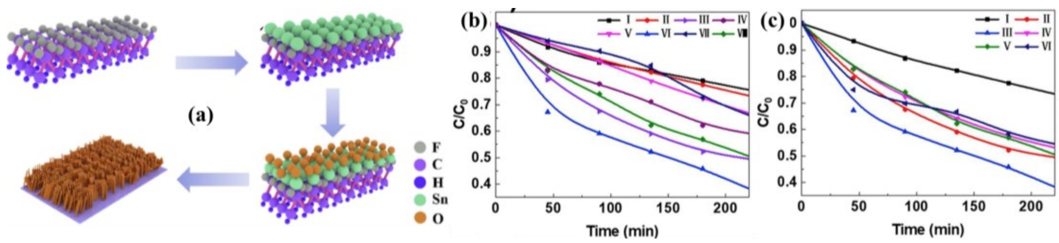

Figure 1.23 (a) Schematic illustration of the growth mechanism of Sn_3O_4/PVDF hybrid film; (b, c) the photocatalytic degradation of Rh B under UV light (b) (I) no photocatalyst, 22 mL/min (water flow rate), (II) no photocatalyst, 480 mL/min, (III) Sn_3O_4, 480 mL/min, (IV) Sn_3O_4, 22 mL/min, (V) Sn_3O_4/PVDF, 22 mL/min, (VI) Sn_3O_4/PVDF, 480 mL/min, (VII) Sn_3O_4/PTF, 22 mL/min, (VIII) Sn_3O_4/PTFE, 480 mL/min; (c) (I) no photocatalyst; (II) Sn_3O_4; (III) Sn_3O_4/PVDF, 2 cm (the distance between photocatalyst to the vibration source), (IV) Sn_3O_4/PVDF, 12 cm, (V) Sn_3O_4/PTFE, 2 cm, (VI) Sn_3O_4/PTFE, 12 cm.[62]

Durairaj et al.[63] prepared PVDF-TiO_2 hybrid nanofiber membrane by sequential electrospinning PVDF solution and electrospraying TiO_2 suspension. TiO_2 NPs were distributed on the surface of PVDF NFs from the SEM image (in Figure 1.24(a, b)), and 53% of the PVDF NFs were covered by TiO_2 NPs from the XPS result. The photocatalytic activities of PVDF-TiO_2 hybrid nanofiber membrane for MB degradation were shown in Figure 1.24(c-e). Under UV irradiation, the air bubble enhanced the MB degradation over the PVDF-TiO_2 hybrid membrane by 99% because of the induced piezoelectric field on PVDF, while pure TiO_2 had no enhancement. In addition, the MB degradation in the presence of PVDF-TiO_2 hybrid membrane was related to the extent of the air bubble supply. These results demonstrated the piezoelectric effect had an obvious effect on the photocatalytic activity. However, the MB degradation efficiency decreased with increasing cycle time due to the loss of TiO_2 during the processes, as shown in Figure 1.24(f), which meant the stability of the hybrid membrane needed to be improved.

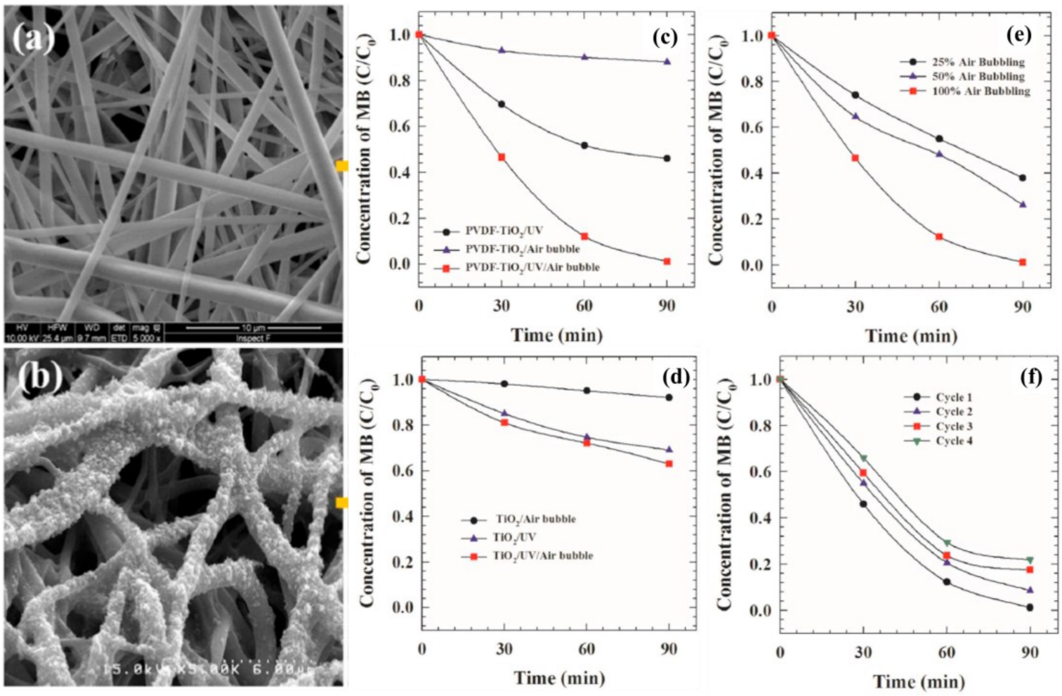

Figure 1.24 SEM image of (a) PVDF layer (b) PVDF-TiO_2 hybrid; piezo-photocatalytic degradation of MB (c) by PVDF-TiO_2 hybrid under UV or/and air bubble, (d) by P25 NPs under UV or/and air bubble, (e) by PVDF-TiO_2 hybrid under air bubble with different extends, and (f) by PVDF-TiO_2 hybrid for four cycles.[63]

Few works have reported the preparation of piezo-photocatalysts based on polymer support and exposure of catalysts out of polymer. Therefore, there is still much room for improvement in the preparation of hybrid piezo-polymer photocatalysts to promote piezo-photocatalysis.

1.4 Aims of research

PVDF is the most widely investigated piezoelectric polymer because of its excellent properties and low price. Meanwhile, TiO_2 has been extensively studied as a photocatalyst due to its chemical stability, environmental friendliness, photostability, and low cost. Therefore, we aim to prepare a hybrid PVDF/TiO_2 piezo-photocatalyst with high performance, focusing on three aspects: 1). Achieving a good combination of PVDF and TiO_2; 2). Exposing TiO_2 and maintaining a large effective surface area; 3). Recovering the used photocatalyst for reuse and avoiding a secondary pollutant. Furthermore, the effect of PVDF polarization on the photocatalytic activity of TiO_2 was studied to improve the catalytic activity.

PVDF as support enables the PVDF/TiO_2 hybrid piezo-photocatalyst easy to operate and recycle. To achieve a PVDF/TiO_2 hybrid piezo-photocatalyst with high surface area and TiO_2 exposure, a nanofiber membrane is proposed in which TiO_2 nanoparticles are covered on the surface of PVDF nanofibers. Therefore, a PVDF-TiO_2 core-shell nanofiber membrane meets the mentioned requests and is the pursuit of the current work.

Electrospinning method provides operational flexibility for the preparations of different nanocomposites in the form of nanofibers, nanoparticles, nanoribbons, and more. Numerous metallic and inorganic particles have been incorporated into polymer nanofibers membrane to achieve desired composites that possess advantages of polymer nanofibers (such as flexibility, lightweight, and high surface-area-to-volume ratio) and the characteristics of particles in specific fields (like electrical, optical, catalytical). In recent years, the immobilization of particles in electrospun nanofibers membrane has received extensive attention, and methods to obtain core-shell nanofiber structure are summarized below:

1) Preparations of semiconductor/polymer composites by electrospinning technique, such as electrospinning polymer solution and electrospraying semiconductor solution or suspension.

2) Preparations of semiconductor/polymer composites by combining electrospinning with post-treatments, such as deposition technologies (CVD, PVD, etc.), thermal treatments, and redox treatments.

Each method have its own features in terms of the preparation and the obtained composites. Appropriate preparations should be found to prepare PVDF-TiO_2 core-shell nanofiber membranes that satisfy the requirements.

In conclusion, this dissertation focuses on the preparations of PVDF-TiO_2 core-shell nanofiber membranes and the investigation of piezo-potential effects on photocatalytic performance.

References

(1) Gerischer, H. Semiconductor electrochemistry. **1968**.

(2) Fujishima, A.; Honda, K. Electrochemical Photolysis of Water at a Semiconductor Electrode. *Nature* **1972**, *238*, 37-38.

(3) O'regan, B.; Grätzel, M. A low-cost, high-efficiency solar cell based on dye-sensitized colloidal TiO2 films. *nature* **1991**, *353*, 737-740.

(4) Zhou, H.; Qu, Y.; Zeid, T.; Duan, X. Towards highly efficient photocatalysts using semiconductor nanoarchitectures. *Energy & Environmental Science* **2012**, *5*, 6732-6743.

(5) Serpone, N.; Emeline, A. V. Semiconductor Photocatalysis — Past, Present, and Future Outlook. *The Journal of Physical Chemistry Letters* **2012**, *3*, 673-677.

(6) Schneider, J.; Bahnemann, D.; Ye, J.; Puma, G. L.; Dionysiou, D. D.: *Photocatalysis: fundamentals and perspectives*; Royal Society of Chemistry, 2016.

(7) Ameta, R.; Ameta, S. C.: *Photocatalysis: principles and applications*; Crc Press, 2016.

(8) Kočí, K.; Obalová, L.; Matějová, L.; Plachá, D.; Lacný, Z.; Jirkovský, J.; Šolcová, O. Effect of TiO_2 particle size on the photocatalytic reduction of CO_2. *Applied Catalysis B: Environmental* **2009**, *89*, 494-502.

(9) Xu, H.; Ouyang, S.; Li, P.; Kako, T.; Ye, J. High-active anatase TiO_2 nanosheets exposed with 95%{100} facets toward efficient H_2 evolution and CO_2 photoreduction. *Acs Appl Mater Inter* **2013**, *5*, 1348-1354.

(10) Macak, J. M.; Zlamal, M.; Krysa, J.; Schmuki, P. Self-organized TiO_2 nanotube layers as highly efficient photocatalysts. *small* **2007**, *3*, 300-304.

(11) Yang, Y.; Qiu, M.; Liu, L. TiO_2 nanorod array@ carbon cloth photocatalyst for CO_2 reduction. *Ceramics International* **2016**, *42*, 15081-15086.

(12) Tahir, M.; Tahir, B.; Amin, N. A. S. Gold-nanoparticle-modified TiO_2 nanowires for plasmon-enhanced photocatalytic CO_2 reduction with H_2 under visible light irradiation. *Applied Surface Science* **2015**, *356*, 1289-1299.

(13) Lüssem, B.; Riede, M.; Leo, K. Doping of organic semiconductors. *physica status solidi (a)* **2013**, *210*, 9-43.

(14) Maeda, M.; Yamada, T. In *Tilte*2007; IOP Publishing.

(15) Sun, W.-T.; Yu, Y.; Pan, H.-Y.; Gao, X.-F.; Chen, Q.; Peng, L.-M. CdS quantum dots sensitized TiO_2 nanotube-array photoelectrodes. *J Am Chem Soc* **2008**, *130*, 1124-1125.

(16) Baker, D. R.; Kamat, P. V. Photosensitization of TiO_2 nanostructures with CdS quantum dots: particulate versus tubular support architectures. *Advanced Functional Materials* **2009**, *19*, 805-811.

(17) Nguyen, T.-V.; Wu, J. C.; Chiou, C.-H. Photoreduction of CO_2 over Ruthenium dye-sensitized TiO_2-based catalysts under concentrated natural sunlight. *Catalysis Communications* **2008**, *9*, 2073-2076.

(18) Mudhoo, A.; Paliya, S.; Goswami, P.; Singh, M.; Lofrano, G.; Carotenuto, M.; Carraturo, F.; Libralato, G.; Guida, M.; Usman, M. Fabrication, functionalization and performance of doped photocatalysts for dye degradation and mineralization: a review. *Environmental Chemistry Letters* **2020**, *18*, 1825-1903.

(19) Ismail, A. A.; Bahnemann, D. W. Photochemical splitting of water for hydrogen production by photocatalysis: A review. *Solar Energy Materials and Solar Cells* **2014**, *128*, 85-101.

(20) Khan, A. A.; Tahir, M. Recent advancements in engineering approach towards design of photo-reactors for selective photocatalytic CO_2 reduction to renewable fuels. *Journal of CO_2 Utilization* **2019**, *29*, 205-239.

(21) Shehzad, N.; Tahir, M.; Johari, K.; Murugesan, T.; Hussain, M. A critical review on TiO_2 based photocatalytic CO_2 reduction system: Strategies to improve efficiency. *Journal of CO_2 Utilization* **2018**, *26*, 98-122.

(22) Katzir, S.: The discovery of the piezoelectric effect. In *The beginnings of piezoelectricity*; Springer, 2006; pp 15-64.

(23) Atif, R.; Khaliq, J.; Combrinck, M.; Hassanin, A. H.; Shehata, N.; Elnabawy, E.; Shyha, I. Solution blow spinning of polyvinylidene fluoride based fibers for energy harvesting applications: A review. *Polymers* **2020**, *12*, 1304.

(24) Ok, K. M.; Chi, E. O.; Halasyamani, P. S. Bulk characterization methods for non-centrosymmetric materials: second-harmonic generation, piezoelectricity, pyroelectricity, and ferroelectricity. *Chemical Society Reviews* **2006**, *35*, 710-717.

(25) Ohsato, H. Origin of piezoelectricity on langasite. *Materials Science and Technology, edited by: Hutagalung, S., IntechOpen, Rijeka, Croatia* **2012**, 15-40.

(26) Mishra, S.; Unnikrishnan, L.; Nayak, S. K.; Mohanty, S. Advances in piezoelectric polymer composites for energy harvesting applications: a systematic review. *Macromolecular Materials and Engineering* **2019**, *304*, 1800463.

(27) Uchino, K.: *Advanced piezoelectric materials: Science and technology*; Woodhead Publishing, 2017.

(28) Park, S.-E. E.; Hackenberger, W. High performance single crystal piezoelectrics: applications and issues. *Current Opinion in Solid State and Materials Science* **2002**, *6*, 11-18.

(29) Li, F.; Shen, T.; Wang, C.; Zhang, Y.; Qi, J.; Zhang, H. Recent Advances in Strain-Induced Piezoelectric and Piezoresistive Effect-Engineered 2D Semiconductors for Adaptive Electronics and Optoelectronics. *Nano-Micro Letters* **2020**, *12*, 106.

(30) Alguero, M.; Cheng, B.; Guiu, F.; Reece, M.; Poole, M.; Alford, N. Degradation of the d33 piezoelectric coefficient for PZT ceramics under static and

cyclic compressive loading. *Journal of the European ceramic society* **2001**, *21*, 1437-1440.

(31) Jaffe, H. Piezoelectric ceramics. *Journal of the American Ceramic Society* **1958**, *41*, 494-498.

(32) Sperati, C. A.; Starkweather, H. W.: Fluorine-containing polymers. II. Polytetrafluoroethylene. In *Fortschritte Der Hochpolymeren-Forschung*; Springer, 1961; pp 465-495.

(33) Chauhan, S. S.; Bhatt, U. M.; Gautam, P.; Thote, S.; Joglekar, M. M.; Manhas, S. K. Fabrication and modeling of β-phase PVDF-TrFE based flexible piezoelectric energy harvester. *Sensors and Actuators A: Physical* **2020**, *304*, 111879.

(34) Park, S.; Kim, Y.; Jung, H.; Park, J.-Y.; Lee, N.; Seo, Y. Energy harvesting efficiency of piezoelectric polymer film with graphene and metal electrodes. *Scientific reports* **2017**, *7*, 1-8.

(35) Khanbareh, H.; Topolov, V. Y.; Bowen, C. R.: *Piezo-particulate Composites: Manufacturing, Properties, Applications*; Springer, 2019; Vol. 283.

(36) Saito, Y.; Takao, H.; Tani, T.; Nonoyama, T.; Takatori, K.; Homma, T.; Nagaya, T.; Nakamura, M. Lead-free piezoceramics. *Nature* **2004**, *432*, 84-87.

(37) Tressler, J. F.: Piezoelectric transducer designs for sonar applications. In *Piezoelectric and acoustic materials for transducer applications*; Springer, 2008; pp 217-239.

(38) Kim, H.; Priya, S.; Uchino, K. Modeling of piezoelectric energy harvesting using cymbal transducers. *Japanese journal of applied physics* **2006**, *45*, 5836.

(39) Uchino, K.; Ishii, T. Energy flow analysis in piezoelectric energy harvesting systems. *Ferroelectrics* **2010**, *400*, 305-320.

(40) Gupta, M.; Agrawal, S.; Sathiskumar, A.; Sangheetha, A. Blending modern multifunctional materials with traditional structures: An approach for a greener and cleaner future.

(41) Li, L.; Salvador, P. A.; Rohrer, G. S. Photocatalysts with internal electric fields. *Nanoscale* **2014**, *6*, 24-42.

(42) Li, J.; Cai, L.; Shang, J.; Yu, Y.; Zhang, L. Giant enhancement of internal electric field boosting bulk charge separation for photocatalysis. *Advanced Materials* **2016**, *28*, 4059-4064.

(43) Lou, Z.; Wang, P.; Huang, B.; Dai, Y.; Qin, X.; Zhang, X.; Wang, Z.; Liu, Y. Enhancing charge separation in photocatalysts with internal polar electric fields. *ChemPhotoChem* **2017**, *1*, 136-147.

(44) Zhu, Q.; Zhang, K.; Li, D.; Li, N.; Xu, J.; Bahnemann, D. W.; Wang, C. Polarization-enhanced photocatalytic activity in non-centrosymmetric materials based photocatalysis: A review. *Chemical Engineering Journal* **2021**, *426*, 131681.

(45) Giocondi, J. L.; Rohrer, G. S. Spatial separation of photochemical oxidation and reduction reactions on the surface of ferroelectric BaTiO3. *The Journal of Physical Chemistry B* **2001**, *105*, 8275-8277.

(46) Burbure, N. V.; Salvador, P. A.; Rohrer, G. S. Photochemical reactivity of titania films on BaTiO3 substrates: origin of spatial selectivity. *Chemistry of Materials* **2010**, *22*, 5823-5830.

(47) Tu, S.; Guo, Y.; Zhang, Y.; Hu, C.; Zhang, T.; Ma, T.; Huang, H. Piezocatalysis and piezo - photocatalysis: catalysts classification and modification strategy, reaction mechanism, and practical application. *Advanced Functional Materials* **2020**, *30*, 2005158.

(48) Starr, M. B.; Wang, X. Fundamental analysis of piezocatalysis process on the surfaces of strained piezoelectric materials. *Scientific Reports* **2013**, *3*, 1-8.

(49) Singh, S.; Khare, N. Coupling of piezoelectric, semiconducting and photoexcitation properties in $NaNbO_3$ nanostructures for controlling electrical transport: realizing an efficient piezo-photoanode and piezo-photocatalyst. *Nano Energy* **2017**, *38*, 335-341.

(50) Thakur, D.; Sharma, M.; Vaish, R.; Balakrishnan, V. WS_2 monolayer for piezo–phototronic dye degradation and bacterial disinfection. *ACS Applied Nano Materials* **2021**, *4*, 7879-7887.

(51) Xue, X.; Zang, W.; Deng, P.; Wang, Q.; Xing, L.; Zhang, Y.; Wang, Z. L. Piezo-potential enhanced photocatalytic degradation of organic dye using ZnO nanowires. *Nano Energy* **2015**, *13*, 414-422.

(52) Burbure, N. V.; Salvador, P. A.; Rohrer, G. S. Influence of dipolar fields on the photochemical reactivity of thin titania films on $BaTiO_3$ substrates. *Journal of the American Ceramic Society* **2006**, *89*, 2943-2945.

(53) Zhang, Y.; Schultz, A. M.; Salvador, P. A.; Rohrer, G. S. Spatially selective visible light photocatalytic activity of $TiO_2/BiFeO_3$ heterostructures. *J Mater Chem* **2011**, *21*, 4168-4174.

(54) Inoue, Y.; Okamura, M.; Sato, K. A thin-film semiconducting titanium dioxide combined with ferroelectrics for photoassisted water decomposition. *The Journal of Physical Chemistry* **1985**, *89*, 5184-5187.

(55) Inoue, Y.; Sato, K.; Sato, K.; Miyama, H. A device type photocatalyst using oppositely polarized ferroelectric substrates. *Chemical physics letters* **1986**, *129*, 79-81.

(56) Hong, D.; Zang, W.; Guo, X.; Fu, Y.; He, H.; Sun, J.; Xing, L.; Liu, B.; Xue, X. High piezo-photocatalytic efficiency of CuS/ZnO nanowires using both solar and mechanical energy for degrading organic dye. *Acs Appl Mater Inter* **2016**, *8*, 21302-21314.

(57) You, H.; Wu, Z.; Jia, Y.; Xu, X.; Xia, Y.; Han, Z.; Wang, Y. High-efficiency and mechano-/photo-bi-catalysis of piezoelectric-ZnO@ photoelectric-TiO_2 core-shell nanofibers for dye decomposition. *Chemosphere* **2017**, *183*, 528-535.

(58) Zhou, X.; Wu, S.; Li, C.; Yan, F.; Bai, H.; Shen, B.; Zeng, H.; Zhai, J. Piezophototronic effect in enhancing charge carrier separation and transfer in $ZnO/BaTiO_3$ heterostructures for high-efficiency catalytic oxidation. *Nano Energy* **2019**, *66*, 104127.

(59) Li, H.; Sang, Y.; Chang, S.; Huang, X.; Zhang, Y.; Yang, R.; Jiang, H.; Liu, H.; Wang, Z. L. Enhanced ferroelectric-nanocrystal-based hybrid photocatalysis by ultrasonic-wave-generated piezophototronic effect. *Nano letters* **2015**, *15*, 2372-2379.

(60) Dai, B.; Huang, H.; Wang, W.; Chen, Y.; Lu, C.; Kou, J.; Wang, L.; Wang, F.; Xu, Z. Greatly enhanced photocatalytic activity by organic flexible piezoelectric PVDF induced spatial electric field. *Catalysis Science & Technology* **2017**, *7*, 5594-5601.

(61) Dong, C.; Fu, Y.; Zang, W.; He, H.; Xing, L.; Xue, X. Self-powering/self-cleaning electronic-skin basing on PVDF/TiO_2 nanofibers for actively detecting body motion and degrading organic pollutants. *Applied Surface Science* **2017**, *416*, 424-431.

(62) Han, S.; Chen, D.; Wang, J.; Liu, Z.; Liu, F.; Chen, Y.; Ji, Y.; Pang, J.; Liu, H.; Wang, J. Assembling Sn_3O_4 nanostructures on a hydrophobic PVDF film through metal-F coordination to construct a piezotronic effect-enhanced Sn_3O_4/PVDF hybrid photocatalyst. *Nano Energy* **2020**, *72*, 104688.

(63) Durairaj, A.; Ramasundaram, S.; Sakthivel, T.; Ramanathan, S.; Rahaman, A.; Kim, B.; Vasanthkumar, S. Air bubbles induced piezophotocatalytic degradation of organic pollutants using nanofibrous poly (vinylidene fluoride)-titanium dioxide hybrid. *Applied Surface Science* **2019**, *493*, 1268-1277.

Chapter II Techniques and characterizations

2.1 Techniques

2.1.1 Electrospinning

Electrospinning is a specific electrohydrodynamic process that can produce fibers with diameters ranging from micrometers to nanometers by means of electrostatic fields applied to polymer solutions or melts. Electrospinning looks like a combination of electrospraying and conventional dry or melt spinning.

The basic setup for electrospinning consists of a syringe tipped with a metal needle, a syringe pump, a collector, and a high-voltage power source (positive and negative voltage ends are connected respectively to the needle and the collector). With the development of the electrospinning technique, several types of needles (such as single, coaxial, and multi-axial ones) and collectors (like flat plate, drum, and disk), as well as needle-less electrospinning, have emerged to meet different requirements from arrangements (e.g., aligned fibers, random orientations, or their combinations) and morphological structures (e.g., single/hollow/core-shell structures, or smooth/porous/wrinkled surfaces) to production yield. A schematic diagram of electrospinning setup with variants is shown in Figure 2.1.

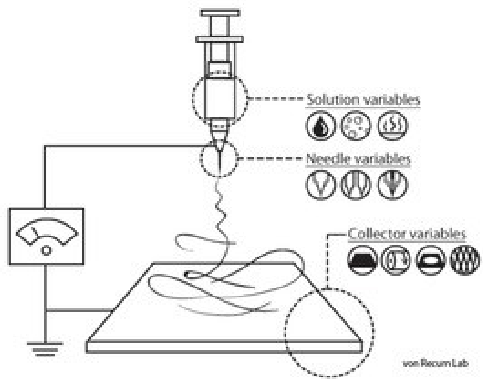

Figure 2.1 Schematic diagram of electrospinning setup with variations.

A polymer solution or melt is loaded into a syringe and the solution is extruded from the needle tip at a constant rate by the pump. Charges accumulate on the surface of the liquid (on the needle tip) under the electric field. Once the electrostatic repulsion on the liquid is greater than its surface tension, the liquid meniscus deforms into a conical structure known as a Taylor cone and a jet from the Taylor cone ejects towards the collector. The jet accelerates with the solvent evaporating during the flight process, then a fiber mat is gathered on the collector. When a particle suspension instead of a polymer solution is applied here, this process is called electrospray.

Various parameters can influence a final product (success or failure, good or bad) on the collector, and they can be divided into three categories:

- Solution parameters: polymer concentration, molecular weight, conductivity, viscosity, surface tension, etc.
- Processing parameters: voltage, tip-to-collector distance, and feed rate.
- Ambient parameters: humidity, and temperature.

Actually, some parameters are intrinsically linked, so it is not easy to discuss the impact on the final product from a single parameter.

2.1.2 Hydrothermal treatment

Hydrothermal treatment refers to a thermochemical process in an aqueous solution under high temperature and high pressure. Hydrothermal treatment can refer to hydrothermal synthesis, hydrothermal crystallization, hydrothermal annealing, etc. Hydrothermal treatments are conducted in a special sealed container, usually a Teflon-lined autoclave. Teflon is inert to both hydrofluoric acid and alkaline media, and the autoclave is strong enough to withstand high pressure. It is worth noticing that substances with specific valence, configuration, and crystal morphology can be formed via hydrothermal treatments with medium temperature and pressure. In addition, hydrothermal synthesis can obtain substances that are impossible to be prepared by other synthesis methods because reactants will retain rather than evaporate at high temperatures.

Outstanding characteristics of water under subcritical/supercritical condition are the key to the advantages of hydrothermal synthesis: 1). Water dissociates into hydronium ions (H_3O^+) and hydroxyl ions (OH^-) under subcritical/supercritical condition, and the produced ions make water behave like a molten salt; 2). The dielectric constant (ε) of water is reduced from 80 to 20, making undissolved compounds soluble; 3). Molecules and ions move more easily in water than normal because elevated temperature reduces the viscosity of water. Additionally, other parameters of water can be changed by varying the temperature and/or pressure. In conclusion, hydrothermal synthesis has three features: accelerating the reaction rate among the complex ions; intensifying the hydrolyzation reaction; significantly changing the redox potential of the reactants.

When water is replaced by other solvents, this process is called solvothermal synthesis, which has a similar mechanism and function as hydrothermal synthesis.

2.1.3 Atomic layer deposition (ALD)

Atomic layer deposition (ALD) is a low-temperature chemical vapor deposition technique in which the growth of materials is controlled by sequential self-saturating gas-solid surface reactions. ALD has the capability to grow thickness-controlled (even at the atomic level), uniform, and conformal layer on the surface of 3D structures with complex shapes and high-aspect-ratios.

In the ALD process, a substrate is exposed to two precursors A and B in a sequential, non-overlapping way. A cycle of ALD consists of four steps, which can be repeated until achieving the desired deposit thickness. Four steps constitute one ALD cycle, as described below, and a corresponding schematic diagram is shown in Figure 2.2.

Step 1) Precursor A in gas phase is poured into the deposition chamber and reacts with a finite number of reactive sites on the substance in a dose time under proper parameters. Because of the high pressure in the chamber, molecule A can reach anywhere of substance.

Step 2) The remaining A molecules and floating reaction products are flushed away by an inert gas.

Step 3) Precursor B is poured into the chamber to react with a finite number of reactive sites on molecule A.

Step 4) Inert gas purges the remaining B molecules and floating reaction products in the chamber.

The dose-purge-dose-purge sequence constitutes one ALD cycle, and the grown thickness of one cycle is defined as the growth per cycle (GPC) value. Therefore, the desired deposition thickness depends on the GPC value and cycle number.

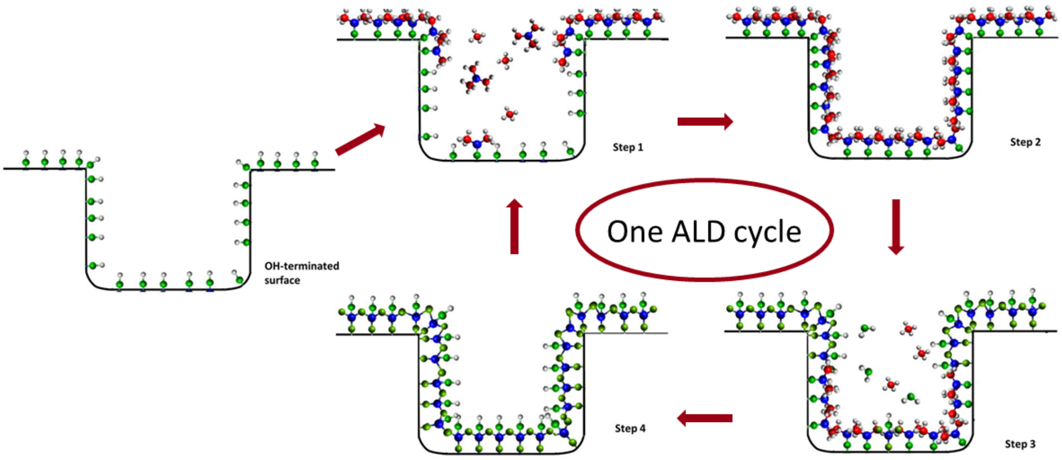

Figure 2.2 Schematic representation of ALD process.

2.2 Characterizations

2.2.1 Scanning electron microscope (SEM)

A scanning electron microscope (SEM) is an electron microscope in which a focused electron beam interacts with atoms in a sample, collecting reflected signals to obtain information about the surface topography and composition of the sample.

Various signals are generated from the interacted atoms, as shown in Figure 2.3: secondary electrons (SE), reflected/back-scattered electrons (BSE), characteristic X-rays, cathodoluminescence (CL), etc. SE can only escape from the top few nanometers of the sample surface and be highly localized at the impact point of the primary electron beam. BSE are reflected from the sample by elastic scattering, and they originate from deeper positions than SE. The contrast in SEM images of SE signal is mainly from specimen topography, while one of BSE signal mainly corresponds to different element components.

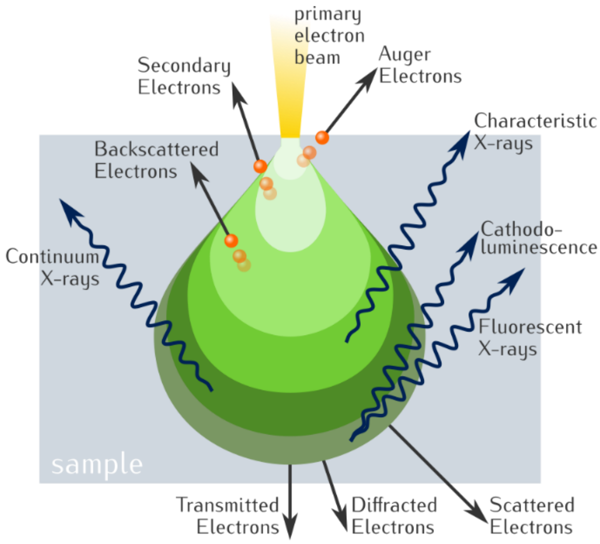

Figure 2.3 Electron–matter interaction volume and types of signals generated.

2.2.2 Transmission electron microscopy (TEM)

Transmission electron microscopy (TEM) is a microscopy technique in which a beam of electrons interacts with a sample as the beam is transmitted through the specimen (the thickness should be less than 100 nm). TEM can image at a much higher resolution than light microscopes because of the smaller de Broglie wavelength of electrons than photons.

The TEM essentially is composed of several components: an electron emission source (usually a tungsten filament heated to a very high temperature), a series of electromagnetic lenses that focus the beams on the sample at an atomic scale, a detection system that converts the information of collected electrons into images, and a high vacuum system that allows electrons to travel from the source to the sample. A comparison of optical components between TEM and SEM is shown in Figure 2.4.

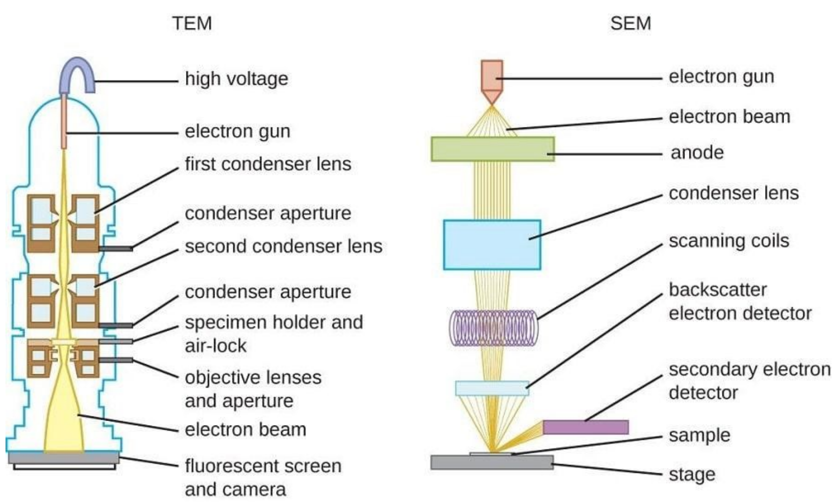

Figure 2.4 A comparison of optical components between TEM and SEM.

2.2.3 FTIR spectroscopy

Infrared (IR) spectrometer is a technique used to obtain the absorption or emission of monochromatic light in the infrared region by solids, liquids, or gases. Fourier Transform Infrared (FITR) spectrometer is an advanced version of IR spectrometer, which is achieved by an interferometer by simultaneously obtaining the absorption or emission of a sample under different frequencies of light. In the interferometer in Figure 2.5, 50% of the light is transmitted toward a moving mirror and 50% is refracted toward a fixed mirror. Then the two reflected beams with optical path differences pass through the beam splitter and become a new beam that can cover the whole infrared frequency range. Fourier transform is a data-processing technique that converts light output as a function of mirror position to light output as a function of infrared wavelength/wavenumber.

IR spectroscopy is used to identify chemical species or functional groups in substrates. For molecules with a dipole moment, the sample can have different vibrational modes under infrared radiation, such as stretching, and bending. Absorption occurs when the frequency of the IR beam is the same as the vibrational frequency of a bond or collection of bonds. IR spectroscopy reveals how much energy is absorbed in each frequency, which can then be used to identify the structure of the molecule.

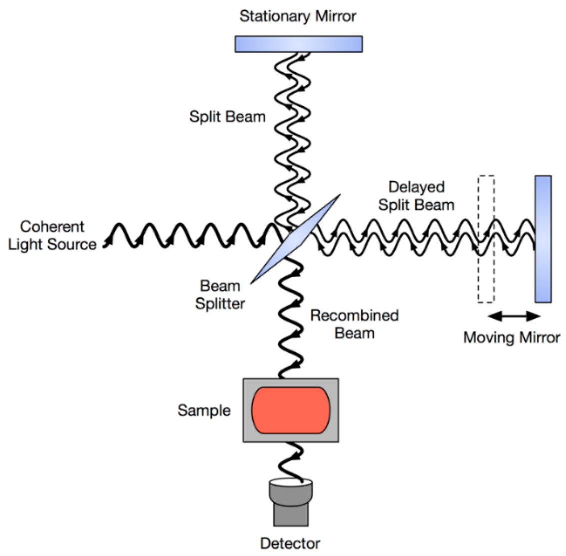

Figure 2.5 Schematic diagram of an interferometer in an FTIR spectrometer.

2.2.4 Raman spectroscopy

Raman spectroscopy is another technique that can be used to determine vibrational modes and provide a fingerprint for the detection of sample structure, which produces similar but complementary information to IR spectroscopy. Monochromatic light (usually a single-wavelength laser) in the range from near-infrared to near-ultraviolet interacts with the specimen, and when the electric dipole-electric dipole polarizability on molecule changes and the energy of photons shifts, the Raman effect will be generated. The shift in energy provides information about the vibrational modes, and the magnitude of the Raman effect is related to the polarizability change on the molecule.

A brief working mechanism of a Raman spectrometer is shown in Figure 2.6. Electromagnetic radiation generated by a laser beam irradiating a sample is collected by a lens and detected by a monochromator. Elastic or Rayleigh scattering (the direction of light is changed while the energy is the same as the incident light) at the wavelength corresponding to the laser is filtered out and only inelastic or Raman scattering (the energy and direction of light are changed) is detected.

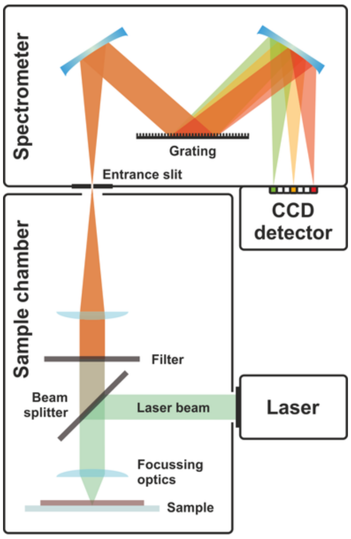

Figure 2.6 Schematic diagram of an FTIR spectrometer.

2.2.5 X-ray diffraction (XRD)

X-ray diffraction (XRD), the most widely used X-ray diffraction technique in material characterization, is used to identify the crystal structure of materials and provide other information on the physical state of the sample (such as crystallite size, and residual stress).

In an XRD diffractometer, a single wavelength X-ray beam is used to irradiate a sample. By continuously changing the incident angle of the X-ray beam, the relationship of the diffraction intensity to the angle between the incident and diffracted beams is recorded. The high-voltage field collides with the metal target to generate continuous-wavelength X-rays, and single-wavelength is achieved through an optical filter. The incident angle (θ) and the spacing between the parallel crystal planes (d) of the material determine the situations of diffraction. Particularly, when the path difference (SQ+QT=2d sinθ) of diffracted X-ray beams is equal to one or multiple X-ray wavelengths (nλ), as shown in Figure 2.7, the diffraction beam with the strongest energy can be obtained according to Bragg's law.

$$n\lambda = 2dsin\theta$$

Possible phases can be obtained by comparing the obtained spectra with a database, the International Centre for Diffraction Data (ICDD), which contains 60,000 diffraction spectra of known crystalline substances from the incident angle and the diffraction intensity.

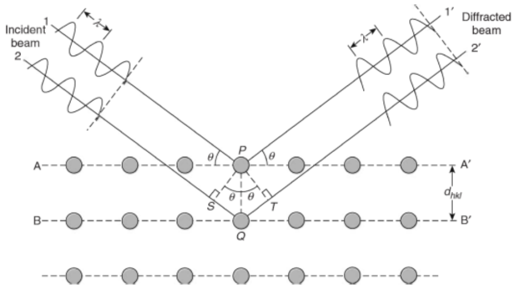

Figure 2.7 Bragg diffraction by crystal planes.

2.2.6 Differential Scanning Calorimetry (DSC)

Differential Scanning Calorimetry (DSC) is a thermal analysis technique that measures the difference in the amount of heat required to change the temperature of a sample and a reference as a function of working temperature. Heat flux DSC is a main and common type of DSC that the changes in heat flow are calculated by integrating the ΔT_{ref}- curve. A schematic diagram of the heat flux DSC is shown in Figure 2.8(a): the sample and the reference crucible are placed on a sample holder with thermocouples, and they are covered in a temperature-controlled furnace, consisting of a heat sink and heater. The temperature difference between sample and reference (DSC signal) and the absolute temperature of the sample is recorded as working temperature, and the absolute temperature of the reference and the sample is recorded as temperature difference.

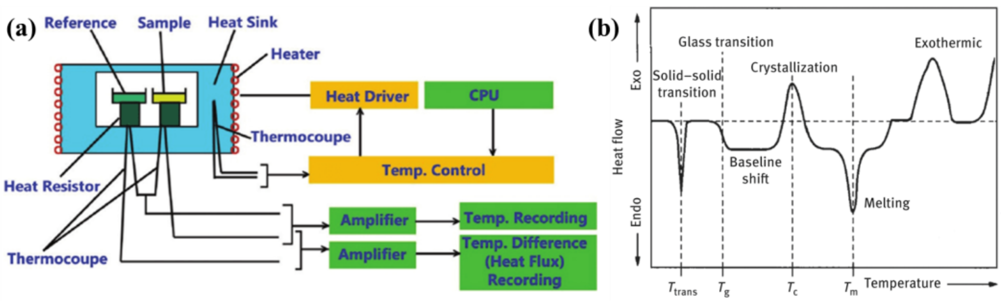

Figure 2.8 (a)Schematic diagram of differential scanning calorimeter and (b)typical transitions in a DSC thermogram.

The result of a DSC experiment is a plot of heat flux versus temperature or time, which may have steps, as well as exothermic and endothermic peaks, as shown in Figure 2.8(b). Enthalpies of transitions can be calculated by integrating the corresponding peak in the DSC curve. Therefore, fusion and crystallization events, glass transition, as well as chemical reactions are possible to be studied by DSC.

2.2.7 Thermogravimetric analysis (TGA)

Thermogravimetric analysis (TGA) is a method of thermal analysis in which the mass of a sample is a function of temperature or time as the temperature raises in a controlled atmosphere. In general, mass, temperature, and time are the basic measuring elements and other additional elements can be derived from these three measurements. Depending on the analytical procedure and the atmosphere, TGA provides information on physical phenomena (such as phase transitions, absorption, and thermal stability) and chemical phenomena (like chemisorption, oxidation, and dehydration) of the sample.

A sample pan loaded on a precision balance in a furnace with programmable temperature control under variant atmospheres is the main part of a thermogravimetric analyzer, as shown in Figure 2.9.

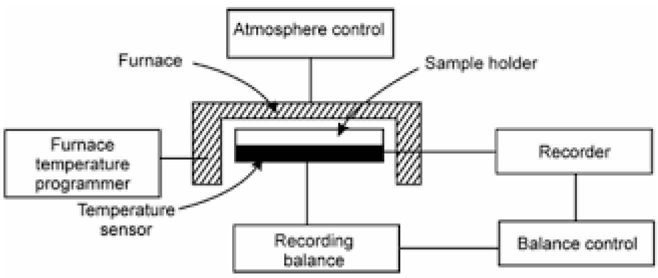

Figure 2.9 Schematic diagram of thermogravimetric analyzer.

2.2.8 UV/Vis absorption spectroscopy

Ultraviolet/Visible (UV/Vis) absorption spectroscopy is used as a qualitative tool to identify molecular species or/and as a quantitative tool to measure the quantities of species in different states (mainly solutions). Molecules and ions capable of absorbing photon energy in the UV or Vis range are called chromophores. The absorbed photons in the chromophore excite electrons from the ground state to higher energy molecular orbitals, and the chromophore after absorbing the photons is excited. Due to the electron distribution, each chromophore has its own unique absorption maximum and molar absorptivity, corresponding to the wavelength/wavenumber and intensity of absorption peak in UV/Vis absorption spectra. Therefore, UV/Vis absorption spectroscopy can provide information about specific bonds or functional groups.

The Beer-Lambert law is the principle by which a UV/Vis spectrophotometer measures the concentration of absorbing species:

$$A = log_{10}\left(\frac{I_0}{I}\right) = \varepsilon c L$$

where A is the measured absorbance, I_0 and I are the incident light intensity and the transmitted intensity at a given wavelength, ε is the molar absorptivity or extinction coefficient, a constant related to the measurement atmosphere, and L is the path length through the sample, and c is the absorbing species concentration.

The UV/Vis spectrophotometer consists of three key components, as shown in Figure 2.10: a light source, a wavelength selector to isolate a narrow band of wavelengths near the desired analytical wavelength, and a detector to measure the intensity of the incident light transmitted by the sample.

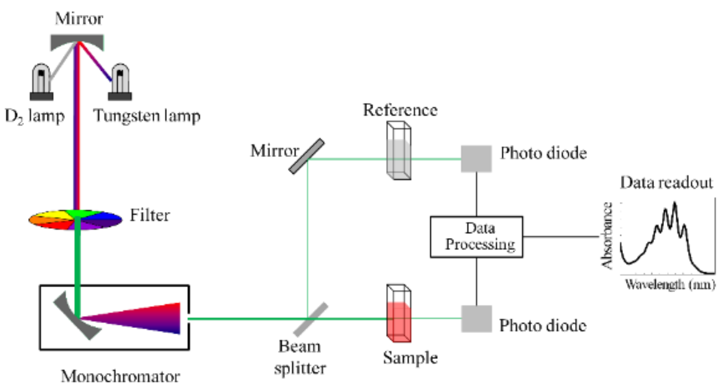

Figure 2.10 Schematic diagram of UV/Vis spectrophotometer.

2.2.9 High-performance liquid chromatography (HPLC)

Liquid chromatography (LC) is one of the fastest-growing techniques in analytical chemistry, used to separate, identify, and quantify each component in mixtures of organic, inorganic, pharmaceutical, and biochemical compounds. High performance liquid chromatography (HPLC) is an advanced LC with high operating pressures and modern equipment, columns, and column packing systems.

Figure 2.11 shows a schematic of an HPLC instrument: a pressurized liquid solvent (as a mobile phase) containing the sample mixture is pumped through a column filled with a solid adsorbent material (as a stationary phase). Each component in a mixture interacts slightly differently with the adsorbent material, resulting in different flow rates of components in the column, and leading to the separation of the components as they flow out of the column. The combination of a stationary phase and a mobile phase is crucial for the separation of components.

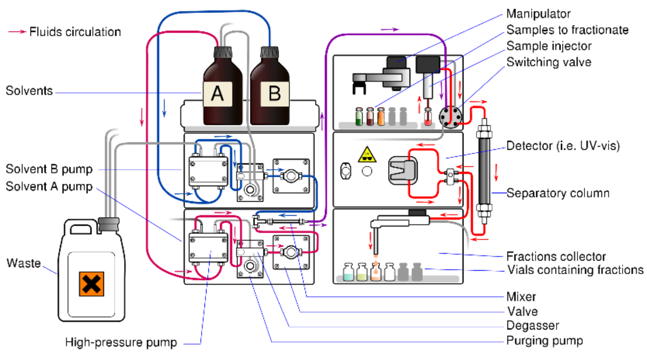

Figure 2.11 Schematic diagram of HPLC instrument.

HPLC can be used to perform qualitative and quantitative analyses. Qualitative analysis refers to the identification of components in a sample mixture: the chromatogram of the detected component is matched to a known component from the aspects of the retention times and shapes of peaks, or the separated components are analyzed via various detectors (e.g., infrared spectroscopy, nuclear magnetic resonance, and mass spectrometry). Quantitative analysis of the components in a sample is performed by the height or area of the component peak and a calibration curve of a standard.

Chapter III Effects of solvent and electrospinning parameters on the morphology and piezoelectric properties of PVDF nanofibrous membrane

Abstract

PVDF electrospun membranes were prepared by employing different mixtures of solvents and diverse electrospinning parameters. A comprehensive investigation was carried out, including morphology, nanofiber diameter, crystallinity, β-phase fraction, and piezoelectric response under external mechanical strain. It was demonstrated that by using low-toxicity DMSO as the solvent, PVDF membranes with good morphology (bead-free, smooth surface, and uniform nanofiber) can be obtained. All the fabricated membranes showed crystallinity and β-phase fraction above 48% and 80%, respectively; therefore, electrospinning is a good method for preparing PVDF membranes with piezoelectric properties. Moreover, we considered a potential effect of the solvent properties and the electrospinning parameters on the final piezoelectric properties. When PVDF membranes with different β-phase fractions and crystallinity values are applied to make the piezoelectric transducers, various piezoelectric voltage outputs can be obtained. This paper provides an effective and efficient strategy for regulating the piezoelectric properties of PVDF electrospun membranes by controlling both solvent dipole moment and process parameters. To the best of our knowledge, this is the first time that the influence of a solvent's dipole moment on the piezoelectric properties of electrospun materials has been reported.

Keywords: PVDF; nanofibrous membrane; electrospinning; piezoelectric properties

3.1 Introduction

Piezoelectric materials, which are extensively used in energy harvesting and sensors, have attracted much attention recently.[1,2] In brief, piezoelectric material can convert external mechanical strain into electric energy and vice-versa. Piezoelectric materials can be divided into three main categories: single crystals (e.g., quartz crystal), ceramics (e.g., lead zirconate titanate, $BaTiO_3$), and polymers (e.g., poly(vinylidene fluoride) (PVDF) and its copolymers, polylactic acid, and polyimides) [3]. Among them, piezoelectric polymers present specific advantages, such as lightweight, deformability, and flexibility; therefore, they have the potential to be employed as stretchable and flexible electronics.[3-5]

PVDF has become the most widely investigated piezoelectric polymer because of its excellent properties and low price.[4,6,7] PVDF is a polymorphic material and has distinct chain conformations in five crystalline phases: TTT (all-trans) planar zigzag for β phase, TGTG'(trans-gauche-trans-gauche) for α and δ phases, and T_3GT_3G' for γ and ε phases.[8] A strong electrical dipole moment exists in the PVDF monomer because the fluorine atom is more electronegative than hydrogen and carbon atoms, and it leads to piezoelectric properties. From the packing model of PVDF chain conformation, it can be concluded that there is no net dipole in α and ε phases, but there are net dipoles in β, γ, and δ phases.[9] Among these three phases, the β phase has the highest dipolar moment per unit cell and endues PVDF with the greatest piezoelectricity.[10,11]

The essence of improving the piezoelectric properties of PVDF is to improve the alignment of chain conformation. The main methods to improve the piezoelectric properties of PVDF are: (a) adding treatments, such as melt quenching[12] and stretching[13]; (b) blending with carbon materials[14,15], inorganic particles[16], piezoelectric ceramics[17], etc.; (c) adopting new process methods, such as electrospinning[18]; and (d) altering the structure[19] or surface morphology[11,20].

Electrospinning is a simple and versatile method for producing fiber membranes with a fiber diameter on the nanometer scale. It consists of three essential parts: a high-voltage supply, a spinneret with the polymer solution, and a grounded collector. A suitable solution is a key point for electrospinning. The polymer could be dissolved in a suitable solvent or melted at a high temperature to obtain a homogeneous and flowable polymer solution. Additionally, proper viscosity, surface tension, and conductivity are mandatory for solutions undergoing electrospinning. Under proper conditions, which means suitable processing parameters and ambient parameters, the polymer solution can form a stable Taylor cone at the tip of the spinneret. Then, the Taylor cone erupts to the collector when its electrostatic repulsion is equal to or higher than its surface tension. A nanofibrous membrane can be gathered on the collector, and its thickness depends on the electrospinning time. Processing parameters (voltage, tip-to-collector distance, and feed rate) and ambient parameters (humidity and temperature) influence the morphology and structure of the fiber.

As one of the most highly fluorinated polymers, PVDF is resistant to many standard organic solvents. In order to consume less time and effort finding soluble solvents for polymers, including PVDF, before the actual dissolution experiment, the Hansen solubility parameters[21] were introduced, which define the solubility of a polymer-solvent system. The radius of interaction (R_o) of a polymer defines a solubility sphere and is empirically calculated. δ_d, δ_p, and δ_h are the dispersion, polar, and hydrogen-bonding solubility parameters, respectively. Solvents with Hansen parameters within R_o can dissolve the polymer. The distance (R_a) between the solvent coordinate and the center of the polymer solubility sphere is calculated according to Equation (3.1):

$$R_a = \sqrt{4(\delta_d^p - \delta_d^s)^2 + (\delta_p^p - \delta_p^s)^2 + (\delta_h^p - \delta_h^s)^2} \tag{3.1}$$

where δ_d^p, δ_p^p, and δ_h^p are Hansen parameters for the polymer, and δ_d^s, δ_p^s, and δ_h^s are Hansen parameters for the solvent.[21,22] The ratio R_a/R_o is called the relative energy difference (RED). The polymer can be dissolved in a solvent when $R_a/R_o < 1$, whereas a solvent cannot dissolve the polymer when $R_a/R_o > 1$.[22] Bottino et al.[23] a solubility experiment of 46 kinds of solvents on PVDF and obtained the Hansen space of PVDF, which provided a direct criterion for judging the solubility of PVDF in each solvent.

Solubility supplies the possibility of preparing PVDF solution, which is a basic step in electrospinning a nanofibrous membrane. In addition, some properties of the solvents have effects on the final membrane morphology: evaporation rate influences not only the morphology but also the piezoelectric properties of cast film and electrospun membrane, as reported by Kim et al.[24] Moreover, the high dipole moment of the solvent is the main reason for the better piezoelectric properties of cast films.[25-27] Solution conductivity is also a key factor in controlling the diameter of nanofibers.[28]

The boiling point of the solvent corresponds to the temperature when the vapor pressure of the liquid is equal to the environmental pressure and is used to reflect the evaporation rate. A higher boiling point means a slower evaporation rate and vice-versa. Kim et al. [24] used three different solvents (DMF, DMF/ACE (6/4), and MEK) to prepare P(VDF-TrFE) electrospun nanofibrous membranes and studied the effects of these solvents on crystallization, fiber formation, and harvesting performance. They found that two key solvent properties (surface tension and evaporation rate) can affect the fiber diameter, degree of crystallization, and β-phase content.

Marcel Benz et al.[25] prepared PVDF cast films with different solvents and found that the PVDF films with a γ phase (polar phase) can be produced when the solvent has a high dipole moment. G. Knotts et al.[26] studied the influence of solvents (DMSO, DMF, and MEK) on the ferroelectric properties of PVDF-TrFE spin-cast film and found the film prepared with DMSO (highest dipole moment among three solvents) had excellent ferroelectric output. Kim et al.[27] conducted detailed and comprehensive work on the piezoelectric properties of P(VDF-TrFE) films using solvents with different dipole moments. They found solvents with a high dipole moment can lead to a P(VDF-TrFE) film with high piezoelectric and pyroelectric coefficients, as well as triboelectric properties.

The Hansen solubility parameters and the physical properties of the common soluble solvents for PVDF are listed in Table 3.1. It can be seen that DMF and DMSO with high dipolar moments are good solvents for PVDF, whereas THF and ACE with low dipolar moments are swelling solvents for PVDF.[23]

Solution conductivity determines the charge density of the polymer solution, which in turn controls the repulsion and bending extent during electrospinning. Consequently, it affects the final mean fiber diameter. Uyar and Besenbacher[28] applied different grades of DMFs with slightly different solution conductivities as the solvent for Polystyrene polymer solutions, and they investigated its effect on the morphology of the nanofibers (presence of beads, nanofiber mean diameter). They found that the higher the conductivity, the smaller the diameter of the fibers.

Table 3.1 The Hansen solubility parameters and physical properties of PVDF and various solvents.

Solvent	δ_d	δ_p	δ_h	R_a	**RED (R_a /R_o)** [1]	**Dipole Moment**	**Boiling Point**
Unit	$MPa^{1/2}$	$MPa^{1/2}$	$MPa^{1/2}$	$MPa^{1/2}$		D	℃
PVDF	17.2	12.5	9.2	0			
DMSO	18.4	16.4	10.2	4.68	0.936	3.96	189
DMF	17.4	13.7	11.3	2.45	0.49	3.82	153
ACE	15.5	10.4	7	4.56	0.912	2.85	56
THF	16.8	5.7	8	6.95	1.39	1.63	65

[1] *R_o of PVDF adopted=5, as suggested in the previous work*[22].

Piezoelectric materials can usually be produced through three main steps (melting, mechanical stretching, and electric polarization) to obtain the desired piezoelectric property. Electrospinning has been shown to be a good alternative technique, thanks to the principles that form the basis of all electrohydrodynamic technologies: high electric potential neutralizes some stray ions in solutions, and charge imbalance occurs; then, when the repulsive forces exceed surface tension, an electrified liquid jet is ejected from the tip of the needle, the solvent evaporates, and several electrical instabilities occur, causing the stretching of the jet and, finally, the solidification of nonwoven fibers. Consequently, the main advantage of the process is the ability to obtain mechanical stretching and polarization at the same time with relatively high throughput.

Many works[29,30] have focused on improving the piezoelectricity of PVDF nanofibrous membranes by controlling the electrospinning parameters. Gee et al.[29] synthesized a set of membranes with systematically variable electrospinning parameters (the fraction between DMF and ACE, tip-to-collector distance (TCD), flow rate, and voltage setting), and they ranked parameters according to the contribution of the β-phase fraction: solvent > flow rate > TCD > voltage. Singh et al.[30] studied the effects of eight electrospinning parameters on β-phase content and gave a detailed explanation. However, the connection between parameters and the relative contribution to the β-phase fraction was not investigated. Accordingly, the present work is meant to study the effect of the solvent properties and electrospinning parameters on the morphology, the β-phase fraction, the crystallinity, and the piezoelectric voltage output of PVDF nanofibrous membranes. Eight solvents with suitable solubility and evaporation rates were selected to study the impacts of dipole moment on piezoelectric properties. Different voltages, feed rates, and distances were altered to present the effect of electro-spinning parameters on piezoelectric properties. To the best of our knowledge, few papers have investigated the effect of solvents on the piezoelectric properties of PVDF electrospun nanofibrous membranes. In brief, this chapter provides an effective and efficient strategy for regulating the piezoelectric properties of PVDF membranes by electrospinning: controlling solution solvent and process parameters.

3.2 Experimental Section

3.2.1 Materials

PVDF (KYNAR 500) was purchased from Arkema (Colombes, France). Dimethyl sulfoxide (DMSO), N, N-dimethylformamide (DMF), acetone (ACE), and tetrahydrofuran (THF) were purchased from Sigma Aldrich (Burlington, MA, USA). All reagents were used as received without any further treatment.

3.2.2 Preparation of PVDF Solutions

To explore the effect of solvents on the PVDF nanofibrous membrane, a series of two solvent mixtures were prepared, as listed in Table 3.2. A total of 1 g PVDF powder was added to 6 g mixed solvent in a glass vial, and the solution was stirred for 8 h at room temperature, (20 ± 3) °C.

Table 3.2 Hansen solubility parameters and physical properties of the mixed solvents.

Solvent	δ_d	δ_p	δ_h	R_a	RED (R_a/R_o)	Dipole Moment	Boiling Point
unit	MPa $^{1/2}$	MPa $^{1/2}$	MPa $^{1/2}$	MPa $^{1/2}$		D	°C
DMF/ACE (2/1)	16.7	12.6	9.8	1.10	0.70	3.50	120.7
DMF/THF (1/1)	17.1	9.7	9.7	2.84	0.55	2.73	109.0
DMSO/ACE (2/1)	17.4	14.4	9.1	1.96	0.39	3.59	144.7
DMSO/ACE (1/1)	16.9	13.4	8.6	1.19	0.24	3.41	122.6
DMSO/ACE (2/3)	16.7	12.8	8.3	4.61	0.92	3.29	109.3
DMSO/THF (1/1)	17.6	11.1	9.1	1.66	0.33	2.80	127.0
DMSO/THF (1/2)	17.3	9.3	8.7	3.30	0.66	2.41	106.3

The Hansen solubility parameters and physical properties (dipole moment and boiling point) of the mixed solvents are listed in Table 3.2. All results of the mixture are expressed in terms of the weight ratio of the individual pure components.

3.2.3 Preparation of PVDF Nanofibrous Membrane

A 5 mL syringe loaded with PVDF solution was placed on a syringe pump with a feed rate of 0.5 mL h^{-1}. A 27 G stainless needle with an inner diameter of 0.4 mm was used as a spinneret, and it was connected to a high positive voltage supply. A stainless rotated flat plate covered with aluminum foil was used as the collector. The applied voltage and the tip-to-collector distance were 10 kV and 15 cm, respectively. A schematic diagram of the electrospinning setup can be found in Figure 3.1.

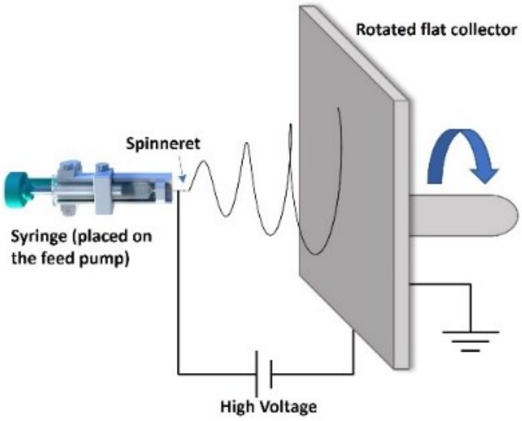

Figure 3.1 Schematic of the electrospinning setup utilized for the preparation of the PVDF nanofibrous membrane.

The solution of PVDF dissolved in DMSO/ACE (2/1) solvent was electrospun with different electrospinning parameters (voltages, feed rates, and distances) equal to all the other operating variables in order to investigate the influence of the electrospinning parameters on the PVDF nanofibrous membrane.

The process parameters of each membrane are listed in Table 3.3. All electrospinning processes were carried out in an atmospheric environment (temperature: 20 °C ± 3 °C, humidity: 45% ± 5%). Then, the collected membranes were dried in an oven at 60 °C for 6 h to remove the remaining solvent.

Table 3.3 Process parameters (solvent and electrospinning properties), nanofiber diameter, crystallinity, and β-phase fraction of the PVDF membranes.

Num.	Solvents	Dipole Moment	Boiling Point	Electrospinning Parameters	Diameter	Crystallinity (DSC)	β Phase (FTIR)
	unit	D	°C		nm	%	%
M1	DMF/ACE (2/1)	3.50	120.7		-[1]	-	-
M2	DMF/THF (1/1)	2.73	109.0		-	-	-
M3	DMSO/ACE (2/1)	3.59	144.7		992 ± 228.8	52.30	87.49
M4	DMSO/ACE (1/1)	3.41	122.6	10 kV, 1 mL/h, 15 cm	817 ± 176.3	51.61	86.88
M5	DMSO/ACE (2/3)	3.29	109.3		602 ± 203.8	51.25	86.36
M6	DMSO/THF (1/1)	2.80	127.0		1133 ± 225.9	50.27	84.70
M7	DMSO/THF (1/2)	2.41	106.3		1421 ± 221.7	48.67	81.91
M8				10 kV, 0.5 mL/h, 15 cm	658 ± 90.6	50.46	85.36
M9	DMSO/ACE (2/1)	3.59	144.7	10 kV, 0.5 mL/h, 30 cm	822 ± 129.4	50.37	86.42
M10				20 kV, 0.5 mL/h, 30 cm	734 ± 111.4	52.36	88.01

1 The properties of M1 and M2 were not studied further due to poor morphological quality.

3.3.4 Characterizations

The morphology of the membrane was observed by a scanning electron microscope (SEM) (JSM-6490, JEOL, Ltd., Tokyo, Japan) with a voltage of 15 kV, and all samples were sputtered with a thin Au layer before imaging. The mean diameter and standard deviation of nanofibers for each electrospun mat were obtained by randomly measuring 200 nanofibers from SEM images. The crystallinity of the PVDF membrane was analyzed by differential scanning calorimetry (DSC) (Q200, TA instruments, New Castle, DE, USA) using the heat-cool-heat procedure from 40 °C to 250 °C with a rate of 10 °C/min in a nitrogen atmosphere. The β-phase fraction of PVDF was analyzed by Fourier transform infrared spectroscopy (FTIR) (Nicolet Is50 spectrometer, Thermo Fisher Scientific, Waltham, MA, USA) in transmission mode, in the (1600650) cm^{-1} wavenumber range (64 scans, 4 cm^{-1} resolution).

3.2.5 The Piezoelectric Analysis

A piece of PVDF nanofibrous membrane (length*width*thickness: 60*16*0.6 mm^3) was sandwiched between the conductive side of two PET films. Two copper wires were attached to the two sides of the PVDF membrane through the silver paint. Later, the PI tape was used to pack and protect the whole transducer. The transducer was fixed on a 3-point bending clamp for dynamic mechanical analysis (DMA) (Q800, TA instruments, New Castle, DE, USA), which can supply a regular and controllable strain. Another end of two copper wires from the transducer was connected to an oscilloscope (LT322, LeCroy, New York, USA), which worked as the acquisition setup. The assembly method of the transducer and the working mode for analysis are shown in Figure 3.2.

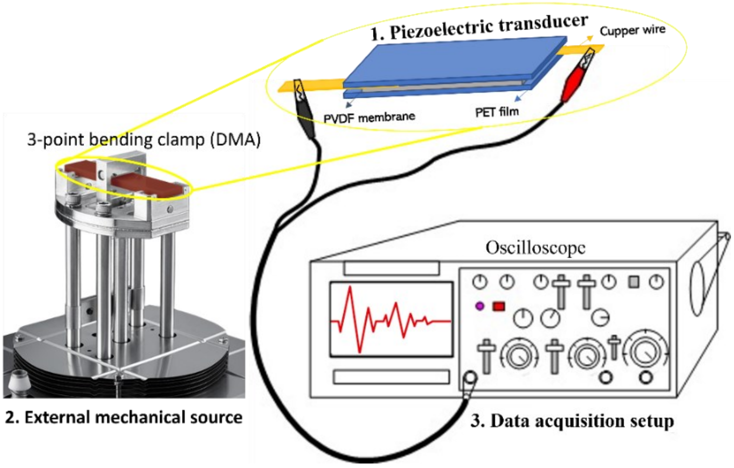

Figure 3.2 Schematic of the experimental setups utilized for piezoelectric analysis.

The same frequency (0.5 Hz) with different strains (1500 um, 2500 um, and 3000 um) and the same strain (2000 um) with different frequencies (0.25 Hz, 0.5 Hz, and 1 Hz) were applied on the transducer by DMA. The open-circuit voltage of the transducer under strain was recorded by the oscilloscope. Analyses under different conditions were performed twice at room temperature.

3.3 Results and Discussion

3.3.1 Effect of Solvent

DMF/ACE (2/1) and DMF/THF (1/1) are the common solvents used to prepare PVDF solutions for electrospinning in the literature. Figure 3.3 shows the SEM images of PVDF membranes (M1 and M2) prepared using these two solvents. Beads, nanofibers with nonuniform morphology and various diameters, can be found in the membranes. It can be seen from the literature[31,32] that when these solvents are applied, similar phenomena frequently occur in the PVDF membrane.

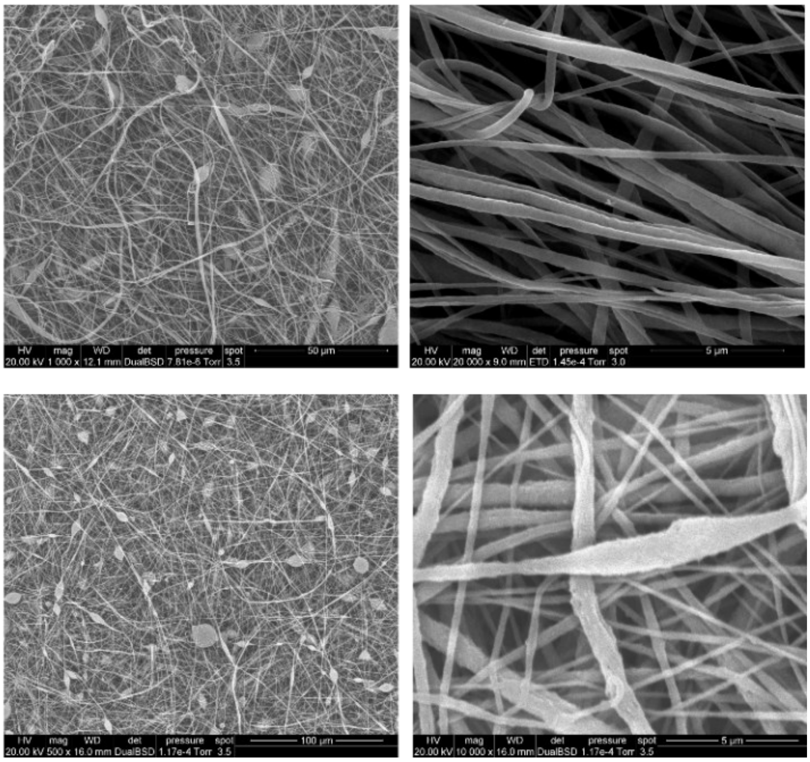

Figure 3.3 SEM images of PVDF nanofibrous membrane at two magnifications: (A) M1 (using DMF/ACE (2/1)) and (B) M2 (using DMF/THF (1/1)).

Figure 3.4 presents the SEM images at two magnifications and the diameter histogram of the PVDF nanofibrous membrane (M3-M7). From the SEM images at low magnification, it can be observed that these membranes consisted of nanofibers without defects, with morphology completely different from that of M1 and M2 in Figure 3.3 Another advantage of adopting DMSO as a solvent is its low toxicity, as emphasized by Russo et al. [33]

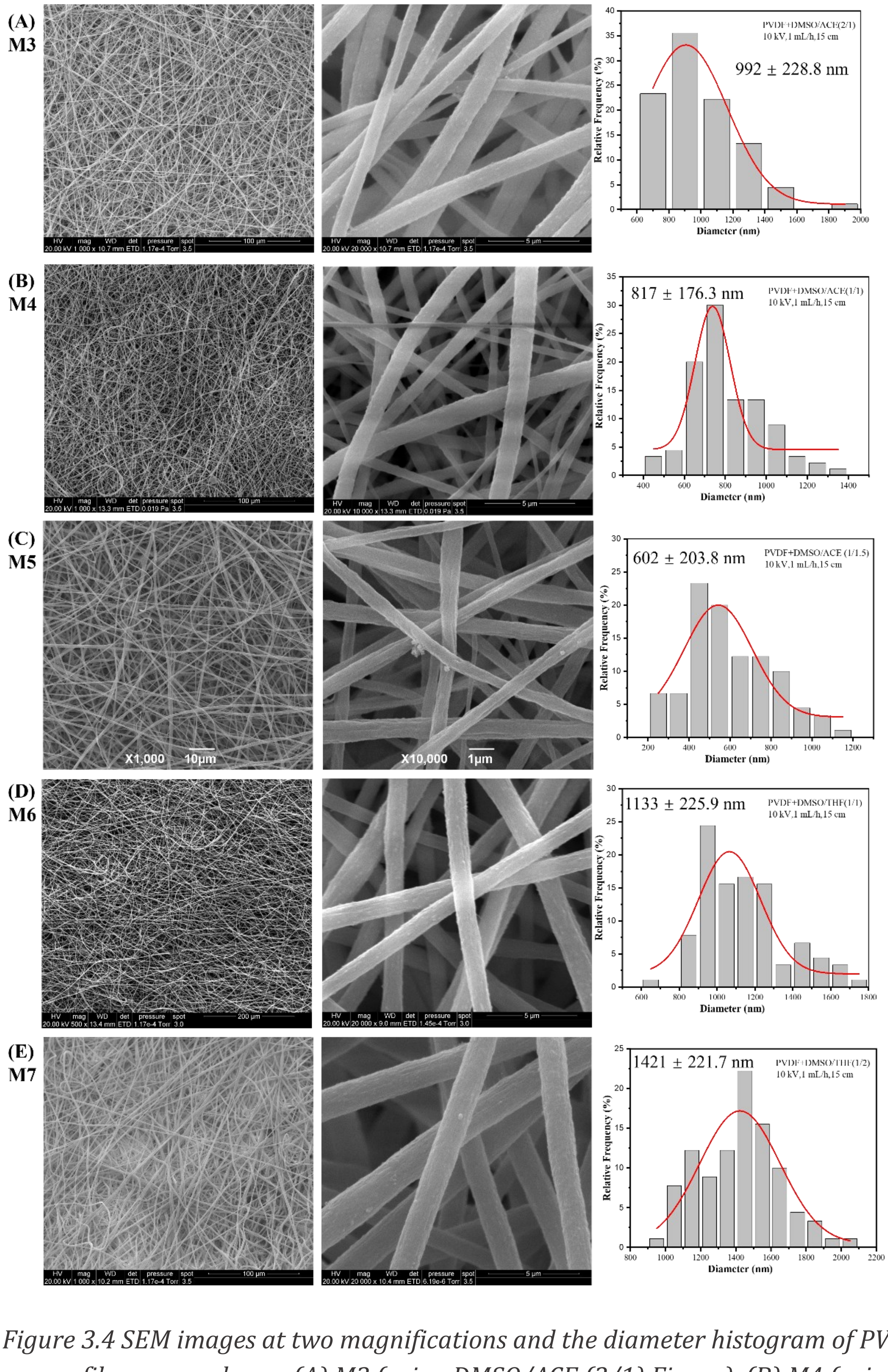

Figure 3.4 SEM images at two magnifications and the diameter histogram of PVDF nanofibrous membrane (A) M3 (using DMSO/ACE (2/1) Figure), (B) M4 (using DMSO/ACE (1/1)), (C) M5 (using DMSO/ACE (2/3)), (D) M6 (using DMSO/THF (1/1)), and (E) M7 (using DMSO/THF (1/2)).

From the SEM images at high magnification, the smooth surface and uniform shape of the nanofibers were observed. The difference in average diameter among membranes can be attributed to the evaporation-stretching function during the electrospinning process. More specifically, the solvent with low boiling temperature was completely evaporated during electrospinning. Then, nanofibers with small diameters were gathered on the collector; otherwise, the nanofiber with residual solvent reached the collector and presented a large diameter. The stretching of nanofibers during the process was determined by not only the electrospinning parameters but also the solution conductivity; high stretching definitely leads to high elongation of the jet, as well as the formation of uniform fibers with a small diameter. ACE has higher solution conductivity than DMSO, followed by THF, so the conductivity of the solvents was increased from M3 to M4 and from M5 to M6. From the diameter of each membrane, it can be concluded that the conductivity of solution has a more pronounced effect on the fiber diameter than evaporation.

The FTIR spectra of all the samples are reported in Figure 3.5. The peaks at 1400 cm^{-1}, 1171 cm^{-1}, 1071 cm^{-1}, and 874 cm^{-1} were related to the CH_2 wagging vibration, symmetrical stretching of -CF_2, C-C asymmetric stretching, and CF_2 symmetric stretching, respectively, and these are common bands for all the various PVDF phases. The peaks at 1275 cm^{-1} and 840 cm^{-1} were attributed to CF out-of-plane deformation and CH_2 rocking, and they were characteristic bands for the β phase of PVDF. The peak at 766 cm^{-1} was raised from CF_2 bending and skeletal bending, corresponding to the α phase[6,34-36].

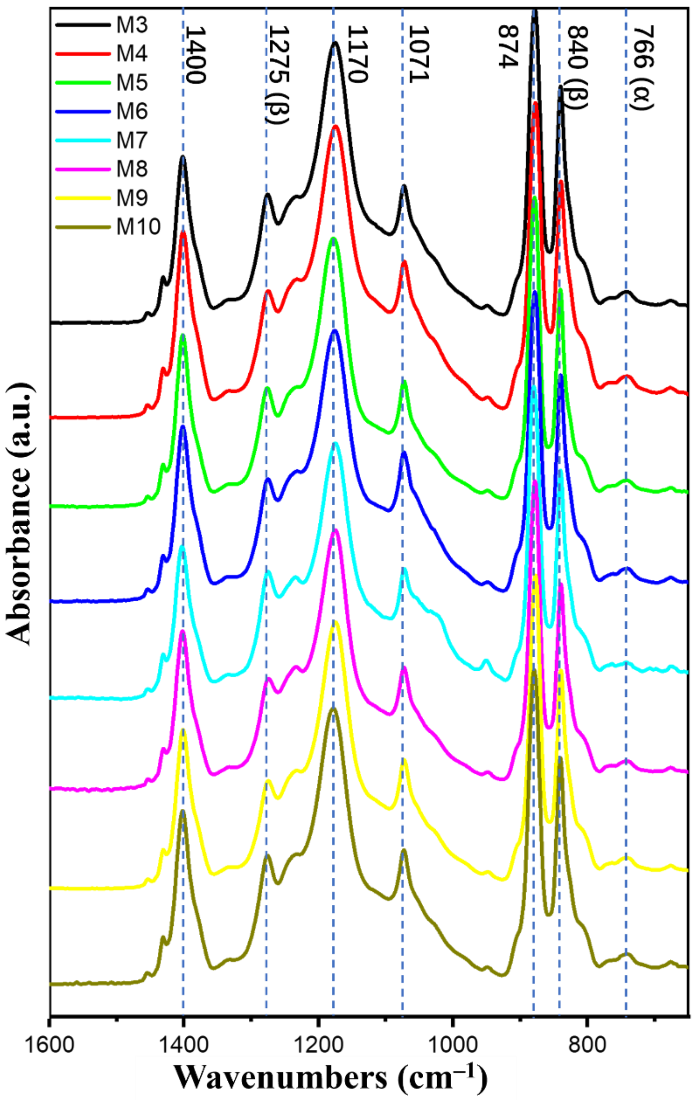

Figure 3.5 FTIR spectra of all PVDF nanofibrous membranes (M3-M10).

To clearly observe the difference in curves and simply explain the calculation of the β-phase fraction ($F(\beta)$), only the FTIR spectra of M7 and M10 are presented in Figure 3.6(A). $F(\beta)$ can be calculated using the Beer-Lambert Equation (2).

$$F(\beta)=\frac{A_\beta}{A_\beta+\frac{K_\beta}{K_\alpha}A_\alpha}\times 100\%. \quad (2)$$

where K_α ($6.1*10^4$ cm^2 mol^{-1}) and K_β ($7.7*10^4$ cm^2 mol^{-1}) are the absorption coefficients at 766 cm^{-1} and 840 cm^{-1}, respectively; and A_α and A_β are the absorbencies at 766 cm^{-1} and 840 cm^{-1}, respectively.[34]

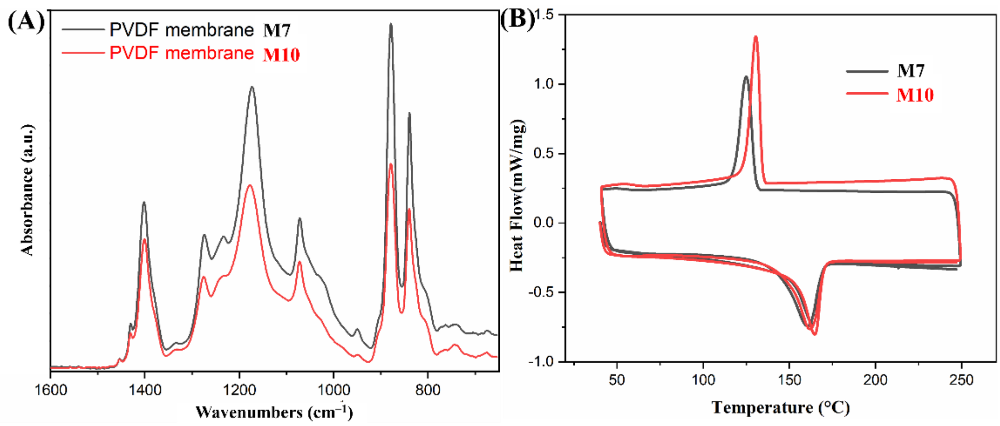

Figure 3.6 (A) FTIR spectra and (B) DSC curves of PVDF nanofibrous membranes (M7 and M10).

The average β-phase fractions at five different places on each membrane are summarized in Table 3.3 All electrospun membranes had a relatively high β-phase content (above 80%) compared with the membrane prepared by casting because of the voltage field and the stretch during the electrospinning process. On the other hand, a high β-phase fraction was obtained in the PVDF electrospun membrane when a solvent with a high dipole moment was used.

Figure 3.6(B) is the DSC curves of M7 and M10. Crystallinity is calculated according to Equation (3):

$$X_c = \frac{\Delta H}{\Delta H_{\mathrm{m}} \cdot \varphi} * 100\% \quad (3)$$

where ΔH is the melting enthalpy of the PVDF membrane obtained from the DSC curve, ΔH_{m} (104.7 J g^{-1}) is the melting enthalpy of PVDF with 100% crystallinity, and φ is the PVDF weight fraction. The endothermic peak of the second heating process was used to calculate the crystallinity.

The crystallinity summarized in Table 3.3 is the average of the three analyses. More than 50% crystallinity can be reached in the PVDF membrane through electrospinning. Furthermore, the relation between crystallinity and solvent showed a trend similar to that between β-phase content and solvent: the higher the dipole moment of the solvent, the higher the crystallinity of the PVDF membrane.

Consequently, the solvent affects not only the β-phase fraction but also the crystallinity. Adopting a solvent with a high dipole moment can produce a PVDF membrane with high β-phase content and high crystallinity. This effect on cast films has been previously reported with the explanation that solvents with a high dipole moment can enhance the end-to-end length and lead to the regular orientation of PVDF chains, which in turn results in dipole alignment and good piezoelectric properties of PVDF membranes.[27,37,38]

3.3.2 Effect of Electrospinning Parameters

The effects of electrospinning parameters on the crystallinity and β-phase content of PVDF membranes have been reported in published works[29,30]. Here, PVDF electrospun membranes (M3, M8-M10) with different voltages, feed rates, and distances were prepared, and we confirmed that the electrospinning parameters certainly influence the piezoelectric properties of PVDF membranes.

Figure 3.7 shows SEM images at two magnifications and the nanofiber diameter histogram of PVDF membranes prepared with different electrospinning parameters. Obviously, when the same solvent but different electrospinning parameters were adopted, uniform and bead-free PVDF membranes were synthesized. The ratio of voltage to distance can be regarded as the voltage field intensity. From M3 to M8, the diameter of nanofibers reduced due to the decrease in feed rate, which meant the same voltage field intensity was applied on less solution, or the same amount of solution was applied under higher voltage field intensity. From M8 to M9, a longer distance led to a lower voltage field intensity, which resulted in an increase in nanofiber diameter. The diameter decreased from M9 to M10 because the higher field intensity, generated by the higher voltage, provides a stronger force.

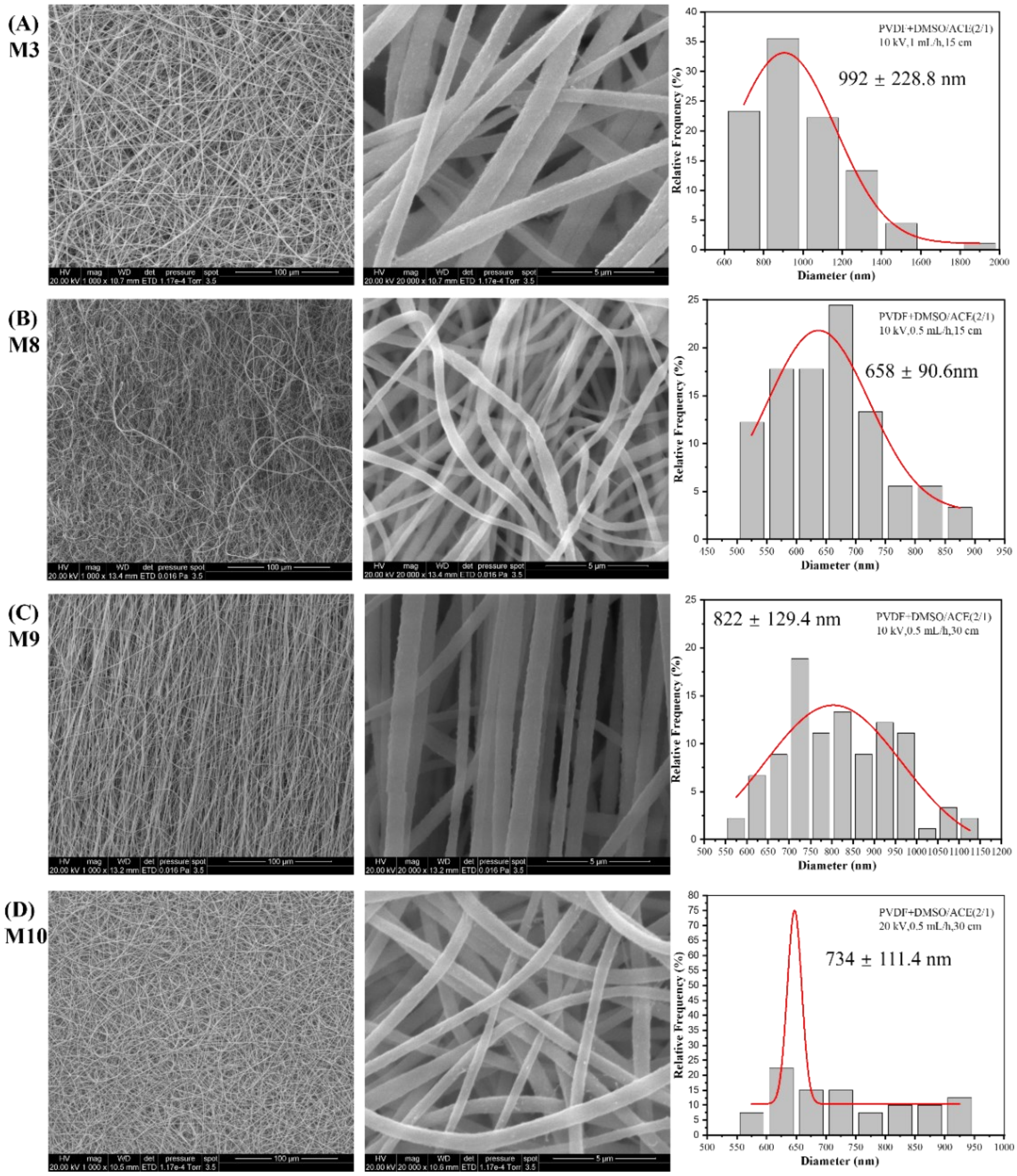

Figure 3.7 SEM images at two magnifications and the diameter histogram of PVDF nanofibrous membrane (A) M3 (using 10 kV, 1 mL/h, 15 cm), (B) M8 (using 10 kV, 0.5 mL/h, 15 cm), (C) M9 (using 10 kV, 0.5 mL/h, 30 cm), and (D) M10 (using 20 kV, 0.5 mL/h, 30 cm).

The β-phase fraction and the crystallinity are summarized in Table 3.3. The influence of electrospinning parameters on the β-phase fraction and crystallinity was present but insignificant, and it was even more difficult to detect any trends. Therefore, no more explanation about the influence can be given here.

As consequence, the solvent was the main factor that manipulated the morphology of the PVDF membranes, whereas electrospinning parameters had influences on the morphology (e.g., diameter, bead) of nanofibers. The effects of electrospinning parameters can be explained as follows: the voltage applies a stretching force on the jet from the needle, the feed rate determines the shape of the Taylor cone on the tip of the needle, and the distance affects the stretching time before reaching the collector. There are internal relations between these parameters, so it is impossible to discuss the impact of an individual parameter or attribute results to a single parameter.

3.3.3 Piezoelectric Analysis

M7 and M10 were selected for piezoelectric measurements because they presented the lowest and the highest crystallinity and β phase, respectively, among all the membranes. The open-circuit voltage as a function of time under various external strains is shown in Figure 8, and the piezoelectric voltage outputs (the value between the highest and lowest voltage) are summarized in Table 3.4. The voltage output increased with increased amplitude and remained stable with the change in frequency, as previously observed by Chen et al.[39]. With the progress of the piezoelectric measurements (especially after the measurements at 3000 um-0.5 Hz), the transducers became more flexible and therefore more easily stretched under the same strain with respect to the beginning conditions. Consequently, the voltage output of the transducer at 2000 um-0.5 Hz was higher than that at 2500 um-0.5 Hz.

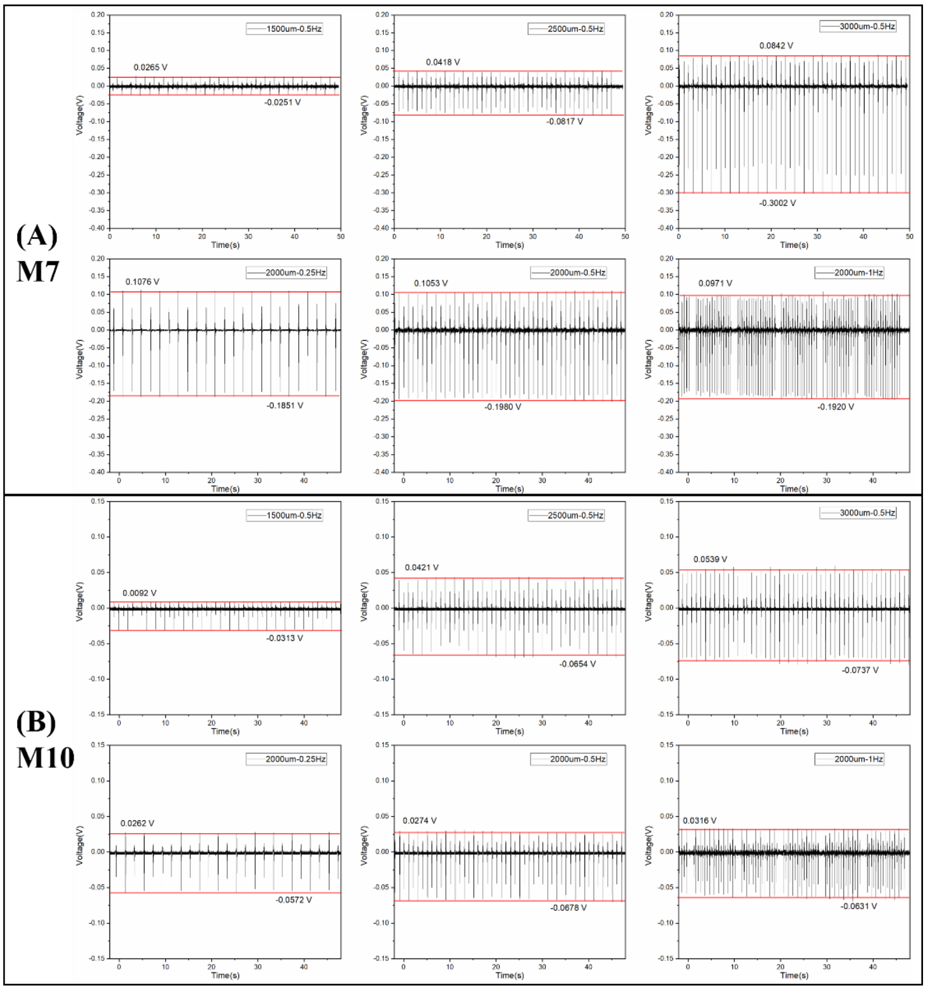

Figure 3.8 The open-circuit voltage of the transducers is made of PVDF membranes (A) M7 and (B) M10 as a function of time under different amplitudes and frequencies.

Table 3.4 Piezoelectric voltage outputs of transducers made of M7 and M10 under different amplitudes and frequencies.

Sample		M7	M10
Different amplitude	1500 um-0.5 Hz	39.1 mV	48.8 mV
	2500 um-0.5 Hz	106.4 mV	111.8 mV
	3000 um-0.5 Hz	119.9 mV	369.7 mV
Different frequency	2000 um-0.25 Hz	83.4 mV	285.7 mV
	2000 um-0.5 Hz	88.2 mV	298.6 mV
	2000 um-1 Hz	94.7 mV	289.1 mV

Comparing the voltage output of the transducers made of M7 and M10, it can be seen that the voltage outputs of M10 were always higher than those of M7 under the different external strains. Hence, M10 had a higher piezoelectric response than M7, which corresponded to the higher crystallinity and higher β-phase fraction of M10.

3.4 Conclusions

This work provides new insight into the preparation of PVDF electrospun membranes with piezoelectric properties based on the dipole moment of solvents. The morphology, nanofiber diameter, crystallinity, and β-phase fraction of the synthesized PVDF membrane were studied, and piezoelectric analysis of the transducers made of two PVDF membranes was carried out. When DMSO with good solubility for PVDF and low toxicity was used, membranes with good morphology were obtained. When DMSO/ACE (2/1) with high dipole moment was used as the solvent, PVDF electrospun membranes exhibited a higher crystallinity, β-phase fraction, and piezoelectric output than that prepared with DMSO/THF (1/2). Based on the presented analysis, we found that solvents with a high dipole moment can improve piezoelectric properties, and the evaporation rate and solvent conductivity can influence nanofiber diameter. On the other hand, electrospinning parameters can also control nanofiber diameter and piezoelectric properties during the electrospinning process, although the effect of the solvents is much more straightforward. Therefore, selecting a proper solvent can be considered a simple method to control the piezoelectric performance of PVDF membranes.

References

(1) Kim, H. S.; Kim, J.-H.; Kim, J. A review of piezoelectric energy harvesting based on vibration. *International journal of precision engineering and manufacturing* **2011**, *12*, 1129-1141.

(2) Smith, M.; Kar-Narayan, S. Piezoelectric polymers: Theory, challenges and opportunities. *International Materials Reviews* **2022**, *67*, 65-88.

(3) Mishra, S.; Unnikrishnan, L.; Nayak, S. K.; Mohanty, S. Advances in Piezoelectric Polymer Composites for Energy Harvesting Applications: A Systematic Review. *Macromolecular Materials and Engineering* **2019**, *304*, 1800463.

(4) Fan, F. R.; Tang, W.; Wang, Z. L. Flexible nanogenerators for energy harvesting and self-powered electronics. *Advanced Materials* **2016**, *28*, 4283-4305.

(5) Han, M.; Wang, H.; Yang, Y.; Liang, C.; Bai, W.; Yan, Z.; Li, H.; Xue, Y.; Wang, X.; Akar, B. Three-dimensional piezoelectric polymer microsystems for vibrational energy harvesting, robotic interfaces and biomedical implants. *Nature Electronics* **2019**, *2*, 26-35.

(6) Yin, J.; Roso, M.; Boaretti, C.; Lorenzetti, A.; Martucci, A.; Modesti, M. PVDF-TiO2 core-shell fibrous membranes by microwave-hydrothermal method: Preparation, characterization, and photocatalytic activity. *Journal of Environmental Chemical Engineering* **2021**, *9*, 106250.

(7) Vazquez, B.; Vasquez, H.; Lozano, K. Preparation and characterization of polyvinylidene fluoride nanofibrous membranes by forcespinning™. *Polymer Engineering & Science* **2012**, *52*, 2260-2265.

(8) Arunachalam, P.: Polymer-based nanocomposites for energy and environmental applications. In *Polymer-based Nanocomposites for Energy and Environmental Applications*; Elsevier, 2018; pp 185-203.

(9) Yu, Y.-J.; McGaughey, A. J. Energy barriers for dipole moment flipping in PVDF-related ferroelectric polymers. *The Journal of chemical physics* **2016**, *144*, 014901.

(10) Kabir, E.; Khatun, M.; Nasrin, L.; Raihan, M. J.; Rahman, M. Pure β-phase formation in polyvinylidene fluoride (PVDF)-carbon nanotube composites. *Journal of Physics D: Applied Physics* **2017**, *50*, 163002.

(11) Martins, P.; Lopes, A.; Lanceros-Mendez, S. Electroactive phases of poly (vinylidene fluoride): Determination, processing and applications. *Progress in polymer science* **2014**, *39*, 683-706.

(12) Gu, M.; Zhang, J.; Wang, X.; Ma, W. Crystallization behavior of PVDF in PVDF-DMP system via thermally induced phase separation. *Journal of applied polymer science* **2006**, *102*, 3714-3719.

(13) Li, L.; Zhang, M.; Rong, M.; Ruan, W. Studies on the transformation process of PVDF from α to β phase by stretching. *RSC Advances* **2014**, *4*, 3938-3943.

(14) Zhang, Y. Y.; Jiang, S. L.; Yu, Y.; Zeng, Y. K.; Zhang, G. Z.; Zhang, Q. F.; He, J. G. Crystallization behavior and phase-transformation mechanism with the use of graphite nanosheets in poly(vinylidene fluoride) nanocomposites. *Journal of Applied Polymer Science* **2012**, *125*, E314-E319.

(15) Qamar, Z.; Zakria, M.; Shakoor, R. I.; Raffi, M.; Mehmood, M.; Mahmood, A. Reinforcement of electroactive characteristics in polyvinylidene fluoride electrospun nanofibers by intercalation of multi-walled carbon nanotubes. *J Polym Res* **2017**, *24*.

(16) Ye, H. J.; Shao, W. Z.; Zhen, L. Crystallization kinetics and phase transformation of poly(vinylidene fluoride) films incorporated with functionalized baTiO3 nanoparticles. *Journal of Applied Polymer Science* **2013**, *129*, 2940-2949.

(17) Jain, A.; KJ, P.; Sharma, A. K.; Jain, A.; PN, R. Dielectric and piezoelectric properties of PVDF/PZT composites: A review. *Polymer Engineering & Science* **2015**, *55*, 1589-1616.

(18) Zheng, J. F.; He, A. H.; Li, J. X.; Han, C. C. Polymorphism control of poly(vinylidene fluoride) through electrospinning. *Macromol Rapid Comm* **2007**, *28*, 2159-2162.

(19) Pan, C.-T.; Yen, C.-K.; Wang, S.-Y.; Lai, Y.-C.; Lin, L.; Huang, J.; Kuo, S.-W. Near-field electrospinning enhances the energy harvesting of hollow PVDF piezoelectric fibers. *Rsc Advances* **2015**, *5*, 85073-85081.

(20) Zaarour, B.; Zhu, L.; Huang, C.; Jin, X. Enhanced piezoelectric properties of randomly oriented and aligned electrospun PVDF fibers by regulating the surface morphology. *Journal of Applied Polymer Science* **2019**, *136*, 47049.

(21) Hansen, C. M.: *Hansen solubility parameters : a user's handbook*; CRC Press: Boca Raton, 2007.

(22) Ma, J.; Larsen, R. M. Use of Hansen solubility parameters to predict dispersion and strain transfer of functionalized single-walled carbon nanotubes in poly (vinylidene fluoride) composites. *Journal of Thermoplastic Composite Materials* **2014**, *27*, 801-815.

(23) Bottino, A.; Capannelli, G.; Munari, S.; Turturro, A. Solubility parameters of poly (vinylidene fluoride). *Journal of Polymer Science Part B: Polymer Physics* **1988**, *26*, 785-794.

(24) Kim, M.; Lee, S.; Kim, Y.-i. Solvent-controlled crystalline beta-phase formation in electrospun P (VDF-TrFE) fibers for enhanced piezoelectric energy harvesting. *APL Materials* **2020**, *8*, 071109.

(25) Benz, M.; Euler, W. B.; Gregory, O. J. The role of solution phase water on the deposition of thin films of poly (vinylidene fluoride). *Macromolecules* **2002**, *35*, 2682-2688.

(26) Knotts, G.; Bhaumik, A.; Ghosh, K.; Guha, S. Enhanced performance of ferroelectric-based all organic capacitors and transistors through choice of solvent. *Applied Physics Letters* **2014**, *104*, 84_81.

(27) Kim, J.; Lee, J. H.; Ryu, H.; Lee, J. H.; Khan, U.; Kim, H.; Kwak, S. S.; Kim,

S. W. High-performance piezoelectric, pyroelectric, and triboelectric nanogenerators based on P (VDF-TrFE) with controlled crystallinity and dipole alignment. *Advanced Functional Materials* **2017**, *27*, 1700702.

(28) Uyar, T.; Besenbacher, F. Electrospinning of uniform polystyrene fibers: The effect of solvent conductivity. *Polymer* **2008**, *49*, 5336-5343.

(29) Gee, S.; Johnson, B.; Smith, A. Optimizing electrospinning parameters for piezoelectric PVDF nanofiber membranes. *J Membrane Sci* **2018**, *563*, 804-812.

(30) Singh, R. K.; Lye, S. W.; Miao, J. Holistic investigation of the electrospinning parameters for high percentage of β-phase in PVDF nanofibers. *Polymer* **2021**, *214*, 123366.

(31) Mokhtari, F.; Latifi, M.; Shamshirsaz, M. Applying the Genetic Algorithm for Determination Electrospinning Parameters of Poly Vinylidene Fluoride (PVDF) Nano Fibers: Theoretical & Experimental Analysis. *J Textile Eng Fashion Technol* **2017**, *3*, 00098.

(32) Cozza, E. S.; Monticelli, O.; Marsano, E.; Cebe, P. On the electrospinning of PVDF: influence of the experimental conditions on the nanofiber properties. *Polym Int* **2013**, *62*, 41-48.

(33) Russo, F.; Ursino, C.; Avruscio, E.; Desiderio, G.; Perrone, A.; Santoro, S.; Galiano, F.; Figoli, A. Innovative Poly (Vinylidene Fluoride)(PVDF) electrospun nanofiber membrane preparation using DMSO as a low toxicity solvent. *Membranes* **2020**, *10*, 36.

(34) Cai, X.; Lei, T.; Sun, D.; Lin, L. A critical analysis of the α, β and γ phases in poly (vinylidene fluoride) using FTIR. *RSC advances* **2017**, *7*, 15382-15389.

(35) Elashmawi, I.; Hakeem, N. Effect of PMMA addition on characterization and morphology of PVDF. *Polymer Engineering & Science* **2008**, *48*, 895-901.

(36) Barrau, S.; Ferri, A.; Da Costa, A.; Defebvin, J.; Leroy, S.; Desfeux, R.; Lefebvre, J.-M. Nanoscale investigations of α-and γ-crystal phases in PVDF-based nanocomposites. *Acs Appl Mater Inter* **2018**, *10*, 13092-13099.

(37) Tung, K.-L.; Lu, K.-T.; Ruaan, R.-C.; Lai, J.-Y. Molecular dynamics study of the effect of solvent types on the dynamic properties of polymer chains in solution. *Desalination* **2006**, *192*, 380-390.

(38) Salimi, A.; Yousefi, A. A. Conformational changes and phase transformation mechanisms in PVDF solution-cast films. *Journal of Polymer Science Part B: Polymer Physics* **2004**, *42*, 3487-3495.

(39) Chen, J.; Nabulsi, N.; Wang, W.; Kim, J. Y.; Kwon, M.-K.; Ryou, J.-H. Output characteristics of thin-film flexible piezoelectric generators: A numerical and experimental investigation. *Applied Energy* **2019**, *255*, 113856.

Chapter IV PVDF-TiO_2 core-shell fibrous membranes by microwave-hydrothermal method: preparation, characterization, and photocatalytic activity

Abstract

A polyvinylidene fluoride (PVDF)-titanium dioxide (TiO_2) core-shell composite nanofibrous membrane (CNM) with photocatalytic activity was obtained from the microwave-assisted hydrothermal treatment of an electrospun PVDF membrane. The effects of the precursor solution acidity, the heating temperature, and the treatment time on the structure and the photocatalytic performance were investigated. The CNM obtained from a 2 M precursor acidic solution showed the presence of nanofibers (NFs) with a proper core-shell structure, wherein a TiO_2 smooth shell was uniformly covering the electrospun PVDF NFs core. The TiO_2 crystallographic phase was found to be temperature-dependent, with the highest anatase content observed at 120 °C. The mean PVDF-TiO_2 NFs diameter measured from SEM images and the TiO_2 fraction of CNM calculated from TGA results showed an accumulation of TiO_2 on the PVDF NFs surface as heating temperature and treatment time increased. The photo-oxidation capability of the as-prepared CNMs was evaluated by the photocatalytic decomposition of aqueous methyl orange solution at room temperature under UV-C irradiation. PVDF-TiO_2 CNM exhibited a stable performance after five cycles of methyl orange degradation due to a strong connection between the TiO_2 layer and the PVDF substrate. The implemented approach has been demonstrated to be a feasible method for the synthesis of core-shell PVDF-TiO_2 fibrous membrane. The influence of hydrothermal process parameters on the structure and final properties of PVDF-TiO_2 CNM was revealed through a detailed mechanism investigation.

Keywords： microwave-hydrothermal method, core-shell composite nanofibrous membrane, photocatalysis, wastewater treatment.

4.1 Introduction

Photocatalysis[1-4] is an important process that belongs to the category of advanced oxidation processes that uses appropriate light irradiation to activate, for example, semiconductor metal oxides. Metal oxides, like zinc oxide (ZnO)[5], titanium dioxide (TiO_2)[6,7], ferric oxide (Fe_2O_3)[8,9], and bismuth oxide (Bi_2O_3)[10], are used as photocatalysts due to their short band gap and easy production. Light irradiation, with photon energy higher than or equal to the band gap, causes electrons to jump from the valence band to the conduction band, resulting in the generation of holes in the valence band[11]. Further reactions between the electron-hole pairs and oxygen or water can produce reactive oxygen species (ROS; such as $O_2^{\cdot -}$ H_2O_2, $^{\cdot}OH$) that can act as strong oxidizing agents, with the ability to degrade various organic pollutants.[12]

Among the above metal oxides, TiO_2 has been extensively investigated as a photocatalyst due to its chemical inertness, photostability, nontoxicity, and low cost.[13,14] It is well known that TiO_2 has three common crystal structures in nature: rutile, anatase, and brookite.[13,15] Rutile is the most stable phase from the thermodynamic point of view, while brookite has received less research attention due to its complex structure.[16] Metastable anatase is considered the most active phase and is used widely as photocatalyst.[17,18]

The microwave-assisted hydrothermal method (MAHM), a combination of the hydrothermal method and microwave heating, has recently gained popularity to prepare functional nanomaterials.[19-21] The MAHM is able to reach a high and uniform temperature in a short period thanks to the high-frequency electromagnetic radiation that directly interacts with the permanent dipole of the material.[22] Consequently, the crystal structure and the morphology of the obtained products are homogeneous over the whole sample.[20] Another advantage of the MAHM is that it requires a lower reaction temperature or a shorter treatment time than other preparation methods, like the sol-gel method and chemical vapor deposition, as it can reach a high pressure in a sealed reactor, which can accelerate those reactions favored by a pressure increase.[20]

There have recently been plenty of reports regarding the synthesis of TiO_2 by MAHM.[23-28] Most notably, Komarneni S et al.[23] were the first researchers who used this technique to prepare crystalline oxide powders, including TiO_2. Yang et al.[24] synthesized the TiO_2 microsphere, with a completely crystallized anatase phase, that was able to photo-catalytically decontaminate both Cr(VI) and methyl orange (MO).

TiO_2 nanoparticles (NPs) may be difficult to separate and recycle when employed as a photocatalyst for a liquid-phase treatment. To overcome this problem, a polymeric substrate can be selected to immobilize TiO_2 NPs because it is convenient to operate during the separation process. Thanks to its large surface area, the electrospun fibrous membrane is a good candidate as the substrate for NPs from variant forms of polymer.[29]

Poly(vinylidene fluoride) (PVDF) is a well-known semi-crystalline polymer with outstanding mechanical properties (such as good formability[30], high chemical resistance[31,32], ultrahigh strength[33,34], and excellent thermal and UV stability[35,36]), which can be considered as a support for TiO_2 NPs[37] for photocatalysis[38]. Many studies have focused on the preparation of composites of TiO_2 and PVDF with different experimental design strategies, such as varying the incorporation method and changing the operation orders of TiO_2 and PVDF.[39-45]

A catalyst-based polymer nanofiber membrane was prepared by Roso et al.[43] to degrade both acetaldehyde and methanol gas by a one-step electrospinning method, in which the spinning solution consisted of polymer (PVDF) and catalyst (pure TiO_2 or Ag_2CO_3/GO modified TiO_2).

Dong et al.[40] synthesized in-situ TiO_2 NPs with high adhesion on PVDF nanofibers (NFs). The reported process used the following steps: i) Electrospinning of a PVDF solution with titanium precursor; ii) cold plasma treatment (to increase the bonding between titanium source and PVDF support); iii) hydrothermal reaction (to grow TiO_2 crystal phase). This work has provided a strategy to improve the interaction between the support and substrate. Furthermore, the TiO_2-PVDF membrane prepared in this manner exhibited improved performance towards CO_2 photoreduction.

TiO_2 NPs with different crystalline phases and morphologies on the surface of PVDF NFs were prepared in different acidic solutions using the hydrothermal method by Zhang et al.[42]. The TiO_2/PVDF with the highest photodegradation efficiency was the one hydrothermally synthesized in H_2SO_4.

There were nonetheless concerning aspects regarding the migration of the catalysts or their precursors within the bulk of the electrospun fibers, with a consistent reduction of their active form on the surface[46] and consequently lower performance.[47] Therefore, in order to ensure the maximum amount of catalyst on the NFs surface, the growth of TiO_2 on the surface of electrospun PVDF nanofiber membrane (which acts as polymeric support) by MAHM has been chosen in this work as a fast and effective method. On the other hand, a strong interaction between TiO_2 NPs and PVDF NFs can be obtained by hydrothermal treatment[44], which means that the PVDF-TiO_2 composite nanofiber membrane (CNM) can be recycled and reused without significant loss of TiO_2 NPs or reducing catalytic efficiency. To the best of our knowledge, there are only a few papers related to the synthesis of catalysts on the surface of NFs by MAHM, and just one reported a detailed and systematic study of the process parameters' effects on the PVDF-TiO_2 NFs morphology.

To obtain a PVDF-TiO_2 CNM with the desired properties and high catalytic performance, three main parameters related to the MAHM were considered: i) acidity of precursor solution; ii) heating temperature; iii) treatment time. The effects of these parameters were evaluated in terms of PVDF-TiO_2 CNM structure (morphology, TiO_2 crystalline phase, and coverage efficiency) and photocatalytic activity (degradation of MO). A detailed mechanism of TiO_2 formation, and rationalization of the effect of various parameters during hydrothermal treatment, have been proposed. Moreover, the properties of PVDF-TiO_2 CNM before and after photocatalysis have been compared to confirm the stability of the membranes.

In summary, we report a detailed study on the PVDF-TiO_2 CNMs production by a simple and efficient method that provides an effective strategy for catalyst immobilization, a potential feature in the field of innovative media for water treatment.

4.2 Experimental section

4.2.1 Materials

PVDF (KYNAR 500) was purchased from Arkema. Acetone (ACE), N, N-Dimethylformamide (DMF), and sulphuric acid (H_2SO_4) were purchased from Sigma Aldrich. Tetrabutyl titanate (TBOT), ethyl alcohol, and MO were purchased from Alfa Aesar. All reagents were used as received without any further treatment. Deionized water was used throughout all experiments.

4.2.2 Preparation of PVDF NFs membrane

4 g of PVDF powder was added into a 22.67 g solvent mixture of DMF and ACE with a volume ratio of 2:1 and stirred overnight at room temperature to prepare a 15 wt% PVDF solution for electrospinning.

A 5 mL syringe loaded with the PVDF solution was placed on a syringe pump with a flow rate of 0.5 mL h^{-1}. A 27 G stainless needle with an inner diameter of 0.4 mm was used as the nozzle and was connected to an electrode with a high positive voltage supply. A stainless drum covered with aluminum foil was used as the collector, and its rotation rate was set at 4000 rpm. The voltage applied to the needle and the distance between the collector and nozzle were 20 kV and 20 cm, respectively.

The electrospinning process was carried out in an atmospheric environment with a temperature of (20 ± 3) ℃ and humidity of (45 ± 5) %. After electrospinning, the collected membrane was dried in an oven at 60 ℃ for 6 h to remove the remaining solvent.

4.2.3 Preparation of PVDF-TiO_2 CNM

1 mL TBOT was hydrolyzed in 30 mL H_2SO_4 with the acidity of 1 M, 2 M, and 3 M under stirring. Then a piece of PVDF membrane was dipped into the solution, keep stirring for about 10 min, and then the transparent solution with wet membrane was transferred into a Teflon-lined autoclave with a volume of 100 mL. The hydrothermal reactions were carried out in a microwave oven (Micro SYNTH) at 100 °C, 120 °C, and 140 °C for 0.5 h, 1 h, 2 h, and 3 h, separately. All the variables and their levels are present in Table 4.1.

After the hydrothermal reaction, the as-synthesized membranes were entirely washed with deionized water and ethyl alcohol and dried in the oven at 60 °C for 6 h.

Table 4.1 The variables and levels used for preparing PVDF-TiO_2 CNM.

Variables	Levels			
Acidity of precursor solution	1 M	2 M	3 M	
Heating temperature	100 °C	120 °C	140 °C	
Treatment time	0.5 h	1 h	2 h	3 h

4.2.4 Characterizations

The morphology of NFs was characterized by scanning electron microscope (SEM) (JSM-6490, JEOL, Ltd.) with a voltage of 15 kV, and with all samples gold-sputtered before imaging. The mean diameter with a standard deviation of NFs under different parameters was determined by randomly measuring 80 NFs from 4 SEM images with two magnifications. Differential scanning calorimetry (DSC) (Q200, TA Instruments) was used for evaluating the melting point of the polymeric support. The status and existence of PVDF were analyzed by Fourier transform infrared spectroscopy (FTIR) (Nicolet Is50 spectrometer, Thermo Fisher Scientific), working in transmission mode, in the 4000-650 cm^{-1} wavenumber range (64 scans, 4 cm^{-1} resolution). Static contact angle analysis of water droplet was carried out by a Kruss DSA 100E, performing measurements after 5 s contacting in 5 different positions on both sides of the medium to confirm the uniform distribution of TiO_2. The crystalline phase of PVDF-TiO_2 CNM was determined by Wide-angle X-ray diffraction (WXRD) using an X' Pert PRO diffractometer with radiation (Cu, Kα, 50 kV, 40 mA). Thermogravimetric analysis (TGA) (Q600, TA instruments) of the membranes was performed from room temperature to 700 °C at a heating rate of 20 °C min^{-1} in an air atmosphere to evaluate TiO_2 content. The surface area of CNM was determined by an autosorb iQ (ASiQwin, Quantachrome) system using a 5-points Brunauer-Emmett-Teller (BET) method. Further evaluation of the absorption limit and the band-gap of PVDF-TiO_2 CNM were obtained by diffuse reflectance spectroscopy (DRS) using an Ultraviolet-Visible-Near Infrared spectrophotometer (V-570, JASCO) with an integrating sphere attachment, in the range of (200-650) nm. The absorbance of MO solutions was analyzed by using the same spectrophotometer but with a liquid cell holder and a 300-650 nm scanning range.

4.2.5 Photocatalytic activity

The catalytic activity under UV irradiation was monitored through the photodegradation of MO solutions. A schematic diagram of the photocatalytic reactor is shown in Figure 4.1. A quartz tube containing a UV-C lamp (254 nm, 15 W, Philips) was inserted into a photocatalytic reactor with a water-cooling jacket. PVDF-TiO_2 CNM with a total weight of 32 mg was added to a 200 mL MO aqueous solution at a concentration of 2.5 mg L^{-1}. The effect of UV-C light on MO photooxidation was tested without the PVDF-TiO_2 CNM and set as a blank experiment. The air bubble was supplied by an airflow of 2 NL min^{-1} from the bottom of the reactor. The solution was shaken by air bubbles in the dark for 30 min to reach the adsorption-desorption equilibrium between MO and catalyst. Subsequently, since UV illumination was on, 3 mL samples were withdrawn from the solution at regular intervals, analyzed by UV visible spectrophotometry, and evaluated the absorbance at 465 nm. A calibration curve of MO (concentration vs absorbance at 465 nm) was performed previously for the quantitative analysis. The selected intervals and the initial concentration were defined as C and C_0, respectively, and the relative concentration was expressed as C/C_0. To better understand the catalytic activity of PVDF-TiO_2 CNM, the relative concentration C/C_0 of each CNM was subtracted by that of the blank and defined as $C/C_0{}'$ (Equation 3.1). The difference between the MO degraded mass (mg) of each CNM and that of the blank was called m'_{MO}, then normalized by the TiO_2 amount on each CNM, m'_{MO}/m_{TiO_2} (Equation 3.2).

$$\left(\frac{C}{C_0}\right)' = \left(\frac{C}{C_0}\right)_{CNM} - \left(\frac{C}{C_0}\right)_{blank} \quad (3.1)$$

$$m'_{MO}/m_{TiO_2} = \frac{(m_{MO})_{CNM}-(m_{MO})_{blank}}{m_{TiO_2}} \quad (3.2)$$

PVDF-TiO_2 CNMs were then removed from the photoreactor, washed with deionized water, air-dried, and thus reused another two times. The reported catalytic activities in Figure 4.9 represented the average value of three experiments. The photocatalytic activity of the PVDF-TiO_2 CNM (140 °C-3 h-2 M) was performed five times in order to evaluate reusability and stability of CNMs.

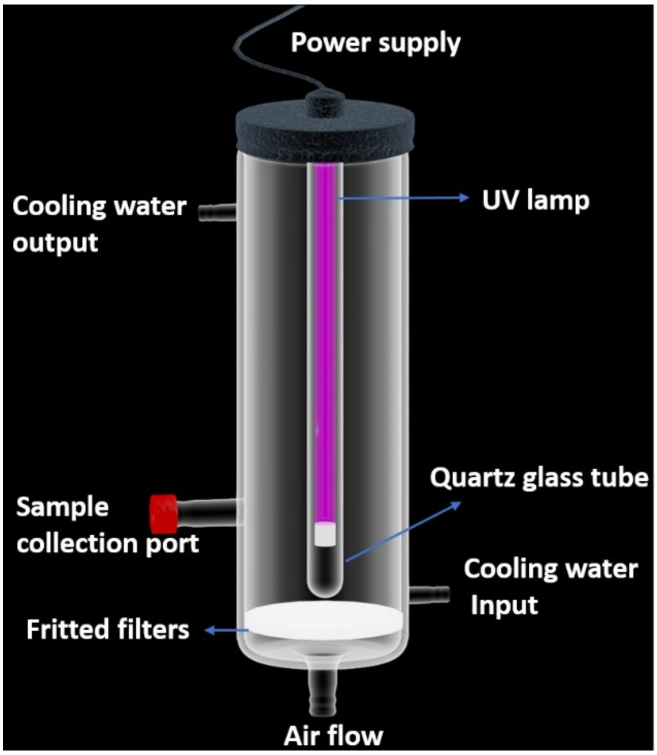

Figure 4.1 The schematic diagram of the photocatalytic reactor.

4.3 Results and discussion

4.3.1 Morphological and structural characterization

SEM images of PVDF-TiO_2 CNMs prepared from precursor solutions with an acidity of 1 M, 2 M, and 3 M are reported in Figure 4.2(A-C), respectively. The membrane shrank when it was hydrothermally disposed in a 1 M solution at 140 ℃ for only 30 min, which may be attributed to the partial melting of PVDF. Therefore, for the hydrothermal reaction in a 1 M solution, we focused on CNMs prepared at 100 ℃ and 120 ℃. Similarly, the membrane obtained in a 3 M solution at 100 ℃ for 3 h did not show the presence of TiO_2 NPs either on the surface of PVDF NFs or in the solution. Then, the membranes prepared at 100 ℃ in a 3 M solution were also disregarded from the subsequent discussion.

For the CNMs obtained using the 1 M acidic solution (Figure 4.2(A)), it can be observed that TiO_2 NPs were assembled in spherical shapes, with a non-uniform coverage on the surface of PVDF NFs, resulting in rough surface morphology. As the treatment time increased, more TiO_2 NPs were produced, then excess TiO_2 NPs accumulated next to the PVDF-TiO_2 NFs. There was no significant difference between samples prepared at 100 °C and 120 °C in the 1 M solution. Regarding the experiments run with 2 M acidic solution (Figure 4.2(B)), only the CNM prepared under the conditions of 100 ℃-0.5 h-2 M had a similar morphology to those prepared from the 1 M solution, and the other CNMs had PVDF-TiO_2 NFs with smooth morphology. Moreover, as the treatment time and heating temperature increased, the diameter of PVDF-TiO_2 NFs increased while maintaining a smooth morphology. Finally, looking at the CNMs prepared in a 3 M acidic solution (Figure 4.2(C)), a non-uniform distribution of TiO_2 NPs was observed in most cases, along with a tendency of TiO_2 NPs to create clusters, especially at 140 °C.

It is clear that the acidity of the precursor solution strongly affected the morphology of the TiO_2 shell layer. Based on the above results, 2 M acidic solution was found to be most suitable for the preparation of PVDF-TiO_2 CNM; accordingly, the diameters of PVDF-TiO_2 NFs prepared from a 2 M acidic solution were measured and are reported in Table 4.2.

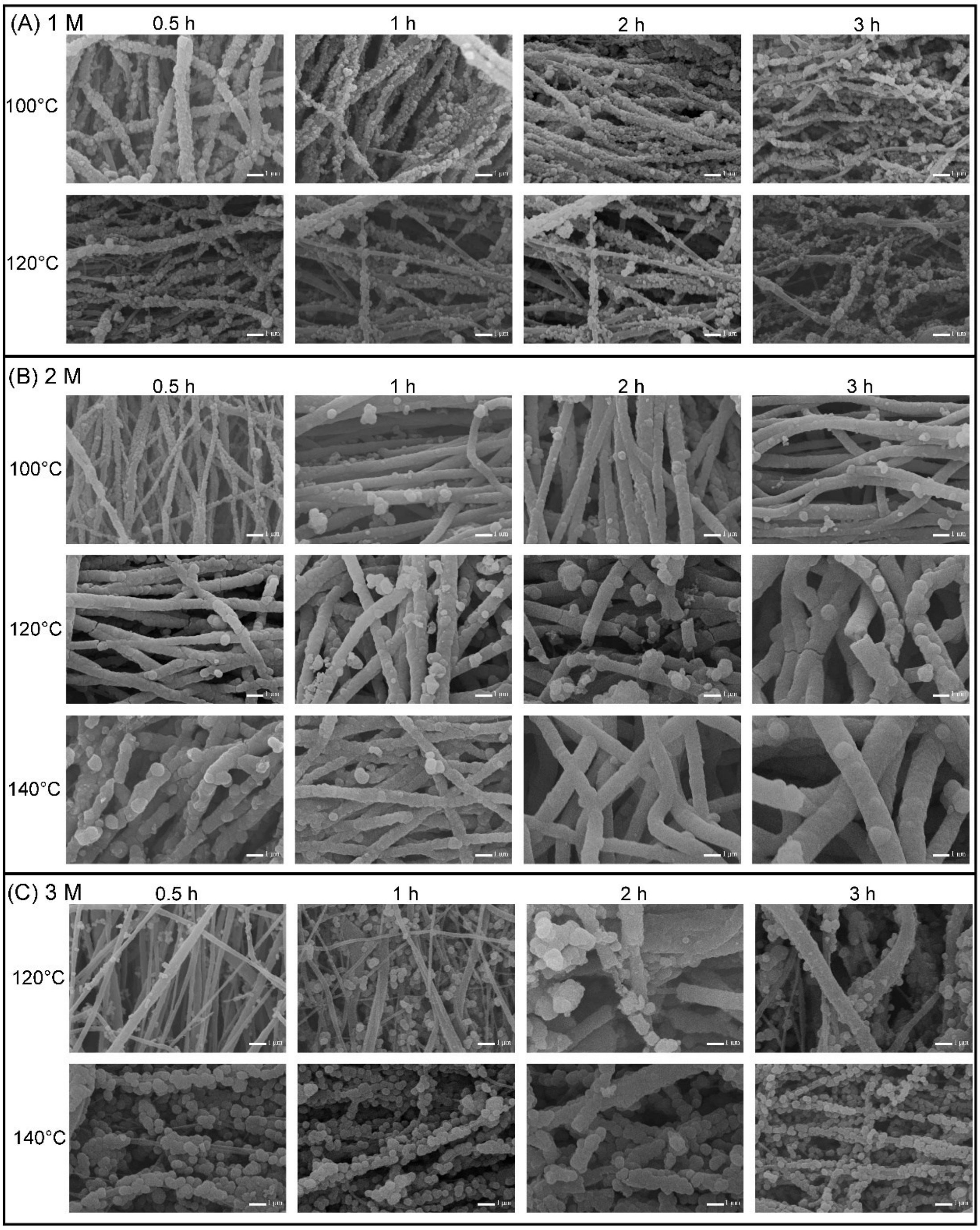

Figure 4.2 SEM images of PVDF-TiO_2 NFs prepared in different H_2SO_4 solutions with an acidity of (A) 1 M, (B) 2 M, and (C) 3 M under different heating temperatures and treatment times (scale bar :1 um).

The aforementioned results related to the morphology were supported by FTIR analysis (Figure 4.3). The main PVDF peaks at 874 cm^{-1}, 1171 cm^{-1}, and 1400 cm^{-1} (related to the CF_2 symmetric stretching[48], CH_2 wagging deformation[48], and the CH_2 wagging vibration[49], respectively), resulted in severely weakened in the sample obtained from 2M precursor solutions, wherein the TiO_2 NPs shell well covered the PVDF NFs core. Moreover, the broad absorption at 3200 cm^{-1} has been attributed to the stretching vibration of the OH bonds, exposed on the titania surface, as well as the absorption at low frequency (800-600 cm^{-1}) has been attributed to the vibration of the O-Ti-O bonds, similar to that in the spectrum of titania.[50-52]

The core-shell PVDF-TiO_2 NFs prepared from a 2 M solution can be considered satisfactory, especially those at 120 °C and 140 °C. Consequently, these PVDF-TiO_2 CNMs from 2 M acidic solution were further characterized in detail.

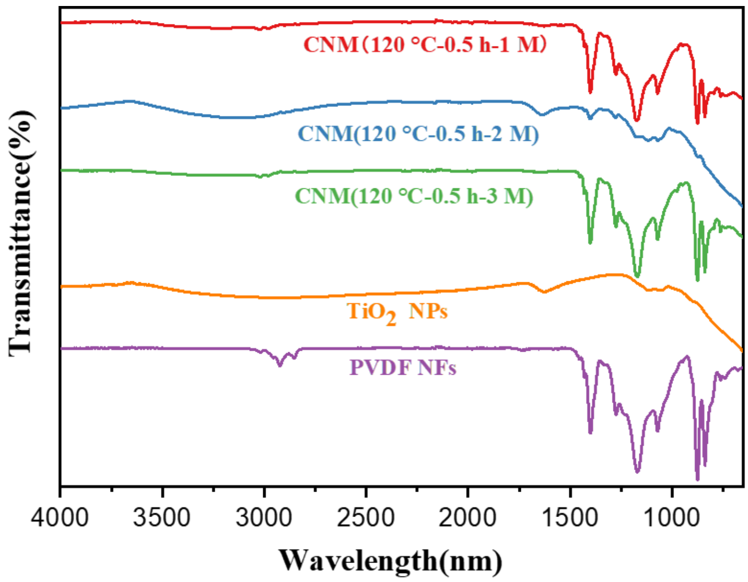

Figure 4.3 FTIR spectra of PVDF NFs membrane, synthesized TiO_2 NPs, and PVDF-TiO_2 CNMs (120 °C-0.5 h)

The wettability of the membranes was determined by water contact angle measurements. Compared to the neat hydrophobic PVDF NFs membrane[53], which showed a contact angle of 150° (Figure 4.4(A)), the contact angle of the obtained PVDF-TiO_2 CNMs at the lowest treatment time (0.5 h) was found to be measurable and in the range of 80°-89° (Figure 4.4(B)), probably due to the non-uniform distribution of the TiO_2 over the whole tested area. Moving towards higher treatment times, independently from the temperature conditions, the membranes resulted completely wettable within 5 seconds, even though the PVDF-TiO_2 CNM prepared under 140 °C-1 h-2 M showed an initial contact angle of 39.2° (Figure 4.4(C).

Table 4.3 summarizes the average water contact angle at five different points on both sides (side A refers to the front side, side B to the back side). The contact angle (the average value of side A and side B) of the samples prepared at 100 °C, 120 °C, and 140 °C for 0.5 h in 2 M solution were approximately 130.3°, 81.8°, and 87.9°, and other samples were completely wetted.

In short, longer treatment time resulted in a thicker TiO_2 layer, meaning that the PVDF-TiO_2 CNM turned from hydrophobic to hydrophilic.[54,55] This feature is beneficial for PVDF-TiO_2 CNM application in wastewater treatment.

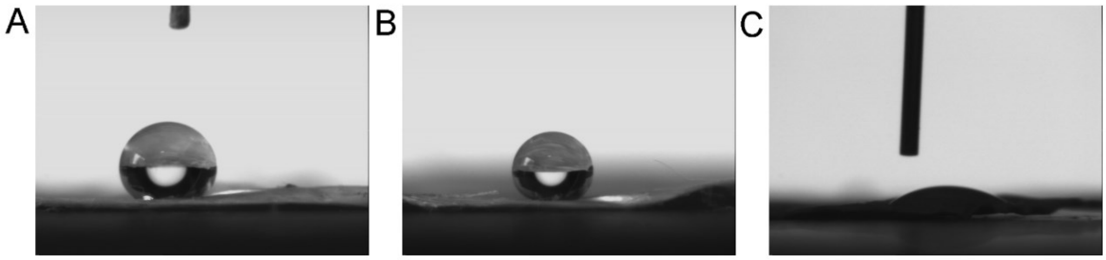

Figure 4.4 Water contact angle on the surface of (A) PVDF mat after 5 s, (B) PVDF-TiO_2 CNM prepared under 100 °C-0.5 h-2 M after 5 s, (C) PVDF-TiO_2 CNM prepared under 140 °C-1 h-2 M at the beginning.

Table 4.3 Water contact angle on PVDF TiO_2 CNMs prepared in 2M solution.

2 M		**0.5 h**	**1 h**	**2 h**	**3 h**
100 °C	Side A	124.5° ± 0.83°	c.w.[1]	c.w.	c.w.
	Side B	136.1° ± 0.44°	c.w.	c.w.	c.w.
120 °C	Side A	82.2° ± 0.60°	c.w.	c.w.	c.w.
	Side B	81.4° ± 0.12°	c.w.	c.w.	c.w.
140 °C	Side A	87.3° ± 0.61°	c.w.	c.w.	c.w.
	Side B	88.5° ± 0.98°	c.w.	c.w.	c.w.

1: completely wettable

The crystal structures of PVDF and PVDF-TiO_2 CNMs were analyzed by XRD, as shown in Figure 4.5 The α phase (020) plane and β phase (110) plane of the neat PVDF were indicated by the strong diffraction peaks at 18.5° and 20.6°. For PVDF-TiO_2 CNMs, the characteristic PVDF diffraction peaks were retained, but with lower intensity. While they were accompanied by several new features: a clear peak at 25.4°corresponded to the (101) plane of anatase TiO_2 (JCPDS card: 21-1272); some weak peaks at 27.5°, 38.0°, 47.8°, 54.6°, and 62.8° corresponded to the (110) plane of rutile TiO_2 (JCPDS card: 21-1276), and the (004), (200), (211), and (204) plane of anatase, respectively. When PVDF-TiO_2 CNM was prepared using either a high heating temperature or a long treatment time, the intensity of the PVDF peaks decreased meantime the intensity of theTiO_2 peaks increased, suggesting that the content of TiO_2 (especially the anatase phase) increased. Crystallite diameters of TiO_2 were determined from diffraction peaks of anatase (101) at 25.4° and rutile (110) at 27.5° using the Scherrer equation, and they were roughly (10 ± 2) nm.

The reference intensity ratio (RIR) value, which is based upon scaling all diffraction data to the diffraction of standard reference materials, can be used in semi-quantitative analysis based on the method proposed by Chung[56] to obtain the percentage of anatase and rutile phases.[57] The content calculated by this method is inaccurate and is only used for relative comparison. Expansion of the spectra between 20°-50°, as shown in Figure 4.6, allows for the diffraction peaks of anatase and rutile phases to be distinguished for calculation of the TiO_2 phase fraction of PVDF-TiO_2 CNMs. The results are listed in Table 4.4.

For the CNMs prepared at 100 °C in 2 M, the fraction of anatase increased when the treatment time increased from 0.5 h to 1 h, with little change upon further extending the treatment time. At 140 °C, a high anatase fraction was observed on the PVDF-TiO_2 CNMs, then an almost total anatase phase was found when the treatment time exceeded 2 h. For the CNM synthesized at 120 °C in 2 M, a complete anatase phase was obtained in most cases. The anatase content of the CNM reacted at 120 °C was higher than those at 100 °C and 140 °C. Therefore, the heating temperature has a more significant influence on the anatase fraction than the treatment time. 120 °C was chosen as the optimal temperature to get the highest content of the anatase phase. A detailed mechanism related to the impact of these parameters (temperature and time) on the TiO_2 crystalline phase would be discussed in the next section.

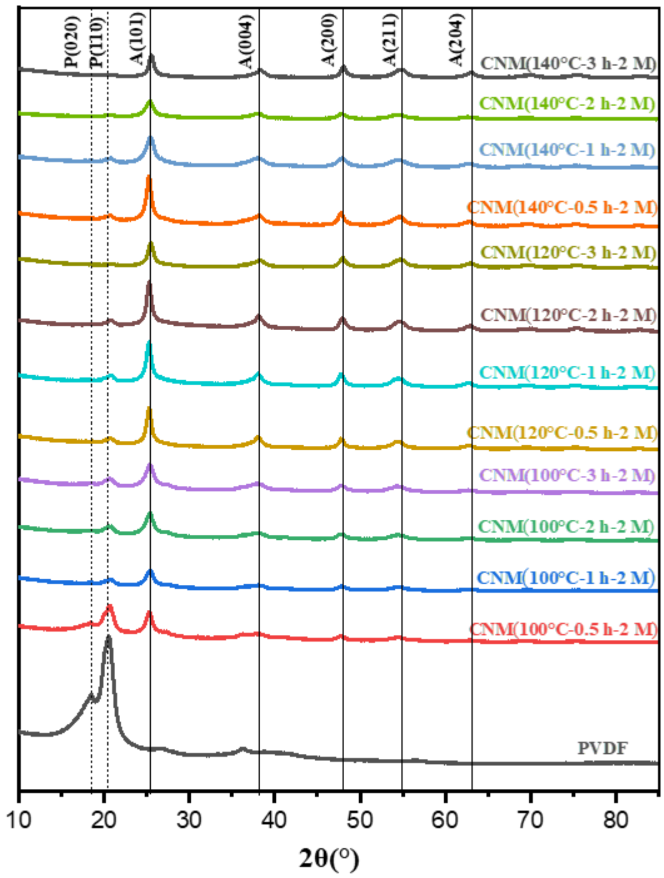

Figure 4.5 XRD patterns of PVDF and PVDF-TiO_2 CNMs prepared under different conditions.

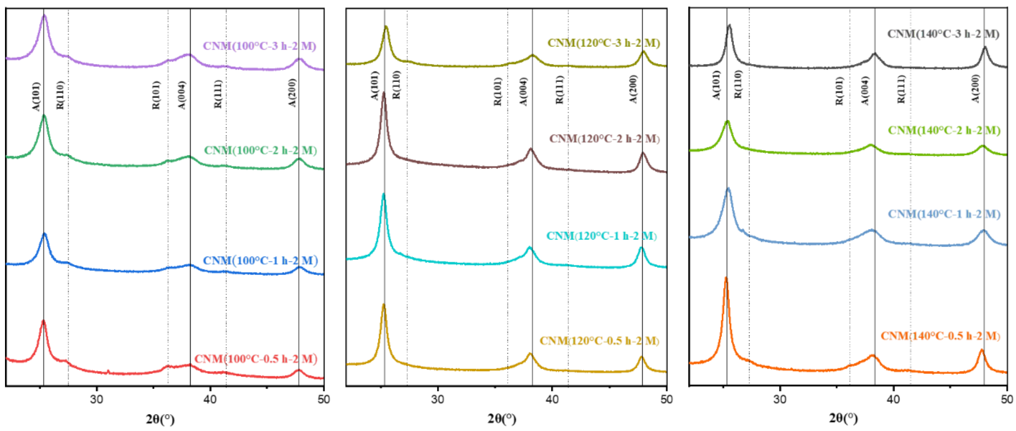

Figure 4.6 The expansion of the spectra in Figure 4.5 between 20-50°.

Table 4.4 The TiO_2 phase content of PVDF-TiO_2 CNMs prepared in 2M solution evaluated from XRD.

2 M		0.5 h	1 h	2 h	3 h
100 °C	$C_{Anatase}$	72.9%	75.6%	84.9%	88.8%
	C_{Rutile}	27.1%	24.4%	15.1%	11.2%
120 °C	$C_{Anatase}$	100%	100%	100%	95.5%
	C_{Rutile}	0	0	0	4.5%
140 °C	$C_{Anatase}$	91.7%	88.8%	100%	100%
	C_{Rutile}	8.3%	11.2%	0	0

TGA was used to analyze the TiO_2 content in the CNMs. Thermograms of pure PVDF, synthesized TiO_2 NPs, and PVDF-TiO_2 CNMs prepared at 120 °C for different treatment times are shown in Figure 4.7. The primary weight loss in the region of 350-550 °C and the slight weight decrease before 350 °C were attributed to the decomposition of PVDF and the impurities in TiO_2, which can be confirmed by the thermogram of pure PVDF and pure TiO_2. The degradation temperature of the CNMs was lower than that of the pure PVDF membrane because the TiO_2 catalyzed the decomposition of PVDF, as reported in the previous work[58]. The residual weight of PVDF-TiO_2 CNMs above 550 °C was related to the inorganic part of the samples (the TiO_2 shell), which increased as treatment time increased. By comparing the residual mass of CNMs and pure TiO_2 at 600 °C, the synthesized TiO_2 NPs synthesized on the membrane can be calculated. These results are listed in Table 4.5, and it can be observed that the mass increased with an increase in heating temperature and treatment time.

Moreover, the BET area of CNM (120 °C-2 h-2 M) was found to be18.7 m^2/g.

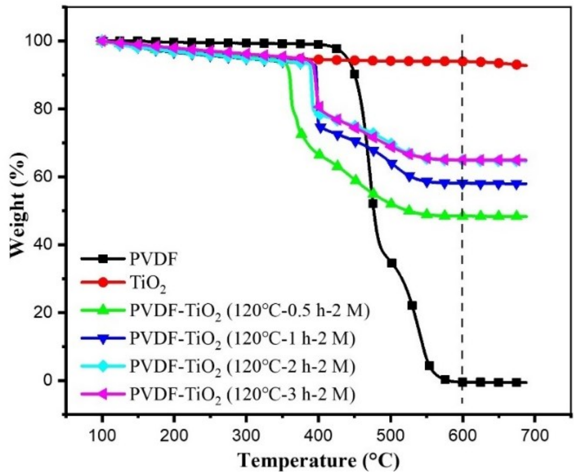

Figure 4.7 The TG curves of PVDF, TiO_2, and CNMs prepared at 120 °C in air atmosphere.

Table 4.5 The TiO_2 NPs content of PVDF-TiO_2 CNMs in 2M solution.

2 M	0.5 h	1 h	2 h	3 h
100 °C	21.2%	53.9%	55.8%	57.2%
120 °C	51.6%	61.9%	69.0%	69.2%
140 °C	64.7%	62.6%	70.2%	77.5%

4.3.2 PVDF-TiO_2 CNMs synthesis mechanism

A schematic illustration of the PVDF-TiO_2 CNM synthesis is present in Figure 4.8. It has been reported that the type of acid might play a critical role in the formation of the polymorphs and that anatase is more likely to be formed when SO_4^{2-} ions are present in the solution.[59,60] The steric effect of SO_4^{2-}, adjacent octahedra were favored to connect the dimers with SO_4^{2-} by sharing the spinal edges to reduce steric repulsion. So, this was the reason why H_2SO_4 was directly adopted as a precursor solution at the beginning.

Two steps are involved in the formation of TiO_2 NPs from metal alkoxide TBOT during hydrothermal reaction: hydrolysis and condensation. TBOT is known to hydrolyze easily to form an amorphous phase $Ti(OH)_4$ in an aqueous solution at room temperature, as well as a large number of octahedral $Ti[(OH)_2(OH_2)_4]^{2+}$ monomers or edge-sharing dimers.[61] As the temperature increases, the solution reaches saturation, and due to the instability of the dissolved species, the different polymeric nuclei form by sharing opposite or spinal edges through olation or oxolation between OH^- and H_2O group.[62] Once these nuclei have grown beyond the critical size, they became stable and then underwent Ostwald ripening in solution or on the surface of the NFs[63].

In precursor solutions with low acidity (1 M), the hydrolysis of TBOT was relatively easy because of a few H^+ ions in the solution.[60] A large amount of TiO_2 nuclei were formed in the solution, meaning that TiO_2 NPs tended to grow in the solution instead of on the PVDF NFs surface. When the acidity of the solution was increased to 2 M, the number of nuclei formed decreased, which in turn reduced the concentration of TiO_2 NPs in the solution. This, together with the repulsive force of SO_4^{2-}, inhibited the aggregation of TiO_2 NPs. Therefore, more TiO_2 NPs grew on the surface of PVDF NFs, and a shell layer with smooth morphology was formed. As the acidity further increased to 3 M, carbonization and esterification of TBOT were observed, which was evidenced by the dark spots formed on the membranes. In addition, more TiO_2 NPs were found in the solution instead of on the PVDF membrane, due to the decrease of H^+ in the solution, which led to an increase in the number of nucleation centers obtained by hydrolysis.

From the viewpoint of energy, the driving force of the hydrothermal crystallization reaction is considered to be the difference in free energy generated by relative supersaturation when the temperature rises from room temperature to hydrothermal temperature.[64] The fraction of the anatase phase can be increased to 100% as the heating temperature increased due to high free energy. However, a further increase in temperature would result in a decrease in anatase fraction and a concomitant increase in the rutile phase (as has been reported previously by Testino et al.)[65]. As explained following, when the crystallite size of the anatase phase exceeds the threshold range (about 1116 nm), the anatase phase is less stable than the rutile phase, then parts of the anatase phase would transform to the rutile phase through lattice rearrangement.[66,67] On the other hand, the formation of TiO_2 NPs can be speculated to follow a dissolution-precipitation mechanism.[64] With the increase in temperature, the solubility of titania in hydrothermal solution decreases, and more nuclei precipitate out and undergo Ostwald ripening[63]; therefore the diameter of PVDF-TiO_2 NFs increases with the heating temperature.

The effect of extending the treatment time is, to some extent, similar to that of increasing the heating temperature. The fraction of the anatase phase increased with the increase of treatment time, which can be explained by high free energy as above-mentioned. The diameter of the formed PVDF-TiO_2 NFs increased when the treatment time was extended from 0.5 h to 3 h, which means that the nuclei can form in half-hour and that the TiO_2 NPs growth can be complete in the subsequent time.

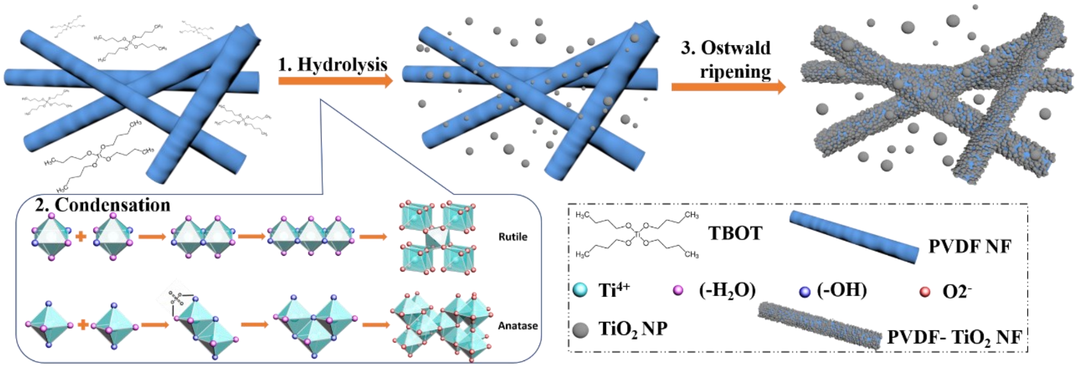

Figure 4.8 Schematic illustration of the PVDF-TiO_2 CNM synthesis.

4.3.3 Optical properties

The optical properties of the prepared PVDF-TiO_2 CNM (120 °C-2 h-2 M) were determined by measuring the response to visible and UV light. The UV-vis absorption spectrum obtained from the DRS results (Figure 4.9(A)) showed strong absorption in the UV region and low absorption in the visible light region, with an absorption edge at about 400 nm, which matches well with the absorption edge of pure TiO_2[68,69].

Another significant feature of the produced CNMs is related to the band-gap energy. The F(R) value is converted from diffuse reflectance value through the Kubelka-Munk function[70]: $F(R) = (1-R)^2/2R$. An indirect allowed transition was adopted for TiO_2[18,71], so the band-gap energy can be determined by extrapolating the linear portion of $(F(R)h\upsilon)^{1/2}$ versus Energy plot to E axis, where hυ was the incident photon energy. Based on this method, the band-gap energy for PVDF-TiO_2 CNM was found to be approximately 3.21 eV (Figure 4.9(B)), which is in good agreement with the band-gap value of anatase TiO_2 (ca.3.2 eV)[71].

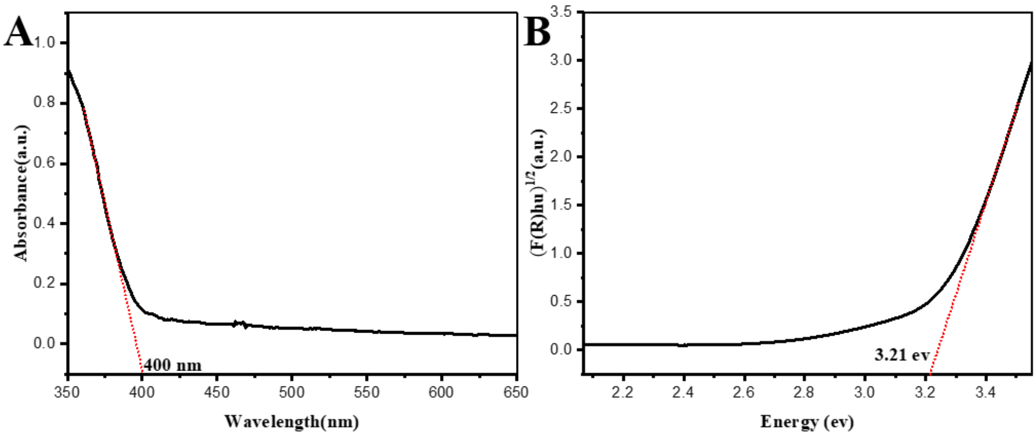

Figure 4.9 (A) UV–vis absorption spectrum and (B) the curve of $(F(R)h\nu)^{1/2}$ versus Energy of PVDF-TiO_2 CNM (120 °C -2 h-2 M).

4.3.4 Photocatalytic performance

As previously mentioned, the photocatalytic performances of the obtained CNMs have been tested for the degradation of MO (2.5 mg/L) in batch mode. A plot of the typical absorbance of MO solutions as a function of wavelength at different sampling times is displayed in Figure 4.10(A). A 95% degradation of the dye has been achieved with the PVDF-TiO_2 CNM (140 °C-3 h-2 M) within the experiment time of 200 mins (Figure 4.10(B)). However, due to the effect of the UV-C light used in this work, in order to evaluate the net performance of the obtained catalytic media a plot of the relative concentration C/C_0’ versus time is reported in Figure 4.10(C). As it can be observed, the photocatalytic effect increased as both the temperature and treatment time increased, reaching a maximum of 30% with the PVDF-TiO_2 CNM (140 °C-3 h-2 M). This result can be explained by looking at the increased amount of TiO_2 which has been shown to raise along with the treatment time and temperature, as confirmed by TGA analysis. According to this, to assess the catalyst efficiency, the relative MO degradation per gram of TiO_2 was investigated as a function of the time in Figure 4.10(D). In this case, CNMs prepared at 140 °C-3 h-2 M no longer exhibited the best MO photodegradation performance, most likely due to photo-shielding effects rendering the inner part of the TiO_2 shell, which is in contact with the PVDF. And for a unit of TiO_2, the best MO photodegradation efficiency was exhibited by the CNM (120 °C-2 h-2 M). It is probably related to better exploitation of the catalyst sites as well as a more adequate TiO_2 thickness layer covering the electrospun fibers.

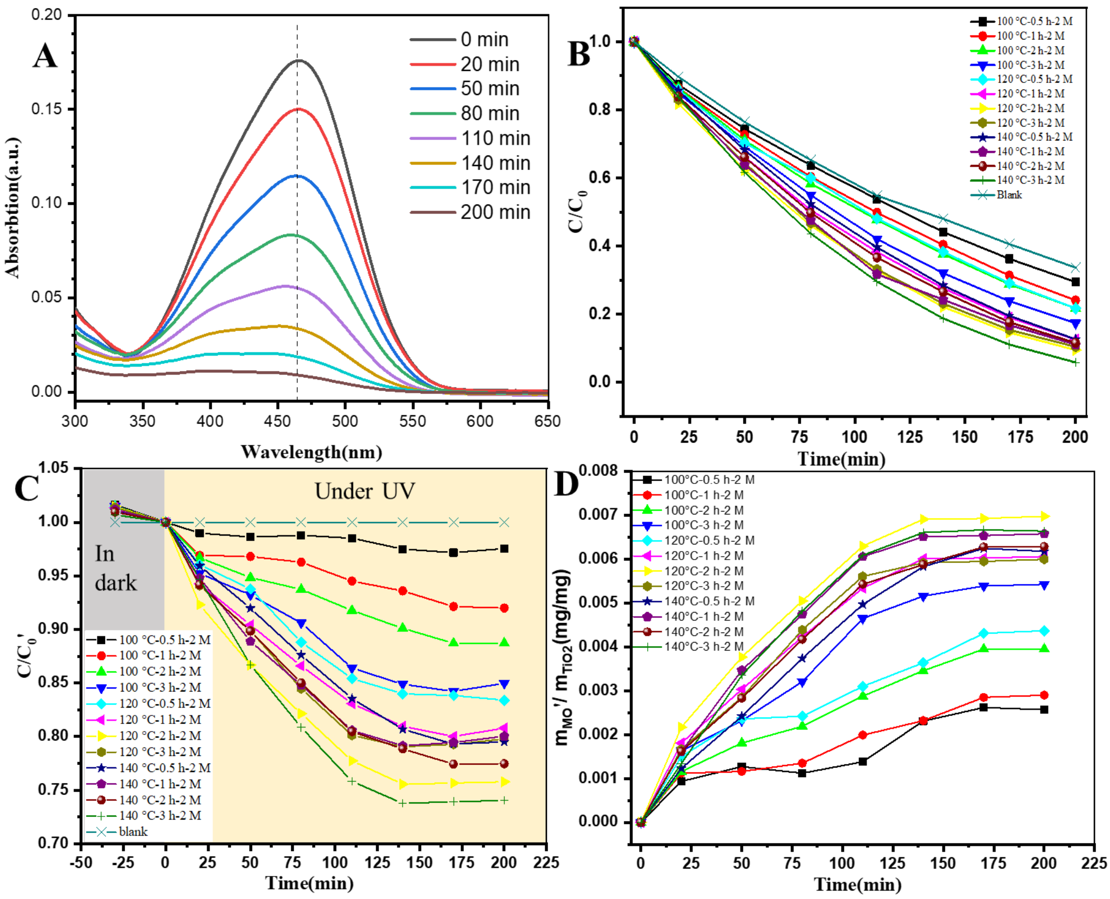

Figure 4.10 (A) Time-dependent UV–vis absorption spectrum of the MO degradation for the PVDF-TiO_2 CNM prepared at 140 °C-3 h-2 M under UV-C, (B) photodegradation profiles of MO for different PVDF-TiO_2 CNMs, (C) the relative concentration C/C_0' as a function of time, (D) the relative MO degradation mass per grams of TiO_2 on each CNM as a function of time. (Performed in triplicate, standard deviation ≤ 5%).

All the membranes showed an effective MO degradation even though it was not complete. With respect to the literature [40,41,73,74], it is difficult to compare the obtained results because the experimental conditions are substantially different, especially the UV light source, which in turn affects the irradiance flux, the catalyst loading, and the tested dye. A potential explanation of the weak photocatalytic efficiency may be related due to the strength of the N=N double bond of MO[72,73] as well as the low catalyst loading (32 mg of CNM) for the pollutant concentration (2.5 mg L^{-1}, 200 mL) used in these experiments.

For practical catalytic applications, an ideal catalyst should be recyclable and reusable. The PVDF-TiO_2 CNM (140 °C-3 h-2 M) was tested for five cycles, with proper washing and drying after each cycle, and the relative concentration C/C_0' is displayed as a function of reaction time shown in Figure 4.11. The photocatalytic efficiency of PVDF-TiO_2 CNM for MO degradation decreased only slightly, which indicates that the membrane has some potential as a reusable catalyst.

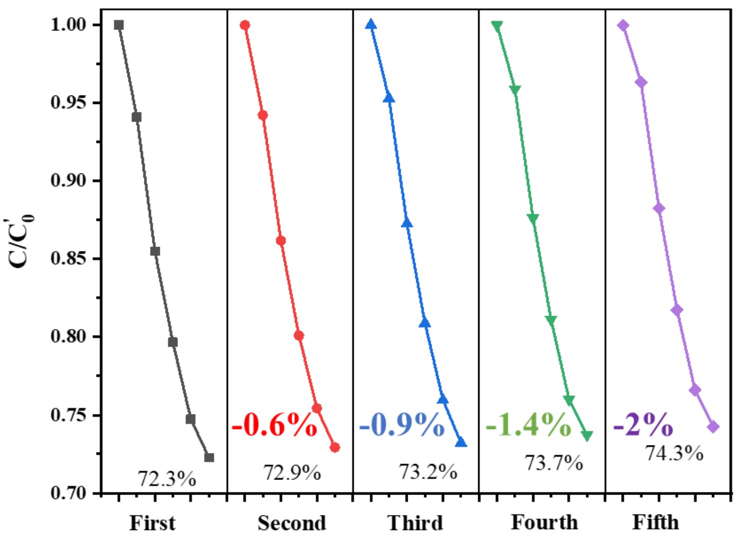

Figure 4.11 The relative concentration C/C_0' of PVDF-TiO_2 CNM (140 °C-3 h-2 M) as a function of regular interval for five cycles of the MO degradation. (The number presented the catalyst deactivation of each cycle compared to the first cycle)

4.3.5 Structural stability of CNM

SEM images of PVDF-TiO_2 CNM (120 °C-2 h-2 M)) before and after photocatalytic experiments (Figure 4.12(A-B) and (C-D)) revealed that the PVDF-TiO_2 CNMs maintained their core-shell structure with a visible smooth TiO_2 outer layer on the PVDF NFs. This result was confirmed further by FTIR analysis, which returned the same spectrum as that taken before experimentation, without the presence of the PVDF characteristic peaks.

In general, these post-reaction analyses (SEM and FTIR) could demonstrate that the stability of the PVDF-TiO_2 CNMs and no leaching effect during the application, due to the close connection between the TiO_2 shell layer and the PVDF core achieved by the hydrothermal preparation method.

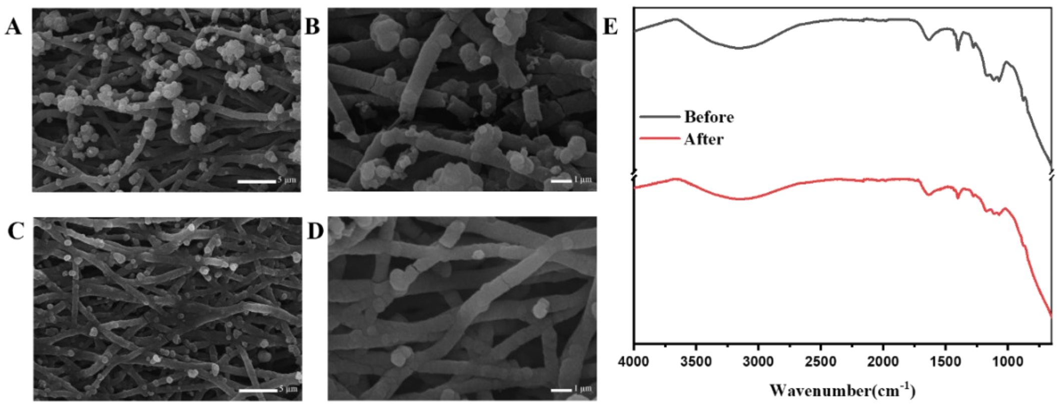

Figure 4.12 SEM images of PVDF-TiO_2 CNM (120 °C-2 h-2 M) (A, B) before and (C, D) after photocatalysis (scale bar :1 um), (E) the FTIR spectra of PVDF-TiO_2 CNM (120 °C-2 h-2 M) before and after photocatalysis.

4.4 Conclusion

In this work, we have used microwave-assisted hydrothermal treatment of electrospun PVDF NFs, a rapid and easy method, to prepare PVDF-TiO_2 CNMs with catalytic photo-oxidation activity. Compared to previous reports[74], our strategy for producing PVDF-TiO_2 CNMs has several advantages, such as a higher exposure of TiO_2 NPs on the PVDF NFs, a shorter treatment time, and a higher production efficiency.

A detailed study on the process parameters effect was undertaken. The optimal precursor solution acidity to achieve a smooth TiO_2 outer layer with uniform coverage of the PVDF electrospun core was found to be 2M. The highest TiO_2 anatase fraction was obtained at 120 °C, and the treatment time has been proved to strongly affect the anatase crystal size till the critical one, beyond which the rutile phase was favored. In addition, the PVDF-TiO_2 CNM exhibited good photocatalytic performance for the MO degradation, attributed to the complete anatase phase of TiO_2 and the high contact surface between TiO_2 and MO solution.

In summary, the stability and recyclability of PVDF-TiO_2 CNMs make these media a potential candidate for many different applications, such as organic pollution treatment in the liquid phase, or biological sensor production. In subsequent studies, the photocatalytic performance of PVDF-TiO_2 CNMs will be further investigated, and more thorough catalytic experiments will be carried out to optimize the catalyst-pollutant ratio and improve the catalyst efficiency.

References

(1) Kabra, K.; Chaudhary, R.; Sawhney, R. L. Treatment of hazardous organic and inorganic compounds through aqueous-phase photocatalysis: A review. *Ind Eng Chem Res* **2004**, *43*, 7683-7696.

(2) Rueda-Marquez, J. J.; Levchuk, I.; Fernández Ibañez, P.; Sillanpää, M. A critical review on application of photocatalysis for toxicity reduction of real wastewaters. *Journal of Cleaner Production* **2020**, *258*, 120694.

(3) Wenderich, K.; Mul, G. Methods, Mechanism, and Applications of Photodeposition in Photocatalysis: A Review. *Chem Rev* **2016**, *116*, 14587-14619.

(4) Byrne, C.; Subramanian, G.; Pillai, S. C. Recent advances in photocatalysis for environmental applications. *Journal of Environmental Chemical Engineering* **2018**, *6*, 3531-3555.

(5) Liu, J.; Wang, Y.; Ma, J.; Peng, Y.; Wang, A. A review on bidirectional analogies between the photocatalysis and antibacterial properties of ZnO. *Journal of Alloys and Compounds* **2019**, *783*, 898-918.

(6) Dal Santo, V.; Naldoni, A. Titanium Dioxide Photocatalysis. *Catalysts* **2018**, *8*.

(7) Henderson, M. A. A surface science perspective on TiO_2 photocatalysis. *Surface Science Reports* **2011**, *66*, 185-297.

(8) Hitam, C.; Jalil, A. A review on exploration of Fe_2O_3 photocatalyst towards degradation of dyes and organic contaminants. *Journal of environmental management* **2020**, *258*, 110050.

(9) Mishra, M.; Chun, D.-M. α-Fe2O3 as a photocatalytic material: A review. *Applied Catalysis A: General* **2015**, *498*, 126-141.

(10) Zhao, H.; Tian, F.; Wang, R.; Chen, R. A review on bismuth-related nanomaterials for photocatalysis. *Reviews in Advanced Sciences and Engineering* **2014**, *3*, 3-27.

(11) Konstantinou, I. K.; Albanis, T. A. TiO_2-assisted photocatalytic degradation of azo dyes in aqueous solution: kinetic and mechanistic investigations: A review. *Applied Catalysis B: Environmental* **2004**, *49*, 1-14.

(12) Chong, M. N.; Jin, B.; Chow, C. W. K.; Saint, C. Recent developments in photocatalytic water treatment technology: A review. *Water Res* **2010**, *44*, 2997-3027.

(13) Carp, O.; Huisman, C. L.; Reller, A. Photoinduced reactivity of titanium dioxide. *Prog Solid State Ch* **2004**, *32*, 33-177.

(14) Buso, D.; Post, M.; Cantalini, C.; Mulvaney, P.; Martucci, A. Gold nanoparticle-doped TiO_2 semiconductor thin films: gas sensing properties. *Advanced Functional Materials* **2008**, *18*, 3843-3849.

(15) Zhu, T.; Gao, S. P. The Stability, Electronic Structure, and Optical Property of TiO_2 Polymorphs. *J Phys Chem C* **2014**, *118*, 11385-11396.

(16) Ovenstone, J.; Yanagisawa, K. Effect of Hydrothermal Treatment of Amorphous Titania on the Phase Change from Anatase to Rutile during Calcination. *Chemistry of Materials* **1999**, *11*, 2770-2774.

(17) Riegel, G.; Bolton, J. R. Photocatalytic Efficiency Variability in TiO_2 Particles. *The Journal of Physical Chemistry* **1995**, *99*, 4215-4224.

(18) Zhang, J.; Zhou, P.; Liu, J.; Yu, J. New understanding of the difference of photocatalytic activity among anatase, rutile and brookite TiO_2. *Physical Chemistry Chemical Physics* **2014**, *16*, 20382-20386.

(19) Kumar, A.; Kuang, Y.; Liang, Z.; Sun, X. Microwave chemistry, recent advancements and eco-friendly microwave-assisted synthesis of nanoarchitectures and their applications: A review. *Materials Today Nano* **2020**, 100076.

(20) Meng, L.-Y.; Wang, B.; Ma, M.-G.; Lin, K.-L. The progress of microwave-assisted hydrothermal method in the synthesis of functional nanomaterials. *Materials Today Chemistry* **2016**, *1-2*, 63-83.

(21) Rathi, A. K.; Gawande, M. B.; Zboril, R.; Varma, R. S. Microwave-assisted synthesis–catalytic applications in aqueous media. *Coordination Chemistry Reviews* **2015**, *291*, 68-94.

(22) Wilson, G. J.; Matijasevich, A. S.; Mitchell, D. R. G.; Schulz, J. C.; Will, G. D. Modification of TiO_2 for enhanced surface properties: Finite Ostwald ripening by a microwave hydrothermal process. *Langmuir* **2006**, *22*, 2016-2027.

(23) Komarneni, S.; Roy, R.; Li, Q. Microwave-hydrothermal synthesis of ceramic powders. *Materials Research Bulletin* **1992**, *27*, 1393-1405.

(24) Yang, Y.; Wang, G. Z.; Deng, Q.; Ng, D. H. L.; Zhao, H. J. Microwave-Assisted Fabrication of Nanoparticulate TiO_2 Microspheres for Synergistic Photocatalytic Removal of Cr(VI) and Methyl Orange. *Acs Appl Mater Inter* **2014**, *6*, 3008-3015.

(25) Zhang, M.; Wang, W.; Wu, C.; Wang, P.; Ru, H. Rapid fabrication of TiO_2 nanobelts with controllable crystalline structure by microwave-assisted hydrothermal method and their photocatalytic activity. *Ceramics International* **2019**, *45*, 22558-22563.

(26) Cho, S. H.; Nguyen, H. H.; Gyawali, G.; Son, J. E.; Sekino, T.; Joshi, B.; Kim, S. H.; Jo, Y. H.; Kim, T. H.; Lee, S. W. Effect of microwave-assisted hydrothermal process parameters on formation of different TiO_2 nanostructures. *Catal Today* **2016**, *266*, 46-52.

(27) Chen, P.; Peng, J. D.; Liao, C. H.; Shen, P. S.; Kuo, P. L. Microwave-assisted hydrothermal synthesis of TiO_2 spheres with efficient photovoltaic performance for dye-sensitized solar cells. *J Nanopart Res* **2013**, *15*.

(28) Bregadiolli, B. A.; Fernandes, S. L.; Graeff, C. F. d. O. Easy and fast preparation of TiO_2-based nanostructures using microwave assisted hydrothermal synthesis. *Materials Research* **2017**, *20*, 912-919.

(29) Li, Y.; Zhu, J.; Cheng, H.; Li, G.; Cho, H.; Jiang, M.; Gao, Q.; Zhang, X. Developments of Advanced Electrospinning Techniques: A Critical Review. *Advanced Materials Technologies* **2021**, 2100410.

(30) Collier, A.; Wang, H.; Yuan, X. Z.; Zhang, J.; Wilkinson, D. P. Degradation of polymer electrolyte membranes. *International Journal of Hydrogen Energy* **2006**, *31*, 1838-1854.

(31) Nguyen, T. Degradation of poly [vinyl fluoride] and poly [vinylidene fluoride]. *Polymer Reviews* **1985**, *25*, 227-275.

(32) Kise, H.; Ogata, H. Phase transfer catalysis in dehydrofluorination of poly (vinylidene fluoride) by aqueous sodium hydroxide solutions. *Journal of Polymer Science: Polymer Chemistry Edition* **1983**, *21*, 3443-3451.

(33) Lin, Y.; Zhang, Y.; Zhan, S.; Sun, C.; Hu, G.; Yang, H.; Yuan, Q. Synergistically ultrahigh energy storage density and efficiency in designed sandwich-structured poly(vinylidene fluoride)-based flexible composite films induced by doping $Na_{0.5}Bi_{0.5}TiO_3$ whiskers. *Journal of Materials Chemistry A* **2020**, *8*, 23427-23435.

(34) Zhang, Y.; Yang, H.; Dang, Z.; Zhan, S.; Sun, C.; Hu, G.; Lin, Y.; Yuan, Q. Multilayer Structured Poly(vinylidene fluoride)-Based Composite Film with Ultrahigh Breakdown Strength and Discharged Energy Density. *Acs Appl Mater Inter* **2020**, *12*, 22137-22145.

(35) Lovinger, A.; Reed, D. Inhomogeneous thermal degradation of poly (vinylidene fluoride) crystallized from the melt. *Macromolecules* **1980**, *13*, 989-994.

(36) Furusho, N.; Komatsu, T.; Nakagawa, T. A Study of the Thermal Degradation of Several Halogen-containing Polymers by Torsional Braid Analysis. *Bulletin of the Chemical Society of Japan* **1974**, *47*, 1573-1577.

(37) Liu, F.; Hashim, N. A.; Liu, Y. T.; Abed, M. R. M.; Li, K. Progress in the production and modification of PVDF membranes. *J Membrane Sci* **2011**, *375*, 1-27.

(38) Alaoui, O. T.; Nguyen, Q. T.; Schaetzel, P.; Mbareck, C. Dye and bacteria photodegradations with anatase-loaded microporous poly (vinylidene fluoride) membranes. *Catalysis Science & Technology* **2011**, *1*, 1412-1422.

(39) Dai, B.; Huang, H.; Wang, W.; Chen, Y.; Lu, C.; Kou, J.; Wang, L.; Wang, F.; Xu, Z. Greatly enhanced photocatalytic activity by organic flexible piezoelectric PVDF induced spatial electric field. *Catalysis Science & Technology* **2017**, *7*, 5594-5601.

(40) Dong, P.; Huang, Z.; Nie, X.; Cheng, X.; Jin, Z.; Zhang, X. Plasma enhanced decoration of nc-TiO_2 on electrospun PVDF fibers for photocatalytic application. *Materials Research Bulletin* **2019**, *111*, 102-112.

(41) Lee, C. G.; Javed, H.; Zhang, D.; Kim, J. H.; Westerhoff, P.; Li, Q.; Alvarez, P. J. J. Porous Electrospun Fibers Embedding TiO_2 for Adsorption and Photocatalytic Degradation of Water Pollutants. *Environmental science & technology* **2018**, *52*, 4285-4293.

(42) Zhang, Z.-G.; Liu, H.; Wang, X.-X.; Zhang, J.; Zhang, F.-B.; Li, R.; Yu, M.; Ramakrishna, S.; Long, Y.-Z. Influences of acids on morphology and properties of TiO_2

grown on electrospun PVDF fibers. *Journal of Physics and Chemistry of Solids* **2019**, *133*, 117-127.

(43) Roso, M.; Boaretti, C.; Bonora, R.; Modesti, M.; Lorenzetti, A. Nanostructured Active Media for Volatile Organic Compounds Abatement: The Synergy of Graphene Oxide and Semiconductor Coupling. *Ind Eng Chem Res* **2018**, *57*, 16635-16644.

(44) Durairaj, A.; Ramasundaram, S.; Sakthivel, T.; Ramanathan, S.; Rahaman, A.; Kim, B.; Vasanthkumar, S. Air bubbles induced piezophotocatalytic degradation of organic pollutants using nanofibrous poly(vinylidene fluoride)-titanium dioxide hybrid. *Applied Surface Science* **2019**, *493*, 1268-1277.

(45) Tan, J. Z.; Nursam, N. M.; Xia, F.; Truong, Y. B.; Kyratzis, I. L.; Wang, X.; Caruso, R. A. Electrospun PVDF-TiO_2 with tuneable TiO_2 crystal phases: synthesis and application in photocatalytic redox reactions. *Journal of Materials Chemistry A* **2017**, *5*, 641-648.

(46) Zhang, P.; Zhao, X.; Zhang, X.; Lai, Y.; Wang, X.; Li, J.; Wei, G.; Su, Z. Electrospun doping of carbon nanotubes and platinum nanoparticles into the β-phase polyvinylidene difluoride nanofibrous membrane for biosensor and catalysis applications. *Acs Appl Mater Inter* **2014**, *6*, 7563-7571.

(47) Modesti, M.; Roso, M.; Boaretti, C.; Besco, S.; Hrelja, D.; Sgarbossa, P.; Lorenzetti, A. Preparation of smart nano-engineered electrospun membranes for methanol gas-phase photoxidation. *Applied Catalysis B: Environmental* **2014**, *144*, 216-222.

(48) Elashmawi, I.; Hakeem, N. Effect of PMMA addition on characterization and morphology of PVDF. *Polymer Engineering & Science* **2008**, *48*, 895-901.

(49) Arshad, A.; Wahid, M.; Rusop, M.; Majid, W.; Subban, R.; Rozana, M. Dielectric and structural properties of poly (vinylidene fluoride)(PVDF) and poly (vinylidene fluoride-trifluoroethylene)(PVDF-TrFE) filled with magnesium oxide nanofillers. *Journal of Nanomaterials* **2019**, *2019*.

(50) Liu, Z.; Jian, Z.; Fang, J.; Xu, X.; Zhu, X.; Wu, S. Low-temperature reverse microemulsion synthesis, characterization, and photocatalytic performance of nanocrystalline titanium dioxide. *International Journal of Photoenergy* **2012**, *2012*.

(51) Lv, K.; Zuo, H.; Sun, J.; Deng, K.; Liu, S.; Li, X.; Wang, D. (Bi, C and N) codoped TiO_2 nanoparticles. *Journal of hazardous materials* **2009**, *161*, 396-401.

(52) Fang, J.; Wang, F.; Qian, K.; Bao, H.; Jiang, Z.; Huang, W. Bifunctional N-doped mesoporous TiO_2 photocatalysts. *The Journal of Physical Chemistry C* **2008**, *112*, 18150-18156.

(53) Prince, J. A.; Singh, G.; Rana, D.; Matsuura, T.; Anbharasi, V.; Shanmugasundaram, T. S. Preparation and characterization of highly hydrophobic poly(vinylidene fluoride) – Clay nanocomposite nanofiber membranes (PVDF–clay NNMs) for desalination using direct contact membrane distillation. *J Membrane Sci* **2012**, *397-398*, 80-86.

(54) Razmjou, A.; Arifin, E.; Dong, G.; Mansouri, J.; Chen, V. Superhydrophobic modification of TiO_2 nanocomposite PVDF membranes for applications in membrane distillation. *J Membrane Sci* **2012**, *415-416*, 850-863.

(55) Kang, Y.; Jiao, S.; Wang, B.; Lv, X.; Wang, W.; Yin, W.; Zhang, Z.; Zhang, Q.; Tan, Y.; Pang, G. PVDF-Modified TiO_2 Nanowires Membrane with Underliquid Dual Superlyophobic Property for Switchable Separation of Oil–Water Emulsions. *Acs Appl Mater Inter* **2020**, *12*, 40925-40936.

(56) Chung, F. H. Quantitative interpretation of X-ray diffraction patterns of mixtures. I. Matrix-flushing method for quantitative multicomponent analysis. *Journal of Applied Crystallography* **1974**, *8*.

(57) Hubbard, C. R.; Snyder, R. L. RIR-measurement and use in quantitative XRD. *Powder Diffraction* **1988**, *3*, 74-77.

(58) Mohamadi, S. Preparation and characterization of PVDF/PMMA/graphene polymer blend nanocomposites by using ATR-FTIR technique. *Infrared Spectroscopy-Materials Science, Engineering and Technology* **2012**, *1*.

(59) Tian, B. Z.; Chen, F.; Zhang, J. L.; Anpo, M. Influences of acids and salts on the crystalline phase and morphology of TiO_2 prepared under ultrasound irradiation. *J Colloid Interf Sci* **2006**, *303*, 142-148.

(60) Zhang, Z. G.; Liu, H.; Wang, X. X.; Zhang, J.; Zhang, F. B.; Li, R.; Yu, M.; Ramakrishna, S.; Long, Y. Z. Influences of acids on morphology and properties of TiO_2 grown on electrospun PVDF fibers. *Journal of Physics and Chemistry of Solids* **2019**, *133*, 117-127.

(61) Zhao, B.; Lin, L.; He, D. Phase and morphological transitions of titania/titanate nanostructures from an acid to an alkali hydrothermal environment. *Journal of Materials Chemistry A* **2013**, *1*, 1659-1668.

(62) Zhang, J.; Sun, P.; Jiang, P.; Guo, Z.; Liu, W.; Lu, Q.; Cao, W. The formation mechanism of TiO_2 polymorphs under hydrothermal conditions based on the structural evolution of $[Ti(OH)_h(H_2O)_{6-h}]^{4-h}$ monomers. *Journal of Materials Chemistry C* **2019**, *7*, 5764-5771.

(63) Cushing, B. L.; Kolesnichenko, V. L.; O'connor, C. J. Recent advances in the liquid-phase syntheses of inorganic nanoparticles. *Chem Rev* **2004**, *104*, 3893-3946.

(64) Zheng, Y. Q.; Shi, E. R.; Chen, Z. Z.; Li, W. J.; Hu, X. F. Influence of solution concentration on the hydrothermal preparation of titania crystallites. *J Mater Chem* **2001**, *11*, 1547-1551.

(65) Testino, A.; Bellobono, I. R.; Buscaglia, V.; Canevali, C.; D'Arienzo, M.; Polizzi, S.; Scotti, R.; Morazzoni, F. Optimizing the photocatalytic properties of hydrothermal TiO_2 by the control of phase composition and particle morphology. A systematic approach. *J Am Chem Soc* **2007**, *129*, 3564-3575.

(66) Banfield, J. Thermodynamic analysis of phase stability of nanocrystalline titania. *J Mater Chem* **1998**, *8*, 2073-2076.

(67) Zhang, H.; Banfield, J. F. Understanding polymorphic phase transformation behavior during growth of nanocrystalline aggregates: insights from TiO_2. *The Journal of Physical Chemistry B* **2000**, *104*, 3481-3487.

(68) Choi, J.; Park, H.; Hoffmann, M. R. Effects of single metal-ion doping on the visible-light photoreactivity of TiO_2. *The Journal of Physical Chemistry C* **2010**, *114*, 783-792.

(69) Dharma, J.; Pisal, A.; Shelton, C. Simple method of measuring the band gap energy value of TiO_2 in the powder form using a UV/Vis/NIR spectrometer. *Application Note Shelton, CT: PerkinElmer* **2009**.

(70) Schevciw, O.; White, W. B. The optical absorption edge of rare earth sesquisulfides and alkaline earth-rare earth sulfides. *Materials research bulletin* **1983**, *18*, 1059-1068.

(71) López, R.; Gómez, R. Band-gap energy estimation from diffuse reflectance measurements on sol–gel and commercial TiO_2: a comparative study. *Journal of sol-gel science and technology* **2012**, *61*, 1-7.

(72) Xu, S. W.; Qian, W. Q.; Zhang, D.; Zhao, X.; Zhang, X. M.; Li, C. B.; Bowen, C. R.; Yang, Y. A coupled photo-piezo-catalytic effect in a BST-PDMS porous foam for enhanced dye wastewater degradation. *Nano Energy* **2020**, *77*.

(73) Zhao, T.; Zai, J.; Xu, M.; Zou, Q.; Su, Y.; Wang, K.; Qian, X. Hierarchical $Bi_2O_2CO_3$ microspheres with improved visible-light-driven photocatalytic activity. *CrystEngComm* **2011**, *13*, 4010-4017.

(74) Al-Mamun, M. R.; Kader, S.; Islam, M. S.; Khan, M. Z. H. Photocatalytic activity improvement and application of UV-TiO_2 photocatalysis in textile wastewater treatment: A review. *Journal of Environmental Chemical Engineering* **2019**, *7*, 103248.

Chapter V Preparation of PVDF/TiO_2 core/shell nanofibrous membrane via coaxial electrospinning

Abstract

Here, coaxial electrospinning was applied to obtain a polyvinylidene fluoride (PVDF)/titanium dioxide (TiO_2) core/shell composite nanofibrous membrane (CNM) with a large surface area and abundant reactive sites. Commercial TiO_2 (80% anatase and 20% rutile), P25, was directly applied for the preparation of PVDF/TiO_2 CNM to utilize excellent photocatalytic efficiency of P25 and avoid thermal damage to PVDF. The core/shell structure endowed the CNM with high photocatalytic efficiency due to the exposure of TiO_2 NPs. It is the first time that the PVDF/TiO_2 core/shell CNM was prepared by coaxial electrospinning.

Keywords: coaxial electrospinning, core-shell composite nanofibrous membrane, photocatalysis, wastewater treatment.

5.1 Introduction

With the rapid development of industrialization and the widespread use of chemical and biological synthetic materials, water pollution has become an urgent problem in the world. Various practical solutions have been applied to yield high-quality water resources, among which photocatalysis as an advanced oxidation technology is regarded as a promising environmental-friendly solution.

Titanium dioxide (TiO_2) has been extensively investigated as a photocatalyst due to its superior photocatalytic properties and economical friendliness.[1] However, the practical applications of TiO_2, like most photocatalysts, are hampered by the low photocatalytic efficiency, which is mainly attributed to the low concentration of photo-generated charge carriers and the high recombination rate of electron-hole pair. In addition, powdered TiO_2 is difficult to recover after use, especially in liquid systems, resulting in limited use value and secondary pollution.

P25 consisting of 80% anatase and 20% rutile, is a commercial TiO_2 NP that is widely used as a photocatalyst. P25 has relatively high efficiency in many photocatalytic reaction systems because the coexistence of anatase and rutile crystallites can accelerate the transfer of photogenerated electrons and holes as well as reduce the recombination rate of electron-hole pairs.[2] Hence, P25 was directly used as TiO_2 NP to achieve excellent photocatalytic efficiency.

Coaxial electrospinning, a novel version of electrospinning, enables the production of nanofibers with diverse morphologies (such as core-shell, hollow, and porous) and applications (like drug release, encapsulation, and cell scaffold).[3-5] Concentric cylindrical nozzles with inner and outer nozzles connect to their relative feed source (generally two syringes, at least one with a polymer solution) for coaxial electrospinning. The preparation of core-shell nanofibers by coaxial electrospinning has the following advantages: a simple one-step and highly efficient process; a variety of material combinations; controllable sheath thickness. Besides the formation of complex polymer fibers using two polymer solutions[3,6] embedding nonpolymeric materials (like ceramic, protein, and drug) without filamentation properties in polymer fibers has also been widely studied[7-9], while the opposite arrangement, coating polymer fibers with nonpolymeric materials, has received less attention.

In this work, PVDF/TiO_2 core/shell composite nanofiber membranes (CNMs) were prepared by coaxial electrospinning with PVDF solution and TiO_2 NPs suspension as the core and shell feed sources, respectively. Many advantages were expected to bring to the photocatalyst via this preparation: (1) Large surface area from the polymer nanofiber membrane; (2) TiO_2 NPs were mainly distributed outside PVDF NFs, so they can directly contact with the pollutant and be easily photoactivated, because of the core-shell structure; (3) Simple preparation without any post-treatment owing to coaxial electrospinning and the connection between PVDF and TiO_2.

The solvent of the outer suspension, the ratio of the core and shell feed rates, and the concentration of TiO_2 in shell suspension were investigated to prepare the PVDF/TiO_2 CNM with a good core/shell structure. Then phenol degradation was used to evaluate the photocatalytic behavior of the PVDF/TiO_2 CNM. To the best of our knowledge, it is the first time that the PVDF/TiO_2 core/shell CNMs were prepared by coaxial electrospinning.

5.2 Experimental section

5.2.1 Materials

PVDF (KYNAR 500) was purchased from Arkema. Titanium dioxide (TiO_2), acetone (ACE), dimethyl sulfoxide (DMSO), tetrahydrofuran (THF), phenol, and ethanol were purchased from Sigma Aldrich. All reagents were used as received without any further treatment. Deionized water was used throughout the whole experiment.

5.2.2 Preparation of PVDF/TiO_2 CNM

1 g of PVDF powder was added to 6 g solvent mixture of DMSO and ACE with a weight ratio of 2:1 and stirred overnight at room temperature to prepare a 15 wt% PVDF solution. TiO_2 was dispersed in 4 g solvent (DMSO, ACE, or THF) to reach the desired concentration (one study variable), and the suspension was sonicated for 1 h before use.

Two 5 mL syringes filled with the PVDF solution and TiO_2 suspension were placed on two syringe pumps, the feed rates of syringe pumps were one study variable. A spinneret consists of two nozzles that were concentrically aligned, and the inner and outer nozzles were connected to syringes of PVDF solution and TiO_2 suspension. A grounded stainless roller covered with aluminum foil was used as the collector and its rotation rate was set at 4000 rpm. The voltage applied to the spinneret and the distance between the spinneret and collector were 12 kV and 15 cm. A schematic diagram of the coaxial electrospinning is shown in Figure 5.1.

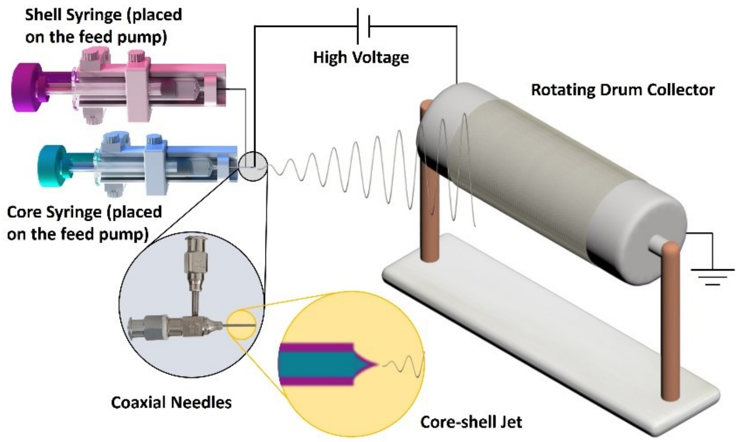

Figure 5.1 The schematic diagram of the coaxial electrospinning.

The electrospinning process was carried out in an atmospheric environment with a temperature of (20 ± 3) ℃ and humidity of (45 ± 5) %. After electrospinning, the collected membrane was dried in an oven at 60 ℃ for 6 h to remove the residual solvent. The dried membrane was shacked in water for 15 min and repeated 3 times to remove unfixed TiO_2 NPs from the membrane. After drying in a 60 ℃ oven for 1 h, the membrane was ready for characterization and photocatalysis.

5.2.3 Characterizations

The morphology of NFs was characterized by a scanning electron microscope (SEM) (JSM-6490, JEOL, Ltd., Tokyo, Japan) with a voltage of 5 kV, all samples were sputtered with a thin Au layer before imaging, and a transmission electron microscopy (TEM) (Tecnai G2, FEI Company, Hillsboro, OR, USA) at 100 kV. Samples for TEM with a cross-section view were embedded in acrylic resin and cut into ultrathin sheets (80 nm-100 nm) with an Ultrotome V (LKB-Produkter AB, Bromma, Sweden) ultramicrotome. The Raman spectroscopy of the membrane was measured by a Raman spectrometer (Micro Raman DRX, Thermo Fisher Scientific, Waltham, MA, USA) with a laser of 532 nm wavelength and a scan range of 200-3500 cm^{-1}. The crystalline phase of the PVDF/TiO_2 membrane was analyzed by X-ray diffraction (XRD) (Bruker D8 Advance, Bruker Italia, Milan, Italy) using an X' Pert PRO diffractometer with radiation (Cu, Kα, 50 kV, 40 mA). Thermogravimetric analysis (TGA) (Q600, TA instruments, New Castle, DE, USA) of the membrane was heated from room temperature to 800 °C at a heating rate of 20 °C min^{-1} in an air atmosphere to evaluate the TiO_2 content.

5.2.4 Photocatalytic experiment

The photocatalytic activity under UV irradiation was monitored by degradation of phenol solution. The same reactor was described in Chapter 4.2.5, but a home-made UV-A LED lamp replaced the UV-C lamp. 100 mg PVDF/TiO_2 CNM were added into a 150 mL phenol aqueous solution with a concentration of 13 mg L^{-1}. The air bubble was supplied by air flow from the bottom of the reactor to mix the solution and CNM. Other operation details remained consistent with Chapter 4.2.5. Reverse phase high-performance liquid chromatography (RP-HPLC) (e2695, Waters, Milford, Massachusetts, United States) with UV/Vis detector (2489, Waters, Milford, Massachusetts, United States) at 275 nm was used to monitor the concentration of phenol during photocatalysis. The phenol concentration at selected intervals and initial were defined as C and C_0, respectively, and a relative concentration was expressed as C/C_0. Plots of the relative concentration as a function of reaction time recorded the degradation activity.

5.3 Results and discussion

5.3.1 Preparation of PVDF/TiO_2 CNMs

Based on simple electrospinning, coaxial electrospinning has additional parameters to be considered: core-shell solution feed rate and solutions compatibility. The preparation of a PVDF nanofiber membrane with good morphology and high piezoelectric behavior via electrospinning has been studied in Chapter 3, hence, the same PVDF solution parameters (DMSO/ACE (2/1) as the solvent and 15% as the concentration) and similar process parameters (0.5 mL/h as the feed rate, the voltage and tip-to-collector distance were adjusted to the practice situation) were considered at the beginning of the preparation. Hence, the TiO_2 suspension parameters (solvent and concentration) and the feed rates of PVDF and TiO_2 solutions were investigated to prepare the hybrid PVDF/TiO_2 core/shell nanofiber membrane.

The core and shell solutions should be immiscible or semi-miscible so that it is possible to form a stable Taylor cone at the spinneret tip, which is a key point for successful electrospinning.[5] Since DMSO and ACE mixture was used as the solvent for the core PVDF solution, DMSO, ACE, and THF were studied as potential solvents for the shell TiO_2 suspension. SEM images of the nanofibrous membranes prepared using TiO_2 suspensions with three different solvents are shown in Figure 5.2. When DMSO was used as the solvent, the surface of NFs was rough because TiO_2 NPs adhered to the smooth PVDF NFs surface to form a layer. However, when THF and ACE were used as the solvent, the surfaces of NFs in two cases were relatively smooth and no TiO_2 NP was found in the image area.

These results should be related to the stability of TiO_2 suspension. Although TiO_2 NPs in DMSO, THF, and ACE suspensions were sonicated for 1 h before electrospinning, TiO_2 NPs precipitated in THF and ACE after 30 min, while TiO_2 NPs well dispersed in DMSO throughout the electrospinning process. TiO_2 NPs tended to agglomerate in THF and ACE, which is caused by the Van der Waals attraction force between particles because of their large surface area. Whereas the TiO_2 NPs remained stable in DMSO due to the balance of the electric interaction between the NPs and solvent molecules and the Van der Waals attraction forces between NPs.[10]

It is evident that PVDF/TiO_2 core/shell CNM was obtained with the help of the stable and dispersal TiO_2 NPs suspension when DMSO was used as the solvent.

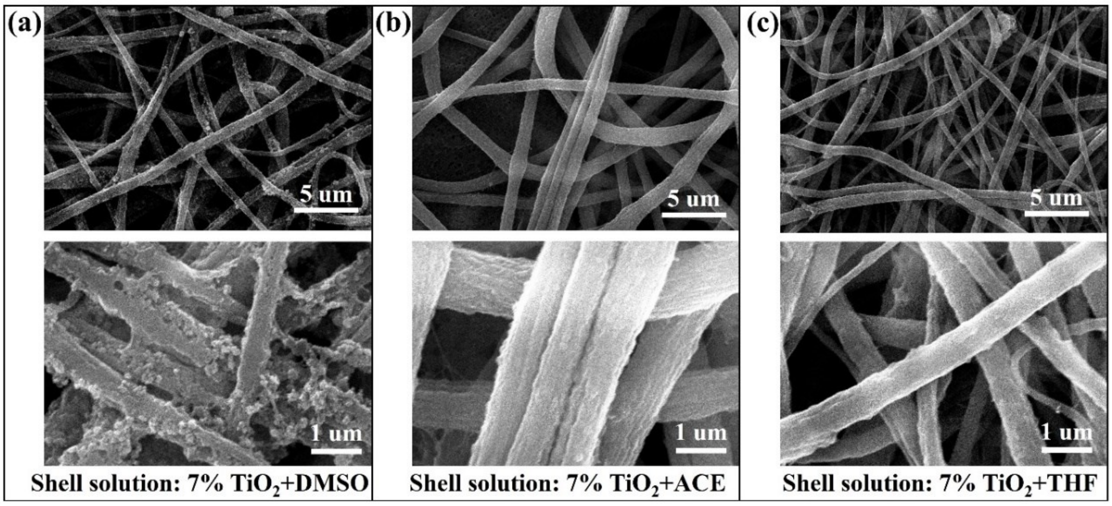

Figure 5.2 SEM images of nanofibrous membranes prepared with different solvents in TiO_2 suspension.

The core/shell feed rate affects the composition of the Taylor corn as well as the thicknesses of core and shell. Figure 5.3 demonstrates the SEM images of PVDF/TiO_2 core/shell CNMs with different core and shell feed rates. When the ratio of core/shell feed rates was low, the morphology of CNMs was not good (the ununiform nanofiber diameters and the appearance of beads) as shown in Figure 5.3(a and e), because of the low polymer concentration in the Taylor corn and the low viscosity solution for electrospinning. When the PVDF fraction in the Taylor corn was high enough, uniform and even nanofibers were obtained as shown in Figure 5.3(b-d).

In the following investigation, the core and shell feed rates of 0.5 ml/h were selected because not only good morphology but also high TiO_2 content were achieved for the as-prepared PVDF/TiO_2 core/shell CNMs.

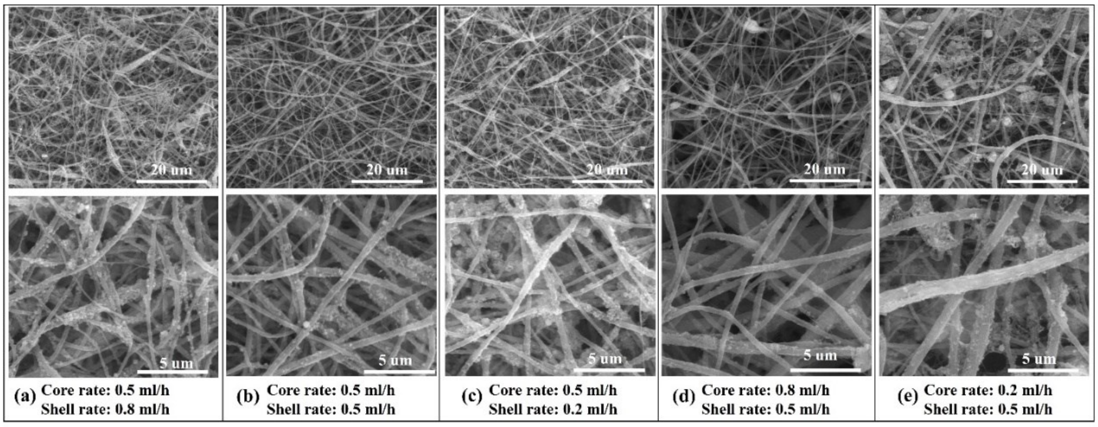

Figure 5.3 SEM images of PVDF/TiO_2 core/shell CNMs prepared with different core/shell feed rates.

The TiO_2 concentration in the suspension affects the TiO_2 amount and the TiO_2 coverage on the PVDF NFs. Figure 5.4 shows the SEM images of PVDF membrane and PVDF/TiO_2 core/shell CNMs with different TiO_2 concentrations in shell suspension. TiO_2 NPs were distributed on the surface of smooth PVDF NFs in all CNMs, forming separate TiO_2 islands when the TiO_2 NPs concentration in shell solution was 5%, as shown in Figure 5.4(b), while forming continuous TiO_2 layers when the concentration was higher than 5%, as shown in Figure 5.4(c-d).

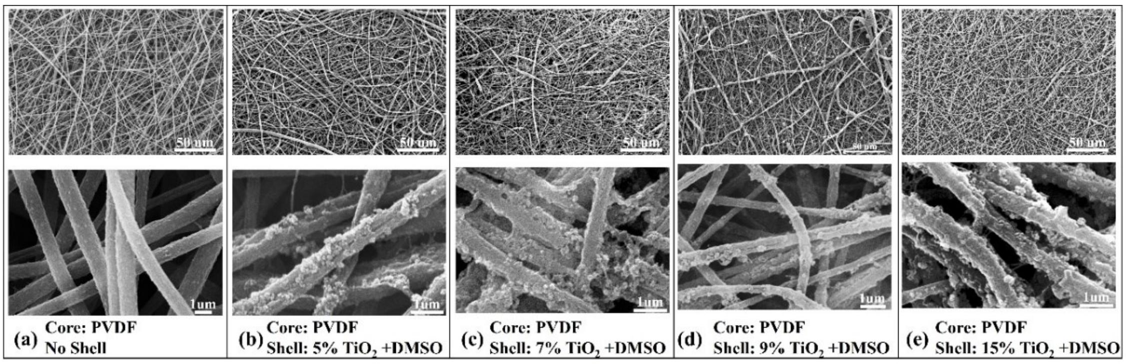

Figure 5.4 SEM images of (a) PVDF membrane and (b-e) PVDF/TiO_2 core/shell CNMs prepared with different TiO_2 NPs concentrations in shell solution.

Therefore, choosing a proper solvent for a stable TiO_2 suspension, a suitable core and shell feed rates, and sufficient TiO_2 concentration in suspension were important for the preparation of PVDF-TiO_2 core-shell CNMs with a continuous TiO_2 layer.

5.3.2 Characterization of the PVDF/TiO_2 CNMs

To confirm the distribution of TiO_2 NPs, TEM images of PVDF/TiO_2 CNMs with side and cross-section views are shown in Figure 5.5. From the side view of TEM images in Figure 5.5(a), the inner part was darker than the outer part, which presented a distinct core-shell structure along nanofibers. The core/shell structure was easier to observe from the cross-section of the TEM image, where dark spots, namely TiO_2 NPs, are attached to each other into a layer over the grey circle, namely the PVDF core. In the side view, the inside was darker than the outside because the inner part of NFs consisted of the core and shell, and the surrounding part was only the shell. The darker TiO_2 shell than the PVDF core in the cross-section view was due to the higher density of TiO_2 based on the same thickness.

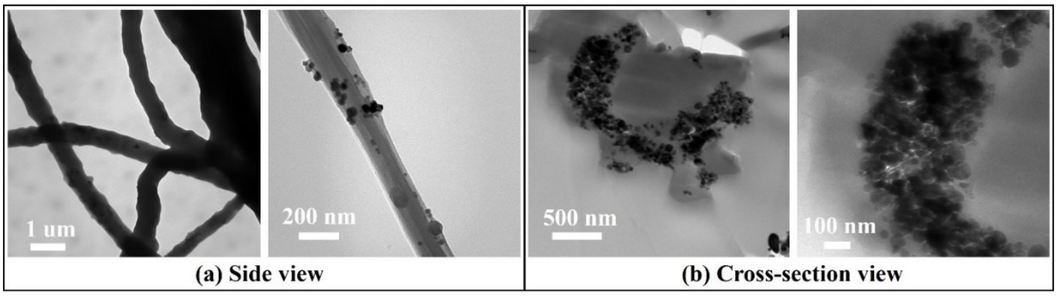

Figure 5.5 The TEM images of PVDF/TiO_2 core/shell CNM (shell: 9% TiO_2 + DMSO) in the views of (a) side and (b) cross-section.

The formation of core/shell nanofiber should be due to the existence of F atoms on the surface of core. The high electronegativity endowed F atoms with the ability to absorb electrons from Ti^{4+} ions, resulting in a strong coordination band between F^- and Ti^{4+} as well as the combination between PVDF core and TiO_2 shell. Han et al.[11] synthesized Sn_3O_4/PVDF hybrid nanofiber membrane by depositing PVDF membrane in precursor solution for hydrothermal treatment and confirmed the coordination effect of F atoms on the connection between Sn_3O_4 and PVDF.

The real TiO_2 fractions in the membranes were obtained from the TGA results and summarized in Table 5.1. With the increase of TiO_2 concentration in shell suspension, the TiO_2 fraction in membrane increased until it reached saturation, which can be reflected in the morphologies in Figure 5.4. The F atoms on the PVDF nanofiber were connected with TiO_2 NPs to form PVDF/TiO_2 core/shell nanofibers. At a relatively low TiO_2 concentration in the shell solution, the TiO_2 amount should determine the attached TiO_2 on the PVDF surface. When there were enough TiO_2 NPs in the shell solution, the TiO_2 fraction should depend on the active F sites.

Table 5.1 TiO_2 fractions in the PVDF/TiO_2 CNMs.

core solution	shell solution	abbreviation	TiO_2 fraction (%)
15% PVDF + DMSO/ACE (2/1)	5% TiO_2 +DMSO	PVDF/TiO_2 CNM-1	11.95
	7% TiO_2 +DMSO	PVDF/TiO_2 CNM-2	17.65
	9% TiO_2 +DMSO	PVDF/TiO_2 CNM-3	22.86
	15% TiO_2 +DMSO	PVDF/TiO_2 CNM-4	23.49

Figure 5.6(a) compares the Raman spectra of PVDF, TiO_2, and PVDF/TiO_2 CNMs with different TiO_2 fractions. PVDF/TiO_2 CNMs showed weak PVDF characteristic peaks at approximately 2978 cm^{-1}, 1428 cm^{-1}, 880 cm^{-1}, 840 cm^{-1}, and 800 cm^{-1} related to the CH_2 wagging, β-combination of CH_2 rocking and CF_2 antisymmetric stretching, the combination of CC antisymmetric stretching and CF_2 symmetric stretching, and α-CH_2 rocking[12,13]. TiO_2 characteristic peaks were recorded at 639 cm^{-1}, 513 cm^{-1}, 440 cm^{-1} and 397 cm^{-1}, corresponding to Eg of anatase, A1g of anatase, Eg of rutile, and B1g of anatase)[14,15], which reflected that the PVDF core was covered well by the TiO_2 shell.

From the XRD spectra in Figure 5.6(b), PVDF in CNM was proved to be in the crystalline phase because of the existence of a PVDF diffraction peak, which was the basis for the piezoelectricity of PVDF. The XRD spectra of CMN were indeed composed of two components, PVDF and TiO_2. In addition, the TiO_2 fraction in membrane increased from CMN-1 to CMN-4 by comparing the intensity ratio between the TiO_2 peak at 25.3° and the PVDF peak at 20.5°.

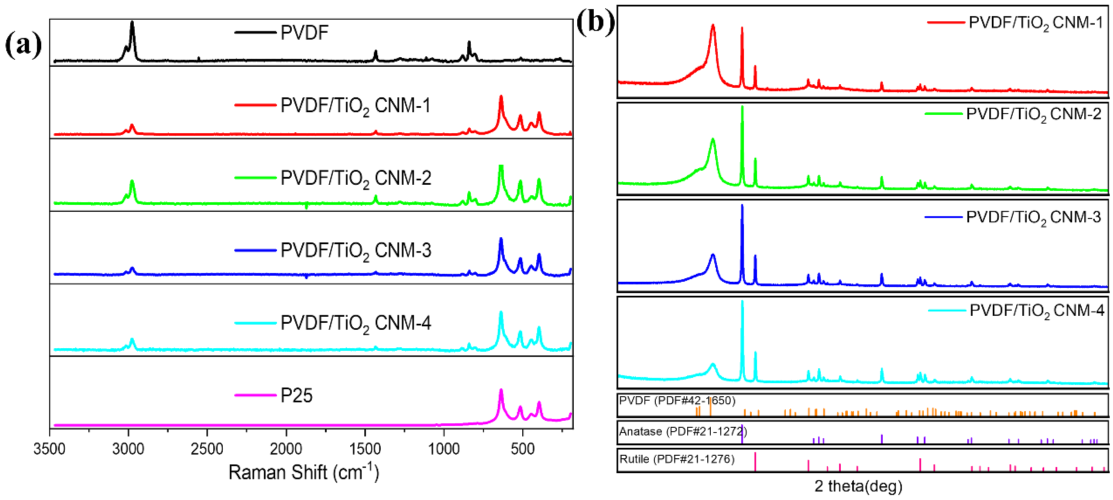

Figure 5.6 (a) Raman spectra of PVDF membrane, PVDF/TiO₂ CNMs, and P25 NPs; (b) XRD spectra of PVDF/TiO₂ CNMs and corresponding PDF standard patterns

5.3.3 Photocatalytic activity

As mentioned in the literature, dye decolorization is not suitable for evaluating the activity of photocatalysts because 1). Dye can absorb light and degrade itself; 2). Dye is reflected by the chromophore groups and monitored by absorbance measurement, which increases the inaccuracy of the measurement.[16] Hence, phenol degradation was used to evaluate the photocatalytic performance of PVDF/TiO_2 CNM prepared via coaxial electrospinning, and the PVDF/TiO_2 CNM-2 was used as a catalytic membrane because it has relatively saturated TiO_2 content. Figure 5.7(a and b) shows the photocatalytic performances of blank and PVDF/TiO_2 CNM-2 under UV only, air flow at 2 NL/min (F2) only, as well as UV and air flow at 2 NL/min (UV+F2).

Only UV-induced degradation occurred in the blank groups. The photocatalytic activities were slower under UV+F2 than under UV only, which was because the bubbles blocked the UV irradiation and inhibited the photocatalytic activity. Phenol degradation was improved under UV+F2 than under UV only and F2 only. Phenol can be completely degraded under UV+F2 when PVDF/TiO_2 CNM was used as the photocatalyst, while only 25% phenol was degraded without photocatalyst, which meant that around 75% phenol was degraded due to the existence of PVDF/TiO_2 CNM. To assess the catalyst efficiency, the degraded phenol per gram of TiO_2 for PVDF/TiO_2 CNM-2 under UV+F2 was investigated as a function of the time in Figure 5.7(c). After 2 h under UV+F2, about $1x10^{-6}$ mol phenol was degraded per 1 mg TiO_2 on CNM. Hence, PVDF/TiO_2 CNM exhibited excellent photocatalytic efficiency.

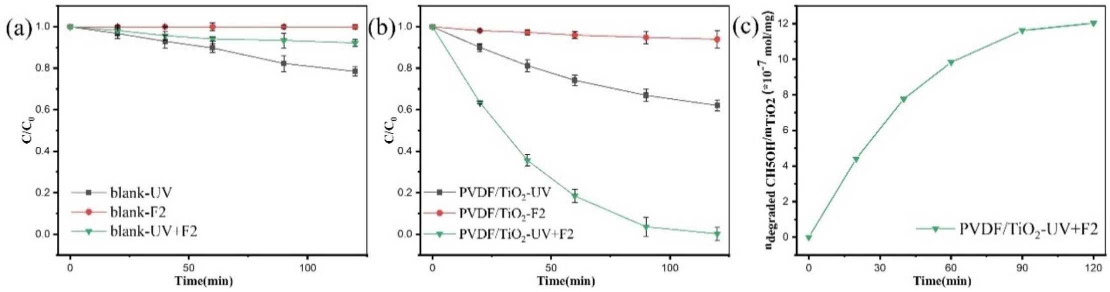

Figure 5.7 Photocatalytic performances of (a) blank and (b) PVDF/TiO_2 CNM under UV only, F2 only, and UV+F2; (c) the phenol degradation per grams of TiO_2 on CNM as a function of time.

Photocatalytic activity of PVDF/TiO_2 CNM-2 under UV+F2 was carried out three times, as shown in Figure 5.8. Compared with the first one, the second photocatalytic activity of the same piece of PVDF/TiO_2 CNM was a little reduced, while the third cycle had a reduction in degraded phenol amount. The photocatalytic efficiency stability of PVDF/TiO_2 CNM prepared via coaxial electrospinning was slight poor, which should be due to the little loss of TiO_2 during the photocatalytic activity and cleaning process.

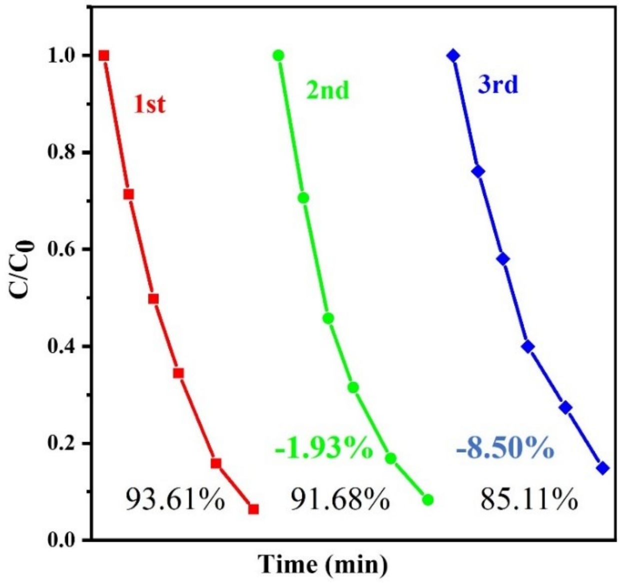

Figure 5.8 Repeated photocatalytic experiments of PVDF/TiO_2 CNM-3 under UV+F2 (the time for points on curves are 0, 20, 40, 60, 90, and 120 min). (Black numbers and color numbers presented the degraded phenol and the catalyst deactivation of each cycle compared to the first cycle)

5.4 Conclusion

In this chapter, PVDF/TiO_2 core/shell CNMs were prepared by coaxial electrospinning with appropriate parameters (appropriate solvent for a stable TiO_2 suspension, suitable core/shell feed rates, and sufficient TiO_2 concentration in suspension). Based on the blank under UV+F2, around 75% phenol was degraded due to the existence of PVDF/TiO_2 CNM. Besides, the PVDF/TiO_2 CNM exhibited excellent photocatalytic performance even after the third reuse but had slight weak stability.

References

(1) Gupta, S. M.; Tripathi, M. A review of TiO_2 nanoparticles. *chinese science bulletin* **2011**, *56*, 1639-1657.

(2) is Degussa, W. P25? Crystalline composition analysis, reconstruction from isolated pure particles and photocatalytic activity test, Ohtani B., Prieto-Mahaney OO, Abe R. *Journal of Photochemistry and Photobiology A: Chemistry* **2010**, *216*, 179-182.

(3) Han, D.; Steckl, A. J. Coaxial electrospinning formation of complex polymer fibers and their applications. *ChemPlusChem* **2019**, *84*, 1453-1497.

(4) Qu, H.; Wei, S.; Guo, Z. Coaxial electrospun nanostructures and their applications. *Journal of Materials Chemistry A* **2013**, *1*, 11513-11528.

(5) Yoon, J.; Yang, H. S.; Lee, B. S.; Yu, W. R. Recent progress in coaxial electrospinning: New parameters, various structures, and wide applications. *Advanced Materials* **2018**, *30*, 1704765.

(6) McCann, J. T.; Marquez, M.; Xia, Y. Melt Coaxial Electrospinning: A Versatile Method for the Encapsulation of Solid Materials and Fabrication of Phase Change Nanofibers. *Nano Letters* **2006**, *6*, 2868-2872.

(7) Pant, B.; Park, M.; Park, S.-J. Drug delivery applications of core-sheath nanofibers prepared by coaxial electrospinning: a review. *Pharmaceutics* **2019**, *11*, 305.

(8) Yu, D.-G.; Chian, W.; Wang, X.; Li, X.-Y.; Li, Y.; Liao, Y.-Z. Linear drug release membrane prepared by a modified coaxial electrospinning process. *J Membrane Sci* **2013**, *428*, 150-156.

(9) Jiang, H.; Hu, Y.; Zhao, P.; Li, Y.; Zhu, K. Modulation of protein release from biodegradable core–shell structured fibers prepared by coaxial electrospinning. *Journal of Biomedical Materials Research Part B: Applied Biomaterials: An Official Journal of The Society for Biomaterials, The Japanese Society for Biomaterials, and The Australian Society for Biomaterials and the Korean Society for Biomaterials* **2006**, *79*, 50-57.

(10) Delforce, L.; Hofmann, E.; Nardello-Rataj, V.; Aubry, J.-M. TiO_2 nanoparticle dispersions in water and nonaqueous solvents studied by gravitational sedimentation analysis: Complementarity of Hansen Parameters and DLVO interpretations. *Colloids and Surfaces A: Physicochemical and Engineering Aspects* **2021**, *628*, 127333.

(11) Han, S.; Chen, D.; Wang, J.; Liu, Z.; Liu, F.; Chen, Y.; Ji, Y.; Pang, J.; Liu, H.; Wang, J. Assembling Sn_3O_4 nanostructures on a hydrophobic PVDF film through metal-F coordination to construct a piezotronic effect-enhanced Sn_3O_4/PVDF hybrid photocatalyst. *Nano Energy* **2020**, *72*, 104688.

(12) Ma, J.; Zhang, Q.; Lin, K.; Zhou, L.; Ni, Z. Piezoelectric and optoelectronic properties of electrospinning hybrid PVDF and ZnO nanofibers. *Materials Research Express* **2018**, *5*, 035057.

(13) Elashmawi, I.; Gaabour, L. Raman, morphology and electrical behavior of nanocomposites based on PEO/PVDF with multi-walled carbon nanotubes. *Results in Physics* **2015**, *5*, 105-110.

(14) Hearne, G.; Zhao, J.; Dawe, A.; Pischedda, V.; Maaza, M.; Nieuwoudt, M.; Kibasomba, P.; Nemraoui, O.; Comins, J.; Witcomb, M. Effect of grain size on structural transitions in anatase TiO_2: A Raman spectroscopy study at high pressure. *Physical Review B* **2004**, *70*, 134102.

(15) Šcepanovica, M.; Aškrabica, S.; Bereca, V.; Golubovica, A.; Dohcevic-Mitrovica, Z.; Kremenovicb, A.; Popovica, Z. In *Tilte*2008.

(16) Bae, S.; Kim, S.; Lee, S.; Choi, W. Dye decolorization test for the activity assessment of visible light photocatalysts: Realities and limitations. *Catal Today* **2014**, *224*, 21-28.

Chapter VI Preparation of PVDF/TiO_2 core/shell nanofibers via atomic layer deposition

Abstract

A TiO_2 nanolayer with controllable thickness was deposited on the surface of PVDF electrospun nanofibers via atomic layer deposition (ALD), and then the amorphous TiO_2 was converted into crystalline one by hydrothermal treatment. Detailed morphological and structural characterizations of PVDF/TiO_2 CNMs at each preparation stage were given. The thickness and weight of the TiO_2 deposit were related to the ALD cycle number. The effect of hydrothermal annealing parameters on TiO_2 and PVDF have been investigated to obtain suitable parameters. Phenol was chosen as a probe molecular to evaluate the photocatalytic efficiency of PVDF/TiO_2 CNMs prepared via ALD.

Keywords: atomic layer deposition, core-shell composite nanofibrous membrane, photocatalysis, wastewater treatment.

6.1 Introduction

Due to the increasing demand for fresh and clean water sources, photocatalysis, an advanced oxidation process involving irradiation and photocatalyst, is a promising technique in the field of water and environmental purification. Among the semiconductors employed as photocatalysts, titanium dioxide (TiO_2) has attracted much attention because of its high photocatalytic efficiency, non-toxicity, low cost, etc. However, the applications of TiO_2 as a photocatalyst are hindered by the limited photocatalytic efficiency and the difficult recovery from solution after use.

When TiO_2, usually in powder form, is combined with a flexible polymer film, the hybrid photocatalyst is possible to be manipulated and recovered.[1,2] Moreover, compared with a polymer film, a micro- or nano-fiber polymer membrane is beneficial to increase the surface area for photocatalytic reaction. Electrospinning is a common and simple technique for fabricating fiber membranes with a wide range of fiber diameters.

PVDF, an attractive polymer with outstanding mechanical properties, was considered to combine with TiO_2 in the form of nanofiber (NF) and used for photocatalysis. Furthermore, a core/shell structure of NF (PVDF as core and TiO_2 as sheath) was proposed to expose TiO_2 outside the PVDF NFs and achieve good contact between PVDF and TiO_2. From the literature[1], the core/shell NFs can be obtained by methods such as hydrothermal treatment, physical/chemical vapor deposition on electrospun membranes, and combinations of electrospinning and electrospraying. Cationic titanium dioxide (TiO_2^+) was immobilized on the surface of electrospun PVA/PAA NFs by the electrostatic layer-by-layer (LBL) assembly, and the thickness of TiO_2^+ layer for each LBL cycle was about (3050) nm.[3] A functionalized PVA/PAA/GO-COOH electrospun nanofibrous membrane was immersed into a TiO_2 nanoparticles (NPs) suspension, and a PVA/PAA/GO-COOH@TiO_2 nanocomposite was formed due to functional groups anchoring TiO_2 NPs. This method was complicated and inapposite for most polymers.[4] Conductive CSA/PANi-PEO composite electrospun fibers were used as conductive collectors for the electrospray of TiO_2 NPs suspension.[5] The distribution of TiO_2 NPs on the surface of CSA/PANi-PEO fibers was not uniform and the TiO_2 NPs amount on NFs was random. For the above methods, the distribution of TiO_2 on the surface of NFs is difficult to achieve a uniform layer, especially in the dense and porous NFs membranes, the thickness is uncontrollable, and the suitable polymers for core are limited.

Atomic layer deposition (ALD) is a low-temperature chemical vapor deposition technique in which the growth of material is controlled by sequential self-saturating gas-solid surface reactions. ALD has been widely adopted to deposit a uniform, conformal, and compact layer with atomic layer precision on substrates. There are some papers detailing ALD, from fundamental principles (such as characteristics, parameters effects, growth process, and mechanism) to applications,[6,7] and even on the combination of electrospinning and ALD[8,9]. Thickness control via ALD has been investigated on electrospun NFs[8], SiO_2/Si substrate[10], and particle templates[11], and it has been demonstrated that ALD can grow desired thickness, even monolayer, on substrates and the thickness is related to the cycle number. Low-temperature ALD has been applied to grow TiO_2, Al_2O_3, ZnO, etc. on substrates to avoid thermal damage to the substrates.[12-14] Therefore, ALD becomes the best suitable method to deposit a TiO_2 layer with a controllable thickness on the surface of NFs in the electrospun membrane without damaging the membrane.

Herein, PVDF/TiO_2 core/shell composite nanofiber membrane (CNM) with excellent morphology and good photocatalytic efficiency were obtained by performing subsequently: electrospinning, ALD, and hydrothermal treatment. PVDF NFs membrane was prepared by electrospinning as the core, a TiO_2 layer with different thicknesses was uniformly coated NFs via ALD as the sheath, and then hydrothermal treatment was applied to crystallize the amorphous TiO_2 layer. In the end, phenol degradation was used to evaluate the photocatalytic activities of PVDF/TiO_2 core/shell

CNM. The effect of the thickness of TiO_2 layer on photocatalytic efficiency and the stability of photocatalyst were also studied.

6.2 Experimental section

6.2.1 Materials

PVDF (KYNAR 500) was purchased from Arkema. Acetone (ACE), dimethyl sulfoxide (DMSO), and phenol were purchased from Sigma Aldrich. Tetrakis (dimethylamino) titanium (TDMAT) (99%) was obtained from Strem Chemicals. All reagents were used as received without any further processing. Milli-Q water was used throughout the whole experiment.

6.2.2 Preparation of PVDF/TiO_2 CNMs

PVDF NFs membrane was prepared by electrospinning technique. PVDF in DMSO and ACE (weight ratio 2:1) solution with a concentration of 15 wt% was used for electrospinning. The working voltage and the distance between the collector and spinneret were 12 kV and 15 cm. The process was carried out in an atmospheric environment with a temperature of (20 ± 3) °C and humidity of (45 ± 5) %. After electrospinning, the collected membrane was dried in an oven at 60 °C for 6 h to remove the residual solvent.

ALD technique was employed to PVDF NFs membrane for coating a TiO_2 layer on the surface of NF, which was defined as PVDF/TiO_2-A (amorphous) core/shell CNM. A piece of PVDF NFs membrane was placed in a Savanna 100 ALD machine (Ultratech/Cambridge Nanotech Inc.) and the deposition process was processed at 90 °C and 1 mbar. TDMAT and H_2O were preheated to 90 °C and 115 °C (to obtain steam) as precursors for titanium and oxygen, respectively. The pulse and purge durations were 0.3 s and 10 s for TDMAT as well as 0.045 s and 10 s for H_2O. N_2 was used as the carrier inert gas at a flow rate of 21 sccm.

Hydrothermal treatment of PVDF/TiO_2-A CNM was carried out in a Teflon-lined autoclave (100 mL volume) with 30 mL water as the heating medium. The autoclave containing the sample was heated in a microwave oven (MicroSYNTH, Milestone Srl, Sorisole, Italy) at a set temperature for a period at a heating rate of 20 °C min^{-1} and cooled naturally. Annealed PVDF/TiO_2-A CNM was defined as PVDF/TiO_2-C (crystalline) CNM.

6.2.3 Characterizations

The morphology of the membranes was studied by using a scanning electron microscope (SEM) (JSM-6490, JEOL, Ltd., Tokyo, Japan) at 5 kV and a thin Au layer was sputtered on all samples before imaging. Transmission electron microscopy (TEM) ((Tecnai G2, FEI Company, Hillsboro, OR, USA) with a voltage of 100 kV was used to observe the cross-section of PVDF/TiO_2 NFs embedded in acrylic resin and cut into ultrathin sheets with an Ultrotome V (LKB-Produkter AB, Bromma, Sweden) ultramicrotome. The TiO_2 thickness of different PVDF/TiO_2 NFs CNMs was measured from 50 random sheaths in TEM images by Image J software. The crystalline phase of PVDF/TiO_2 NFs CNMs was obtained by X-ray diffraction (XRD) (Bruker D8 Advance, Bruker Italia, Milan, Italy) using an X' Pert PRO diffractometer with radiation (Cu, Kα, 50 kV, 40 mA). The TiO_2 fraction in CNMs was evaluated by Thermogravimetric analysis (TGA) (Q600, TA instruments, New Castle, DE, USA) at 700 ℃ in the air atmosphere at a heating rate of 20 ℃ min^{-1}. The crystallinity of PVDF in PVDF/TiO_2 NFs CNMs was analyzed by differential scanning calorimetry (DSC) (Q200, TA instruments, New Castle, DE, USA) from 40 °C to 250 °C at a rate of 10 °C/min in a nitrogen atmosphere.

6.2.4 Photocatalytic experiment

The photocatalytic performance of PVDF/TiO_2 CNMs was investigated by the degradation of phenol. PVDF/TiO_2 CNM with the same area (20 cm^2) was immersed in 150 mL phenol aqueous solution with a concentration of 13 mg L^{-1}. The photocatalytic activities were carried out under UV-A irradiation and air bubbles. Other photocatalytic details were the same as in Chapter 5.2.4.

6.3 Results and discussion

6.3.1 Fabrication and characteristics of PVDF/TiO_2-A core/shell CNMs

To prepare a PVDF membrane with a high piezoelectric property via electrospinning, a solvent with a high dipole moment and appropriate electrospinning parameters obtained from Chapter 3 were applied here. TDMAT and H_2O in steam were selected as the precursors for Ti and O sources for the reaction because TDMAT is a non-toxic and non-corrosive precursor of TiO_2, and H_2O is a simple oxidant.[15,16] To avoid thermal damage to PVDF, a relatively low temperature, 90 °C, was applied as the deposition temperature. According to the previous ALD experiment[17], the growth per cycle (GPC) for TiO_2 deposition under the same parameters was 0.068 nm/cycle, which was obtained by measuring the coating thickness using X-ray reflectivity on Si wafer substrates. To find out the effect of TiO_2 thickness on the photocatalysis of PVDF/TiO_2 CNMs, TiO_2 layers with three thickness were obtained through 1300, 631, and 298 ALD cycles.

The white PVDF membrane turned brown after ALD, and the brown color of PVDF/TiO_2-A CNM deepened with the increase of cycle number, reflecting the deposition of TiO_2 layer and the increase of TiO_2 thickness. SEM images of PVDF/TiO_2-A-298, -613, and -1300 CNMs in Figure 6.1 showed that the NFs after deposition had a continuous and smooth morphology. The TiO_2 layer formed on the surface of PVDF core was speculated from the cracks on the NFs because of the fragile feature of TiO_2.

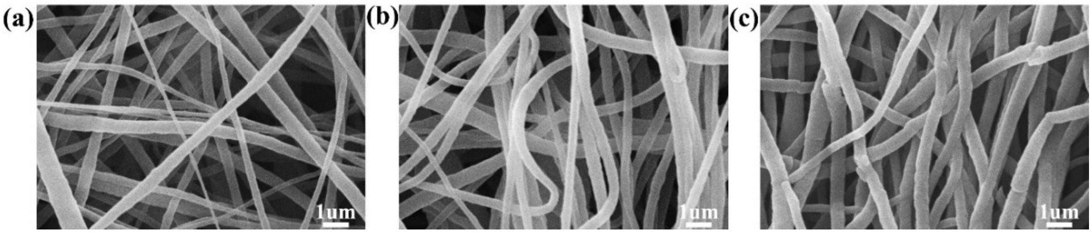

Figure 6.1 SEM images of PVDF/TiO_2-A CNMs prepared via (a) 298, (b) 613, and (c) 1300 ALD cycles.

To confirm the core/shell structure of NFs and to obtain the thickness of the TiO_2 layer, TEM images of the cross-section of PVDF/TiO_2-A CNMs were carried out. From TEM images in Figure 6.2(a-c), uniform black circles (TiO_2 deposit layers) covered gray rounds (PVDF NFs), which was strong evidence of the core/shell structure. After 298, 613, and 1300 ALD cycles, the thickness of TiO_2 deposit on PVDF core were (25.99 ± 3.7) nm, (58.45 ± 7.7) nm, and (98.25 ± 9.3) nm, respectively, measured by Image J software. The actual thicknesses of TiO_2 deposit were different from the expected values (around 90 nm, 45 nm, and 20 nm), calculated by multiplying the cycle number by the GPC value for this deposition process, which was due to the different thickness measurement methods and various substrates.[17]

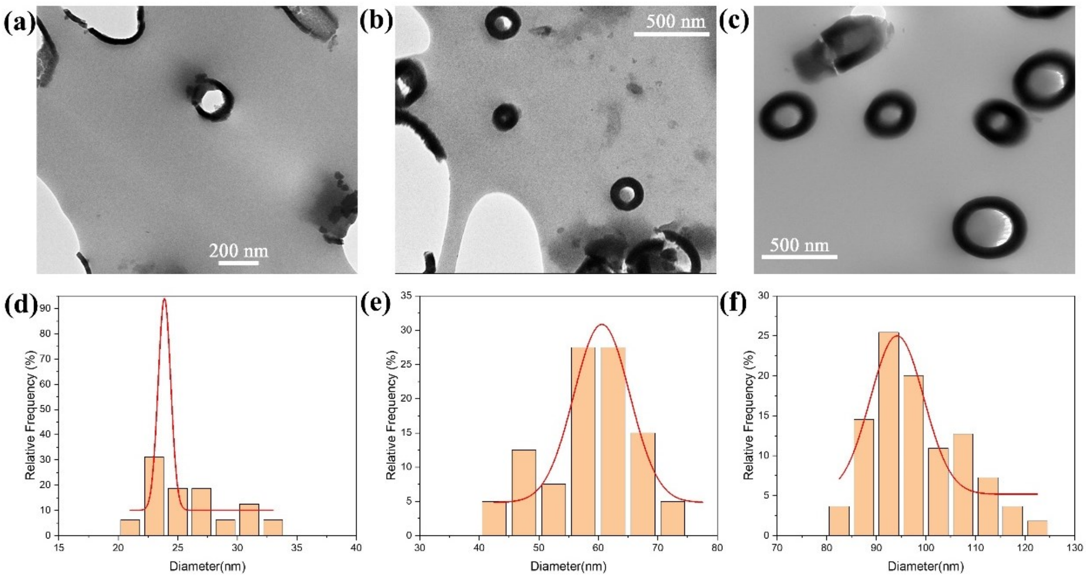

Figure 6.2 TEM images and TiO_2 thickness distribution histograms of PVDF/TiO_2-A CNMs prepared via (a and d) 298, (b and e) 613, and (c and f) 1300 ALD cycles.

The TiO_2 contents in PVDF/TiO_2-A CNMs were obtained from TGA results in Figure 6.3: 14.0%, 36.3%, and 62.5% after 298, 623, and 1300 cycles, respectively. Besides, the weight of CNMs after PVDF degradation kept steady at (550800) °C, which meant that no impurity existed in the CNMs. Both the TiO_2 thickness and the TiO_2 weight of CNMs, recorded in Table 6.1, were proportional to the ALD cycle number.

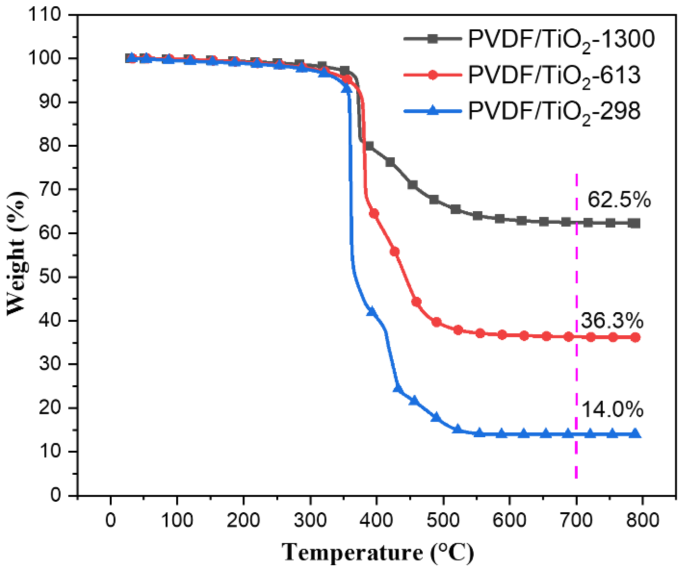

Figure 6.3 TGA curves of PVDF/TiO_2-A CNMs with three ALD cycles.

Table 6.1 Information on the PVDF/TiO_2-A CNMs.

Sample names	ALD cycles	TiO_2 thickness (nm)	TiO_2 weight (%)
PVDF/TiO_2-A-298	298	25.99 ± 3.7	14.0
PVDF/TiO_2-A-613	613	58.45 ± 7.7	36.3
PVDF/TiO_2-A-1300	1300	98.25 ± 9.3	62.5

6.3.2 Crystallization and characteristics of PVDF/TiO_2-C core/shell CNMs

Due to the relatively low deposition temperature, the formed TiO_2 sheath was in amorphous phase, which had no photocatalytic ability. Annealing treatment was applied to the PVDF/TiO_2-A CNMs to crystallize TiO_2. In the beginning, regular annealing on

PVDF/TiO_2-C CNM-1 was performed in a furnace at 120 °C for 48 h, but its XRD pattern, as shown in Figure 6.4, was the same as that of PVDF/TiO_2-A CNM. While the PVDF/TiO_2-C CNM-2 was hydrothermally annealed in an autoclave, heated in a microwave oven at 120 °C for 2 h, and a small peak corresponding to the anatase phase appeared in its XRD pattern. Two results meant that hydrothermal annealing was helpful in crystallizing TiO_2 in this work. To achieve higher TiO_2 crystallization, higher temperatures (140 °C and 160 °C) and longer heating times (2 h and 4 h) were applied to PVDF/TiO_2-A CNMs. The morphology and TiO_2 content of PVDF/TiO_2-C CNMs after annealing were analyzed, and no obvious change was observed.

The XRD patterns of initial PVDF/TiO_2-A-1300 CNM and PVDF/TiO_2-C-1300 CNMs with different annealing parameters are shown in Figure 6.4. The XRD pattern of PVDF/TiO_2-A-1300 mainly consisted of a diffraction peak at 2θ=20.6°, corresponding to the β phase (110) plane of PVDF (JCPDS card: 42-1650), and a hump between 23-35°, which related to the amorphous TiO_2. After hydrothermal annealing at 140 °C or 160 °C for 2 h or 4 h, the diffraction peaks of TiO_2 became sharp and the PVDF peak appeared weak. The diffraction peaks located at 2θ values of 25.3°, 37.9°, 48.0°, 54.0°, 55.0°, and 62.7° were assigned to the (101), (004), (200), (105), (211), and (204) planes of the anatase TiO_2 (JCPDS card: 21-1271), separately. A weak diffraction peak at 2θ=30.9° should correspond to the (121) plane of the brookite TiO_2 (JCPDS card: 29-1360), and the strongest peak ((120) plane) of the brookite phase was not seen because it should be at around 25.4°, which coincided with the strongest peak of the anatase phase at 25.3°. Ignoring the effect of the brookite (120) plane because of the low brookite fraction, the average crystallite size on the anatase (101) plane of PVDF/TiO_2-C-1300 CNMs was calculated via the Scherrer equation. The results were reported in Table 6.2, which showed that the crystallite size increased with the increase in treatment temperature and/or time. Besides, according to the reference intensity ratio (RIR) value of anatase and brookite phases, the anatase/brookite phase fractions of TiO_2 should be (94.0%/6.0%) + few amorphas after the annealing at 140 °C for 2 h, 93.0%/7.0% after the annealing at 140 °C for 4 h, 85.5%/14.5% after the annealing at 160 °C for 2 h, and 92.0%/8.0% after the annealing at 160 °C for 4 h, as summarized in Table 6.2.

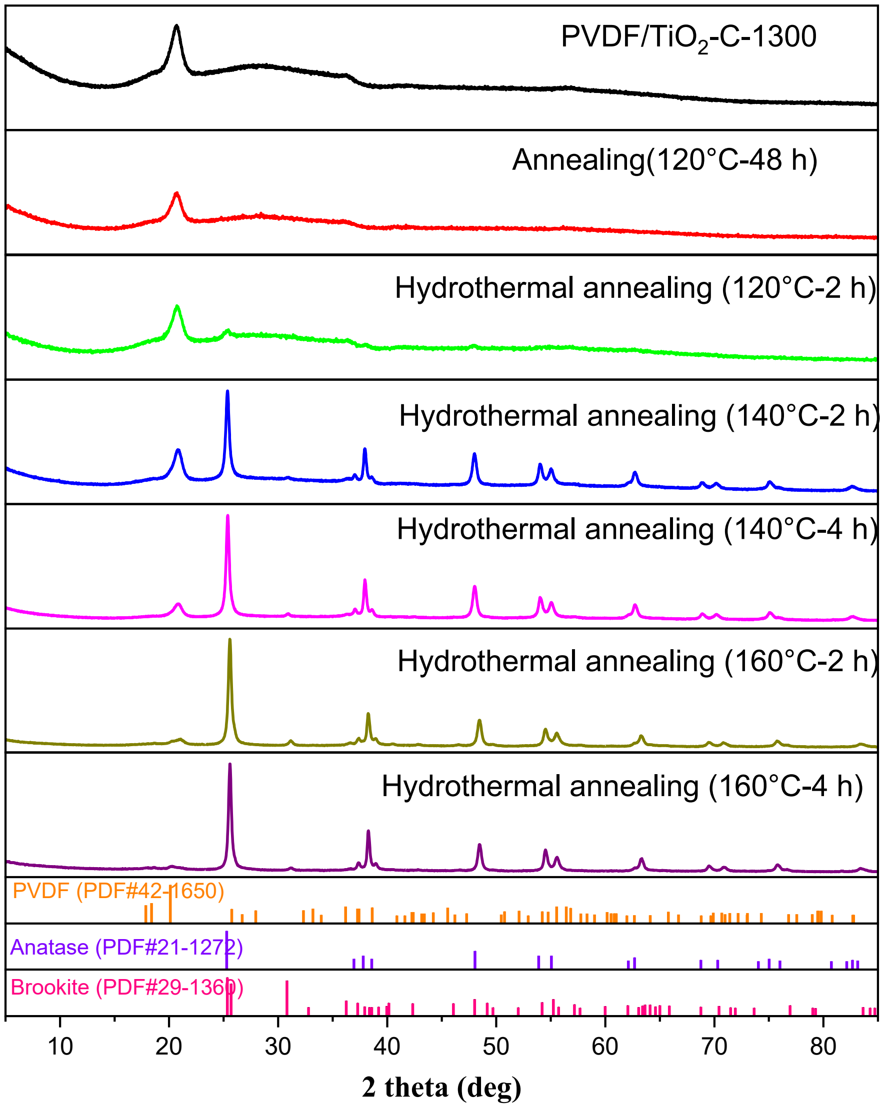

Figure 6.4 XRD patterns of the initial PVDF/TiO_2-C-1300 CNM, the annealed PVDF/TiO_2-A-1300 CNMs, and corresponding PDF standard patterns.

Table 6.2 Information of the initial PVDF/TiO_2-C-1300 CNM and annealed PVDF/TiO_2-A CNMs.

Sample names	Annealing	$D_{(101)}$ (nm)	TiO_2 crystalline phase	Enthalpy of fusion (J g^{-1})	Crystallinity (%)
PVDF/TiO_2-A-1300	/		amour.	15.33	39.04
PVDF/TiO_2-1300-1	A[1], 120 °C, 48 h		amour.	17.1	43.55
PVDF/TiO_2-1300-2	HA[2], 120 °C, 2 h		amour. + few anatase	17.54	44.67
PVDF/TiO_2-1300-3	HA, 140 °C, 2 h	19.0	(94.0% anatase + 6.0% brookite) + few amour.	17.66	44.98
PVDF/TiO_2-1300-4	HA, 140 °C, 6 h	20.9	93.0% anatase + 7.0% brookite	17.03	43.37
PVDF/TiO_2-1300-5	HA, 160 °C, 2 h	21.1	85.5% anatase +14.5% brookite	12.42	31.63
PVDF/TiO_2-1300-6	HA, 160 °C, 4 h	23.2	92.0% anatase +8.0% brookite	11.06	28.17

1: Conventional annealing in a furnace; 2: Hydrothermal annealing in an autoclave heated by a microwave oven.

The PVDF melting situation of CNMs was learned from their DSC curves, and the PVDF crystallinity was calculated according to the Equation below:

$$X_c = \frac{\Delta H}{\Delta H_\mathrm{m} \cdot \varphi} \times 100\%$$

where ΔH is the melting enthalpy of CNMs obtained from the DSC curve, ΔH_m is the melting enthalpy of PVDF with 100% crystallinity, 104.7 J g^{-1}, and φ is the PVDF weight fraction, 37.5%, obtained from the TGA result.

The melting enthalpy and crystallinity of CNMs were reported in Table 6.2. After annealing at 120 °C and 140 °C, the PVDF crystallinity in CNMs increased because annealing is beneficial for crystal growth. Whereas, after annealing at 160 °C, the crystallinity of PVDF in CNMs decreased, implying partial melting of PVDF. Hence, in terms of crystallinity and phase fraction, the optimal annealing parameters for PVDF/TiO_2-A CNMs should be hydrothermal annealing at 140 °C for 4 h.

6.3.3 Photocatalytic activity

Phenol photocatalytic activities under UV and air flow at 2 NL/min (UV+F2) on CNMs with the same area (20 cm^2) were performed and the results were shown in Figure 6.5(a and b). Nearly 10% phenol was degraded when the PVDF/TiO_2-A CNMs were applied as catalysts, which was a similar phenol degradation amount under UV+F2 in blank group without any photocatalyst (as shown in Figure 7.1(a)). It showed as expected that the amorphous TiO_2 has no photocatalytic efficiency. After hydrothermal annealing at 140 °C for 4 h, the PVDF/TiO_2-C CNMs, even with different membrane weights and TiO_2 fractions, exhibited similar photocatalytic behaviors, with approximately 50% phenol being degraded. It meant that no matter the thickness of the TiO_2 layer on PVDF NFs, only the outer surface of TiO_2 layer can participate in phenol degradation. The degraded phenol per gram of TiO_2 as a function of reaction time was plotted in Figure 6.5(c). PVDF/TiO_2-298-4 CNM exhibited the best phenol degradation efficiency per TiO_2 due to the thinnest TiO_2 layer. Therefore, in order to reduce the material and cost as well as maximize the utilization of TiO_2, it is better to produce the PVDF/TiO_2 CNM with a TiO_2 layer as thin as possible on the surface of PVDF NFs.

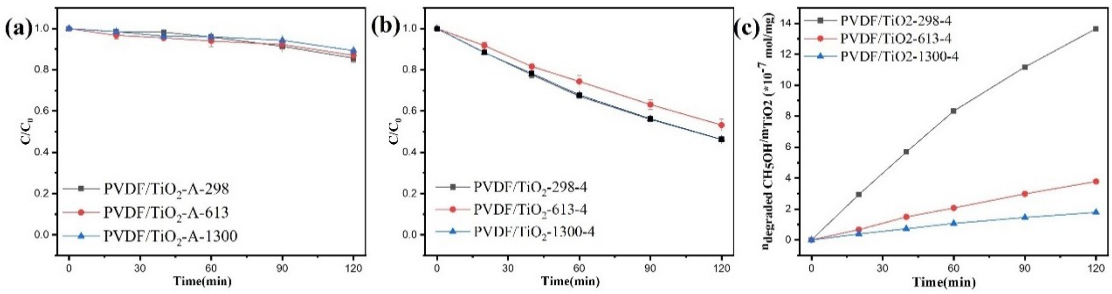

Figure 6.5 Photodegradation profiles of phenol for (a) PVDF/TiO_2-A CNMs and (b) PVDF/TiO_2-C CNMs (hydrothermal annealing at 140 °C for 4 h) under UV+F2, (c) the degraded phenol per TiO_2 as a function of reaction time.

Compared with PVDF/TiO_2-A CNMs, phenol degradation was enhanced by 40% in the presence of PVDF/TiO_2-C CNMs. The relatively weak phenol degradation should be due to the limited photocatalytic efficiency of the synthesized TiO_2 layer after hydrothermal annealing at 140 °C for 4 h, which was the optimal annealing parameters to crystallize TiO_2 and to avoid PVDF damage, instead of to obtain TiO_2 with good photocatalytic efficiency. In addition, the degraded phenol per TiO_2 of PVDF/TiO_2-298-4 CNM was similar to that of PVDF/TiO_2 CNM prepared via coaxial electrospinning (as shown in Figure 5.7(c)), so only 40% enhancement on phenol degradation here should also be related to the limited amount of photocatalytic membrane.

Photocatalytic activity under UV+F2 of the PVDF/TiO_2-298-4 CNM was carried out three times, as shown in Figure 6.6. The degraded phenol after the first, second, and third cycle was 55.38%, 55.03%, and 53.65%, and phenol degradation was reduced by 1.73% after three repeated uses. Hence, the PVDF/TiO_2 core/shell CNM prepared via ALD presented a stable photocatalytic efficiency.

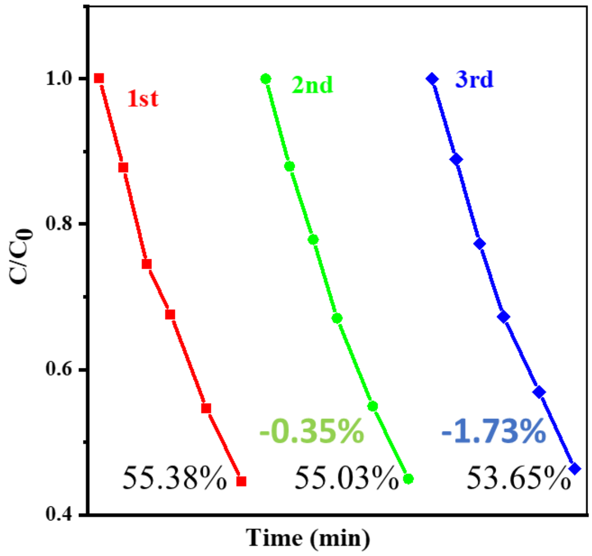

Figure 6.6 C/C_0 of PVDF/TiO_2-298-4 CNM as a function of regular interval for three cycles of phenol degradation. (Black numbers and color numbers presented the degraded phenol and the catalyst deactivation of each cycle compared to the first cycle)

6.4 Conclusion

In this chapter, PVDF/TiO_2 core/shell CNMs with excellent morphology were prepared by ALD based on PVDF nanofibers and following hydrothermal treatment. The homogeneous and thickness-controllable TiO_2 layers were deposited on the surface of PVDF nanofibers in a dense and porous electrospun nanofiber membrane. Therefore, ALD is an ideal technique to prepare core/shell nanofibers. In addition, the PVDF/TiO_2

core/shell CNMs after proper hydrothermal treatment had an effective and stable photocatalytic efficiency, degrading 40% phenol under the effect of annealed PVDF/TiO_2 core/shell CNM.

References

(1) Shan, A. Y.; Ghazi, T. I. M.; Rashid, S. A. Immobilisation of titanium dioxide onto supporting materials in heterogeneous photocatalysis: A review. *Applied Catalysis A: General* **2010**, *389*, 1-8.

(2) Singh, S.; Mahalingam, H.; Singh, P. K. Polymer-supported titanium dioxide photocatalysts for environmental remediation: A review. *Applied Catalysis A: General* **2013**, *462-463*, 178-195.

(3) Deb, H.; Xiao, S.; Morshed, M. N.; Al Azad, S. Immobilization of cationic titanium dioxide (TiO_2^+) on electrospun nanofibrous mat: synthesis, characterization, and potential environmental application. *Fibers and Polymers* **2018**, *19*, 1715-1725.

(4) Hou, C.; Jiao, T.; Xing, R.; Chen, Y.; Zhou, J.; Zhang, L. Preparation of TiO_2 nanoparticles modified electrospun nanocomposite membranes toward efficient dye degradation for wastewater treatment. *Journal of the Taiwan Institute of Chemical Engineers* **2017**, *78*, 118-126.

(5) Neubert, S.; Pliszka, D.; Thavasi, V.; Wintermantel, E.; Ramakrishna, S. Conductive electrospun PANi-PEO/TiO_2 fibrous membrane for photo catalysis. *Materials Science and Engineering: B* **2011**, *176*, 640-646.

(6) George, S. M. Atomic layer deposition: an overview. *Chem Rev* **2010**, *110*, 111-131.

(7) Shin, S.; Ham, G.; Jeon, H.; Park, J.; Jang, W.; Jeon, H. Atomic layer deposition: overview and applications. *Korean Journal of Materials Research* **2013**, *23*, 405-422.

(8) Peng, Q.; Sun, X.-Y.; Spagnola, J. C.; Hyde, G. K.; Spontak, R. J.; Parsons, G. N. Atomic layer deposition on electrospun polymer fibers as a direct route to Al_2O_3 microtubes with precise wall thickness control. *Nano letters* **2007**, *7*, 719-722.

(9) Du, Q.; Wu, J.; Yang, H. Pt@ Nb-TiO_2 catalyst membranes fabricated by electrospinning and atomic layer deposition. *ACS Catalysis* **2014**, *4*, 144-151.

(10) Kim, S. K.; Hoffmann-Eifert, S.; Reiners, M.; Waser, R. Relation between enhancement in growth and thickness-dependent crystallization in ALD TiO_2 thin films. *Journal of The Electrochemical Society* **2010**, *158*, D6.

(11) Liang, X.; Li, N.-H.; Weimer, A. W. Template-directed synthesis of porous alumina particles with precise wall thickness control via atomic layer deposition. *Microporous and mesoporous materials* **2012**, *149*, 106-110.

(12) Nam, T.; Kim, J. M.; Kim, M. K.; Kim, H.; Kim, W. H. Low-temperature atomic layer deposition of TiO_2, Al_2O_3, and ZnO thin films. *Journal of the Korean Physical Society* **2011**, *59*, 452-457.

(13) Groner, M.; Fabreguette, F.; Elam, J.; George, S. Low-temperature Al_2O_3 atomic layer deposition. *Chemistry of materials* **2004**, *16*, 639-645.

(14) Jurca, T.; Moody, M. J.; Henning, A.; Emery, J. D.; Wang, B.; Tan, J. M.; Lohr, T. L.; Lauhon, L. J.; Marks, T. J. Low-temperature atomic layer deposition of MoS_2 films. *Angewandte Chemie International Edition* **2017**, *56*, 4991-4995.

(15) Xie, Q.; Musschoot, J.; Deduytsche, D.; Van Meirhaeghe, R. L.; Detavernier, C.; Van den Berghe, S.; Jiang, Y.-L.; Ru, G.-P.; Li, B.-Z.; Qu, X.-P. Growth kinetics and crystallization behavior of TiO_2 films prepared by plasma enhanced atomic layer deposition. *Journal of The Electrochemical Society* **2008**, *155*, H688.

(16) Katamreddy, R.; Omarjee, V.; Feist, B.; Dussarrat, C. Ti source precursors for atomic layer deposition of TiO_2, STO and BST. *ECS Transactions* **2008**, *16*, 113.

(17) Hassan, M.; Borgese, L.; Montesanti, G.; Bemporad, E.; Cesarini, G.; Voti, R. L.; Depero, L. E. Atomic layer deposition of semiconductor oxides on electric sail tethers. *Thin Solid Films* **2017**, *621*, 195-201.

Chapter VII Piezoelectric field enhanced photocatalytic efficiency of PVDF/TiO_2 core/shell nanofibrous membrane

Abstract:

Three approaches were applied to prepare polyvinylidene fluoride (PVDF)/titanium dioxide (TiO_2) core/shell composite nanofibrous membranes (CNMs), as described in previous chapters. Here, comparisons of PVDF/TiO_2 CNMs via three approaches were given from the aspects of preparation, morphology, and properties. Additionally, the PVDF/TiO_2 CNM prepared via coaxial electrospinning was applied as piezo-photocatalyst for phenol degradation. The high flow rate of air bubbles enhanced the photocatalytic efficiency of PVDF/TiO_2 CNM under UV irradiation, which was less obvious on PAN/TiO_2 CNM, P25 NPs, and PVDF membrane. When continuous air bubbles in solution flowed and burst, inducing strains on CNM, the piezoelectric field generated on PVDF nanofibers provided a driving force for the photogenerated charge carriers in TiO_2 to move to opposite positions, thus improving the photocatalytic efficiency. It is the first time that the effect of the piezoelectric field on photocatalytic activity was investigated on the PVDF/TiO_2 core/shell CNM.

Keywords: piezo-photocatalysis, core-shell composite nanofibrous membrane, coaxial electrospinning, wastewater treatment.

7.1 Introduction

Many strategies, such as morphology altering, heterojunction formation, doping, and noble metal depositing, have been investigated to enhance the efficiency of photocatalysts, as introduced in Chapter 1.1.1. Piezo-photocatalysis, introducing the piezoelectric effect into photocatalysis, is an emerging and promising strategy to improve catalytic efficiency.[1,2]

Mechanical energy on piezoelectric materials can be converted into electric energy, a phenomenon known as the piezoelectric effect. There are two pathways to improve photocatalytic efficiency with the help of piezoelectric effect. In integrated piezo-photocatalysts, the piezo-potential acts as a built-in field to facilitate the movement of charge carriers and suppress the recombination of charge carriers in the bulk. Enhanced photocatalytic activity via piezoelectric effect has been demonstrated on integrated piezo-photocatalysts in different works, such as ZnO nanowires[3]/nanorods[4], $NaNbO_3$[5], WS_2 monolayer[6]. In hybrid piezo-photocatalysts, the piezo-polarization on piezoelectric material facilitates the movement of charge carriers and suppresses the recombination of electron-hole pairs in the photocatalysts. Furthermore, the piezo-potential causes band bending on the interface of hybrid piezo-photocatalysts, which increases the redox potential. Hybrid piezo-photocatalysts based on inorganic piezo-ceramics (such as CuS/ZnO nanocomposites[7], ZnO@TiO_2 core-shell NFs[8], and ZnO/$BaTiO_3$ heterostructure[9]) and organic piezo-polymers (such as Sn_3O_4/PVDF hybrid film[10] and PVDF-TiO_2 film[11]) have been extensively investigated in piezo-photocatalysis, and the piezoelectric field has a contribution to photocatalytic efficiency. Another feature that needs to be mentioned is that the piezoelectric field is a dynamic electric field under oscillating external vibrations on piezoelectric materials, so it is not screened by free carriers as easily as a static electric field. More detailed introduction on piezo-photocatalysis has been introduced in Chapter 1.3. Therefore, the establishment of piezo-potential through the piezoelectric effect is an ideal strategy for photocatalytic activities.

Despite having low piezoelectric constants, piezoelectric polymers exhibit significant strain under low stress due to the low mechanical quality factor and can be recovered and reused.[10-13] Therefore, hybrid piezo-photocatalysts based on piezo-polymers are becoming promising and effective in the piezo-photocatalytic field. The form of polymer in hybrid photocatalysts has evolved from flat films to microfibrous membranes to nanofibrous membranes with increased surface area and ease of deformation. Notably, for most hybrid piezo-polymer photocatalysts, the photocatalysts are distributed inside the polymer films or fibers, which prevents most photocatalysts from participating in photocatalysis.

Therefore, the core-shell nanofiber membrane, which distributes the photocatalysts outside of nanofiber, is a pursuit of piezo-polymer photocatalysts here. Three approaches for fabricating PVDF/TiO_2 core/shell CNMs were proposed: (I) hydrothermal synthesis combined with electrospinning, in Chapter 4; (II) coaxial electrospinning, in Chapter 5; (III) ALD and hydrothermal annealing combined with electrospinning, in Chapter 6. Comparisons of three PVDF-TiO_2 CNMs are given below:

1) From the perspective of preparation complexity and cost: Approach (II) < Method (I) << Approach (III). Approach (II) is a one-step preparation, hydrothermal synthesis in Approach (I) is a common laboratory technique, while ALD in Approach (III), as a novel and precise deposition technique, it is a more expensive solution.
2) From the perspective of the final morphology: Approach (III) >> Approach (II) > Approach (I). Undoubtedly, ALD in Approach (III) is an ideal technique to deposit a uniform, conformal, and thickness-controlled TiO_2 layer on the dense porous electrospun PVDF membrane. Whereas by the hydrothermal synthesis in Approach (I), a uniform TiO_2 layer was formed on the surface of PVDF NFs near the outer side of the electrospun membrane, and the thickness of TiO_2 decreased with the depth of NFs position in the membrane. For

Approach (II), TiO_2 layer was on the surface of PVDF NF regardless of its position in the membrane.

3) From the photocatalytic activities of PVDF-TiO_2 NFs: Approach (II) > Approach (III) > Approach (I). Within the experimental time of two hours, the PVDF-TiO_2 CNM prepared by Approach (II) was able to completely degrade a 13 mg/L phenol solution, while the CNM obtained by Approach (III) and Approach (I) degraded around 50% phenol and 90% MO in solution, respectively. PVDF-TiO_2 CNM-3 (prepared by Approach (II)) and PVDF/TiO_2-298-4 CNM (prepared by Approach (III)) exhibited similar value on degraded phenol per TiO_2, around 10^6 mol/mg.

Here, the PVDF/TiO_2 core/shell CNM prepared by coaxial electrospinning was considered as the photocatalytic membrane for phenol degradation in order to study the effects of piezo-potential on the photocatalytic efficiency. In addition, PAN/TiO_2 CNM with the same core/shell structure was prepared by coaxial electrospinning using PAN without piezoelectric property as a control group. Then the active species in this piezo-photocatalytic system were evaluated through scavenger experiments.

To the best of the authors' knowledge, it is the first time that the effect of piezoelectric field on the photocatalytic activity was investigated on the PVDF/TiO_2 core/shell CNM. From a broader perspective, this work provides an efficient flexible composite membrane with great capability in converting flowing water energy into piezoelectric potential and improving photocatalytic activity to meet a practical challenge, treating pollutants in the ocean or river with the help of natural resources (solar energy, water wave).

7.2 Experimental section

7.2.1 Materials

PVDF (KYNAR 500) was purchased from Arkema. PAN, titanium dioxide (TiO_2), acetone (ACE), dimethyl sulfoxide (DMSO), phenol, methanol, benzoquinone (BQ), ethylenediaminetetraacetic acid (EDTA), and $AgNO_3$ were purchased from Sigma Aldrich. All reagents were used as received without any further treatment. Deionized water was used throughout the whole experiment.

7.2.2 Preparation of core/shell CNMs

1 g of PVDF powder was added to 6 g solvent mixture of DMSO and ACE with a weight ratio of 2:1 and stirred overnight at room temperature to prepare a 15 wt% PVDF solution. A 5 wt% PAN solution was prepared by dissolving 0.5 g PAN powder in a 10 g solvent mixture of DMSO and ACE (2:1 by weight) and stirring overnight. TiO_2 in DMSO suspension with a concentration of 7% was sonicated for 1 h before use.

PVDF/TiO_2 core/shell CNM or PAN/TiO_2 core/shell CNM were prepared by applying PVDF or PAN solution as a core feed source and TiO_2 suspension as a shell feed source in coaxial electrospinning. The feed rates of core and shell solution/suspension were both 0.5 mL/h. The work voltage and distance here were 12 kV and 15 cm.

The membranes were shacked in water for 15 min and repeated 3 times to remove unfixed TiO_2 NPs from the membrane.

7.2.3 Photocatalytic experiment

The catalytic activity under UV irradiation was monitored by photodegradation of phenol in aquatic solution. The photocatalysts (100 mg PVDF/TiO_2 CNM, 5 mg P25, 100 mg neat-PVDF mat, and 100 mg PAN/TiO_2 CNM) were added into a 150 mL phenol aqueous solution with a concentration of 13 mg L^{-1}. The air bubble was supplied by air flow from the bottom of the reactor, and the flow rate altered the deformation of the membrane. Other operation details remained consistent with Chapter 5.2.4.

7.2.4 Scavenger experiment

Scavenger experiments were performed to find out the active species involved in photocatalysis. Methanol, BQ, EDTA, and $AgNO_3$ were added to the photocatalytic system (kept all the same details as described above) with an initial concentration of 5 mM as scavengers for hydroxyl radical ($^{\cdot}OH$), superoxide radicals ($O_2^{\cdot-}$), holes (h^+) and electrons (e^-), respectively.

7.3 Results and discussion

7.3.1 Characterization

PVDF, a typic piezo-polymer, and PAN, with on piezoelectric effect and poor mechanical properties, were obtained core/shell nanofibers via coaxial electrospinning. PVDF/TiO_2 CNM or PAN/TiO_2 CNM with the same core/shell structure were prepared to investigate the piezo-potential effect on photocatalytic activity, eliminating the influence of the structure.

The SEM images of PVDF/TiO_2 CNM and PAN/TiO_2 CNM were shown in Figure 7.1, from which a distinct TiO_2 layer was observed on the surface of smooth neat-polymer nanofibers. Besides, the actual TiO_2 fraction in PVDF/TiO_2 CNM and PAN/TiO_2 CNM were (17.5 ± 1.6) % and (63.3 ± 4.5) %, respectively. The higher TiO_2 fraction in PAN/TiO_2 CNM than PVDF/TiO_2 CNM should be due to the stronger connection between PAN and TiO_2 as well as the lower density of PAN.

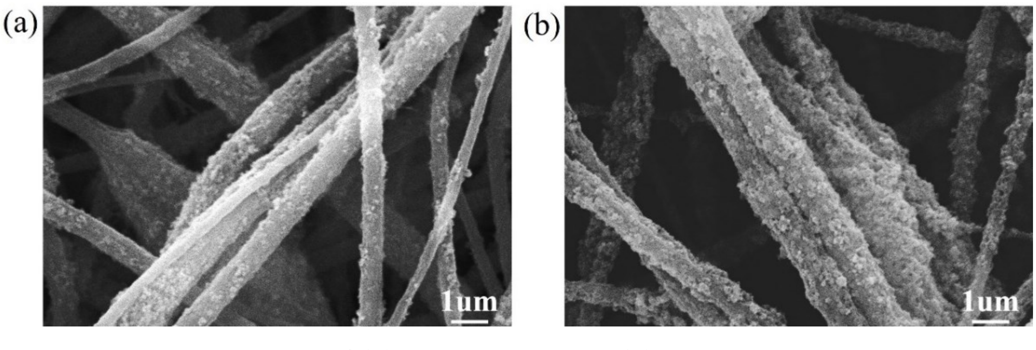

Figure 7.1 SEM images of (a) PVDF/TiO_2 and (b) PAN/TiO_2 core/shell CNMs.

7.3.1 Piezo-photocatalytic activity

The effect of piezo-potential on the phenol degradation was studied to evaluate the piezo-photocatalytic performance of PVDF/TiO_2 CNM prepared via coaxial electrospinning. Figure 7.2 shows the photocatalytic performances of blank (no membrane), neat-PVDF membrane, P25 NPs, PVDF/TiO_2 CNM, and PAN/TiO_2 CNM under UV only, air flow at 2 NL/min (F2) only, UV and air flow at 1 NL/min (UV+F1), as well as UV and air flow at 2 NL/min (UV+F2).

UV-induced degradation occurred in the blank groups. The photocatalytic activities were slower under UV and air flow than under UV only, which might be due to the effect of air bubbles blocking the UV irradiation and/or the reduction in the reaction time related to turbulence. The degradation performances of PVDF, with no photocatalytic behavior and a large surface area, were due to UV-induced degradation and physical absorbance. The photocatalytic activity of PVDF under UV+F2 was slower than that under UV+F1, which was more obvious than that of the blank groups. The inhabitation effect of air bubbles on the photocatalytic activity in the PVDF groups was stronger than the situation in blank groups because air flow blew the PVDF membrane together to block the UV irradiation. Due to the large surface area of P25, 5 mg of P25 caused rapid degradation of phenol under UV and air flow, and higher air flow had a weak contribution to phenol degradation.

PVDF/TiO_2 CNM exhibited faster phenol degradation under UV+F2 than UV+F1, which was the opposite situation in blank and PVDF groups, implying that larger air flow enhanced the photocatalytic activity. The photocatalytic activities of the PAN/TiO_2 CNM are shown in Figure 7.2(e). The performances under UV and under F2 of PAN/TiO_2 CNM were similar to those of PVDF/TiO_2 CNM because of the similar core/shell nanofiber structure. PAN/TiO_2 CNM exhibited faster degradation under UV+F2 than under UV+F1, similar to the P25 and PVDF/TiO_2 CNM groups, but less obvious compared to PVDF/TiO_2 CNM.

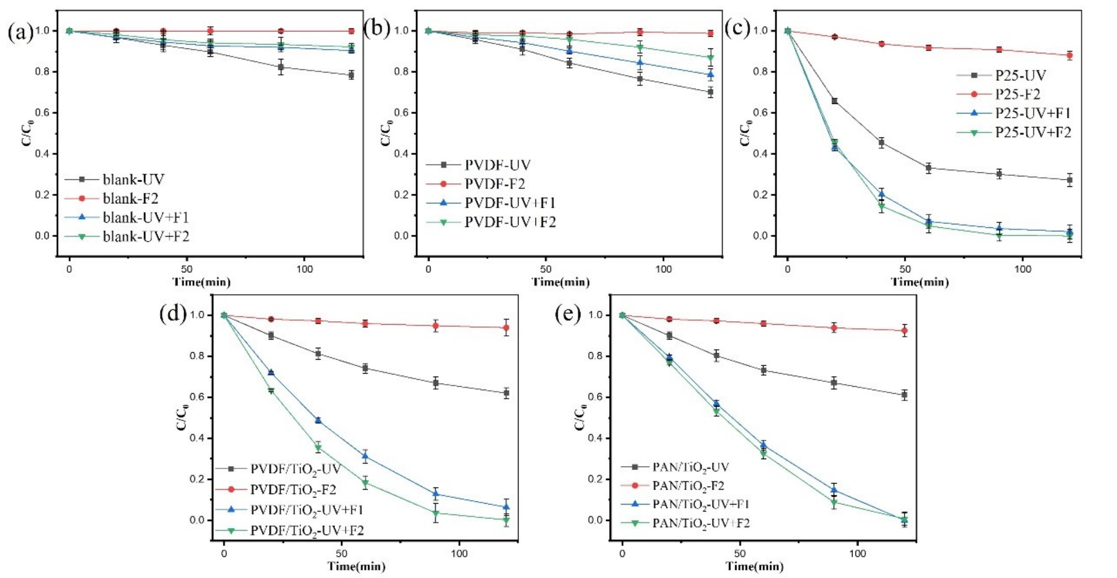

Figure 7.1 Photocatalytic performances of (a) blank, (b) neat-PVDF membrane, (c) P25 NPs, and (d) PVDF/TiO₂ CNM (e) PAN/TiO₂ CNM under UV only, F2 only, UV+F1, and UV+F2.

The degraded phenol per gram of TiO_2 as a function of reaction time was plotted in Figure 7.2(a). After normalizing the TiO_2 mass in CNMs (17.5% and 63.3% TiO_2 fraction in PVDF/TiO_2 and PAN/TiO_2 CNMs, separately), a lower phenol amount was degraded in PAN/TiO_2 CNM than in PVDF/TiO_2 CNM because of higher TiO_2 fraction in PAN/TiO_2 CNM. It can be concluded that only the outer surface of TiO_2 layer on core/shell nanofibers affected phenol degradation, and higher TiO_2 mass in CNMs or thicker TiO_2 layer on the nanofibers had no more contribution to the photocatalytic efficiency, as it was concluded from Chapter 6.3.4.

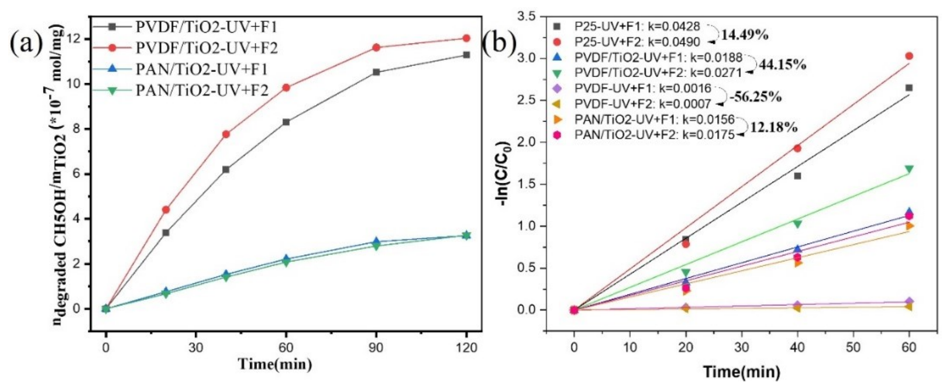

Figure 7.2 (a) The degraded phenol per TiO₂ as a function of reaction time.; (b) scatter plot and linear fit of -ln(C/C₀) versus reaction time (the first one hour) for P25, PVDF/TiO₂ CNM, PVDF, and PAN/TiO₂ CNM under UV+F1 and UV+F2.

Figure 7.2(b) shows scatter plots and linear fits of -ln(C/C_0) versus reaction time (the first one hour) for P25, PVDF/TiO_2 CNM, neat-PVDF, and PAN/TiO_2 CNM under UV+F1 and UV+F2, and the slope of the fitting line was calculated as the corresponding first-order reaction rate constant (k). Under UV+F2, the corresponding k value of P25, PVDF/TiO_2 CNM, PVDF, and PAN/TiO_2 CNM increased by 14.49%, 44.15%, -56.25%, and 12.18% respectively, over the ones under UV+F1. This result suggested that the piezo-potential field generated under air bubbles significantly enhanced the photocatalytic efficiency of PVDF/TiO_2 CNM, which did not occur in no piezo-photocatalytic system (PVDF, P25, and PAN/TiO_2 CNM).

In conclusion, the piezoelectric field was generated on PVDF NFs when continuous air bubbles ruptured in solution and continuously induced strains on CNM, as well as the higher piezoelectric field generated at a higher flow rate of air bubble led to a more efficient photocatalytic efficiency of PVDF/TiO_2 CNM. Hence, piezo-potential had an attribution on photocatalytic performance.

The photocatalysis and piezo-photocatalysis mechanisms of PVDF/TiO_2 CNM are shown in Figure 7.3. For photocatalysis, the electrons jump from the valence band (VB) to the conductive band (CB) under UV irradiation, leaving holes in the VB, and then the electrons and holes migrate to the surface of TiO_2 NPs for reduction and oxidation reactions. The relatively low degradation efficiency is due to the low mobility of charge carriers and the high recombination rate between electron and hole.

For piezo-photocatalysis, the PVDF core can generate piezoelectric potential under the strain from the bubble reputation, which provides a driving force for the migration of photo-generated electrons in TiO_2 shell to the positive piezo-potential interface and the movement of photo-generated holes to the opposite direction. In this case, the mobility of charge carriers is accelerated and the recombination between electrons and holes is inhibited. Furthermore, the accumulation of electrons and holes at different sites causes the band bending of TiO_2, which can increase the redox potential. Therefore, the photocatalytic efficiency of TiO_2 NPs is enhanced by the presence of the built-in piezoelectric field on PVDF. Another feature of piezo-photocatalysis is that the piezoelectric field is a dynamic electric field and is not easily screened by the free carriers as a static electric field, hence the piezo-photocatalysis is a long-term active strategy in the photocatalytic field.

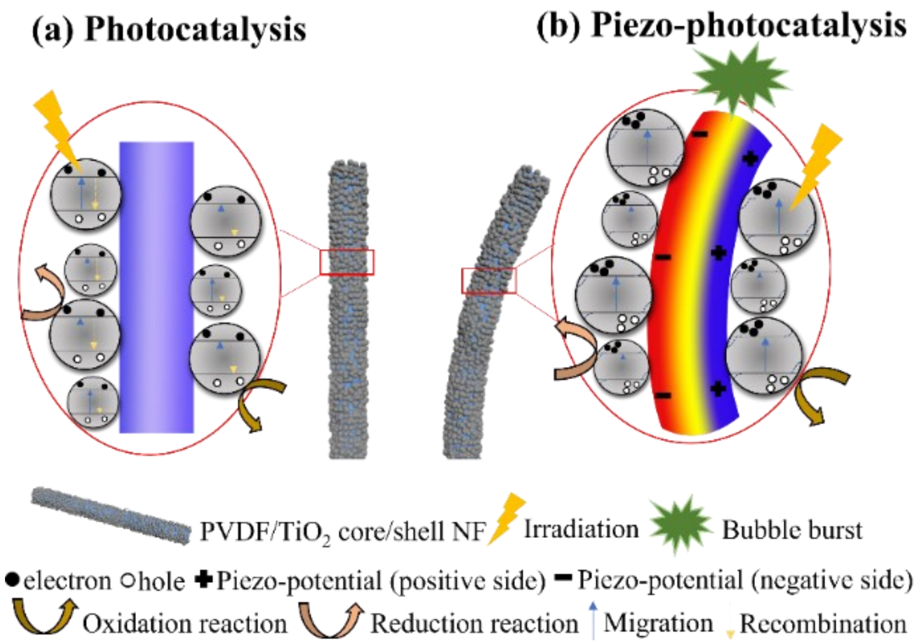

Figure 7.3 Schematic illustration showing the (a) photocatalytic process and (b) piezo-photocatalytic process of PVDF/TiO_2 core/shell NF.

7.3.2 Scavenger activity

To explore the active species for the phenol degradation in this piezo-photocatalytic system, quenching experiments were conducted by adding scavengers (methanol, BQ, EDTA, and $AgNO_3$) to the photocatalytic solution.[14,15] According to the quenching results in Figure 7.4, 37%, 59%, 26%, and 69% phenol was degraded with the addition of methanol, BQ, EDTA, and $AgNO_3$, which acted as the scavenger of hydroxyl radical ($^{\cdot}OH$), superoxide radical ($O_2^{\cdot-}$), hole (h^+), and electron (e^-), separately. It meant that these common active species had a role in the piezo-photocatalytic degradation process, as well as $^{\cdot}OH$ and h^+ were the main active species.

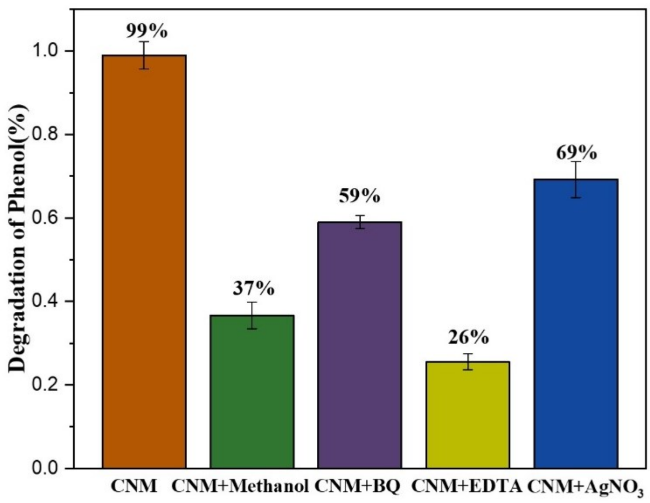

Figure 7.4 Scavenger experiment results during the piezo-photocatalytic degradation of phenol over PVDF/TiO_2 core/shell CNM.

7.4 Conclusion

The photocatalytic efficiency of PVDF/TiO_2 core/shell CNM prepared by coaxial electrospinning under UV+F2 was enhanced by 44% based on the one under UV+F1 because of the piezo-potential generated on the PVDF core. While only 14.49% and 12.18% enhancement in this situation was reached on P25 and PAN/TiO_2 CNM, respectively. Furthermore, h^+, $^{\cdot}OH$, $O_2^{\cdot-}$, and e^- played a role, as the active species, in the piezo-photocatalytic system for the degradation of phenol.

This work confirmed the piezoelectric potential generated on the piezoelectric PVDF core by the flowable water did contribute to the photocatalytic efficiency. The flexible composite membrane possesses a high photocatalytic ability, a sustainable ability, and a manipulative state, and has the potential to treat pollutants in a realistic water environment.

References

(1) Tu, S.; Guo, Y.; Zhang, Y.; Hu, C.; Zhang, T.; Ma, T.; Huang, H. Piezocatalysis and piezo - photocatalysis: catalysts classification and modification strategy, reaction mechanism, and practical application. *Advanced Functional Materials* **2020**, *30*, 2005158.

(2) Pan, L.; Sun, S.; Chen, Y.; Wang, P.; Wang, J.; Zhang, X.; Zou, J. J.; Wang, Z. L. Advances in piezo - phototronic effect enhanced photocatalysis and photoelectrocatalysis. *Advanced Energy Materials* **2020**, *10*, 2000214.

(3) Xue, X.; Zang, W.; Deng, P.; Wang, Q.; Xing, L.; Zhang, Y.; Wang, Z. L. Piezo-potential enhanced photocatalytic degradation of organic dye using ZnO nanowires. *Nano Energy* **2015**, *13*, 414-422.

(4) Bai, Y.; Zhao, J.; Lv, Z.; Lu, K. Enhanced piezo-phototronic effect of ZnO nanorod arrays for harvesting low mechanical energy. *Ceramics International* **2019**, *45*, 15065-15072.

(5) Singh, S.; Khare, N. Coupling of piezoelectric, semiconducting and photoexcitation properties in $NaNbO_3$ nanostructures for controlling electrical transport: realizing an efficient piezo-photoanode and piezo-photocatalyst. *Nano Energy* **2017**, *38*, 335-341.

(6) Thakur, D.; Sharma, M.; Vaish, R.; Balakrishnan, V. WS_2 monolayer for piezo–phototronic dye degradation and bacterial disinfection. *ACS Applied Nano Materials* **2021**, *4*, 7879-7887.

(7) Hong, D.; Zang, W.; Guo, X.; Fu, Y.; He, H.; Sun, J.; Xing, L.; Liu, B.; Xue, X. High piezo-photocatalytic efficiency of CuS/ZnO nanowires using both solar and mechanical energy for degrading organic dye. *Acs Appl Mater Inter* **2016**, *8*, 21302-21314.

(8) You, H.; Wu, Z.; Jia, Y.; Xu, X.; Xia, Y.; Han, Z.; Wang, Y. High-efficiency and mechano-/photo-bi-catalysis of piezoelectric-ZnO@ photoelectric-TiO_2 core-shell nanofibers for dye decomposition. *Chemosphere* **2017**, *183*, 528-535.

(9) Zhou, X.; Wu, S.; Li, C.; Yan, F.; Bai, H.; Shen, B.; Zeng, H.; Zhai, J. Piezophototronic effect in enhancing charge carrier separation and transfer in ZnO/$BaTiO_3$ heterostructures for high-efficiency catalytic oxidation. *Nano Energy* **2019**, *66*, 104127.

(10) Han, S.; Chen, D.; Wang, J.; Liu, Z.; Liu, F.; Chen, Y.; Ji, Y.; Pang, J.; Liu, H.; Wang, J. Assembling Sn_3O_4 nanostructures on a hydrophobic PVDF film through metal-F coordination to construct a piezotronic effect-enhanced Sn_3O_4/PVDF hybrid photocatalyst. *Nano Energy* **2020**, *72*, 104688.

(11) Dong, C.; Fu, Y.; Zang, W.; He, H.; Xing, L.; Xue, X. Self-powering/self-cleaning electronic-skin basing on PVDF/TiO_2 nanofibers for actively detecting body motion and degrading organic pollutants. *Applied Surface Science* **2017**, *416*, 424-431.

(12) Dai, B.; Huang, H.; Wang, W.; Chen, Y.; Lu, C.; Kou, J.; Wang, L.; Wang, F.; Xu, Z. Greatly enhanced photocatalytic activity by organic flexible piezoelectric PVDF induced spatial electric field. *Catalysis Science & Technology* **2017**, *7*, 5594-5601.

(13) Durairaj, A.; Ramasundaram, S.; Sakthivel, T.; Ramanathan, S.; Rahaman, A.; Kim, B.; Vasanthkumar, S. Air bubbles induced piezophotocatalytic degradation of organic pollutants using nanofibrous poly (vinylidene fluoride)-titanium dioxide hybrid. *Applied Surface Science* **2019**, *493*, 1268-1277.

(14) Li, Z.; Meng, X. New insight into reactive oxidation species (ROS) for bismuth-based photocatalysis in phenol removal. *Journal of Hazardous Materials* **2020**, *399*, 122939.

(15) Pelaez, M.; Falaras, P.; Likodimos, V.; O'Shea, K.; Armah, A.; Dunlop, P. S.; Byrne, J. A.; Dionysiou, D. D. Use of selected scavengers for the determination of NF-TiO_2 reactive oxygen species during the degradation of microcystin-LR under visible light irradiation. *Journal of Molecular Catalysis A: Chemical* **2016**, *425*, 183-189.

Chapter VIII Conclusions

8.1 Summary

This work focused on the preparation of PVDF/TiO_2 composite membranes as piezo-photocatalysts and the investigation of the effect of the piezoelectric field on photocatalytic activity. The PVDF/TiO_2 core/shell composite nanofiber membrane (CNM) was proposed here to obtain good contact between PVDF core and TiO_2 shell (achieved by core/shell structure), to reach the recovery and reuse of photocatalyst (achieved by using polymer, PVDF, as support), to maintain a large effective surface area (achieved by means of nanofiber membrane form).

In Chapter 3, the effects of solvents and electrospinning parameters on morphology, structure, and piezoelectric properties of PVDF nanofibrous membranes were studied: when DMSO/ACE (2/1) with high dipole moment was used as the solvent, PVDF electrospun membrane exhibited a higher crystallinity, β-phase fraction, and piezoelectric output than those prepared using DMSO/THF (1/2) with a low dipole moment. Therefore, the solvents with a high dipole moment can enhance piezoelectric properties, while the evaporation rate and solvent conductivity of solvent can influence nanofiber diameter. Besides, electrospinning parameters can also control nanofiber diameter and piezoelectric properties during the electrospinning process.

In Chapter 4, PVDF-TiO_2 core-shell CNMs were obtained through microwave-assisted hydrothermal synthesis of TiO_2 on electrospun PVDF membrane, and the effects of hydrothermal process parameters on the structure and photocatalytic activity were studied: a smooth TiO_2 outer layer uniformly covered the PVDF nanofiber core when the precursor solution acidity was 2 M; the highest TiO_2 anatase fraction was obtained at 120 °C, and the anatase crystal size and fraction were affected by treatment time. Overall, the PVDF-TiO_2 CNM exhibited the best photocatalytic performance for MO degradation when the hydrothermal parameter was 120 °C-2 h-2 M.

In Chapter 5, PVDF/TiO_2 core/shell CNMs were prepared by coaxial electrospinning method adopting PVDF solution and P25 suspension as core and shell feed sources. Directly using P25, a commercial TiO_2 (80% anatase and 20% rutile), achieved excellent photocatalytic activity. One-step preparation of PVDF/TiO_2 core/shell CNMs via coaxial electrospinning was simple, cost-effective, and without damage to PVDF. Based on the blank under UV+F2, around 75% phenol was degraded due to the existence of PVDF/TiO_2 CNM.

In Chapter 6, atomic layer deposition (ALD) was applied to grow the TiO_2 layer on the surface of the PVDF NF membrane, and post-treatment annealing was employed to improve the crystal structure of TiO_2. A uniform and thickness-controllable TiO_2 layer was grown on electrospun PVDF NFs via ALD. The PVDF/TiO_2 core/shell CNMs after hydrothermal annealing at 140 °C for 4 h, which crystallized TiO_2 and avoided PVDF damage, had 40% phenol degradation improvement based on the PVDF/TiO_2 core/shell CNM before annealing. For PVDF/TiO_2 core/shell CNMs with different TiO_2 thicknesses, they had similar photocatalytic performances.

In Chapter 7, the PVDF/TiO_2 core/shell CNM prepared via coaxial electrospinning in Chapter 6, with the easiest preparation and the best photocatalytic performance, was applied to investigate the effect of piezo-potential on photocatalytic activity. The piezo-photocatalytic efficiency of PVDF/TiO_2 core/shell CNM under UV+F2 was enhanced by 44% based on the one under UV+F1. It confirmed the piezo-potential generated on PVDF core under the flowable water did have a contribution to the photocatalytic efficiency. In addition, h^+, $^{\cdot}OH$, $O_2^{\cdot-}$, and e^- played a role, as the active species, in this piezo-photocatalytic system for the degradation of phenol.

8.2 Future perspectives

There is much room for the development of piezoelectric photocatalysis, which are, but not limited to, considered from these perspectives:

- Monolayer TiO_2 on the surface of PVDF NFs can be prepared via ALD with a low cycle number. What is the effect of TiO_2 layer thickness on piezo-photocatalysis of PVDF/TiO_2 core/shell CNM? With the thinner TiO_2 layer, will the piezo-potential on the PVDF core have a higher contribution to photocatalytic performance?

- The mechanism of piezo-photocatalysis needs to be further elucidated and uncovered. The piezoelectric potential in piezoelectric materials is a driving force for facilitating the migration of charge carriers in photocatalysts. But what is the relation between the generated potential and piezoelectrically enhanced photocatalytic activity? Is there true band bending on semiconductors when the piezoelectric potential exists? Can piezoelectric materials or photocatalytic materials have any characteristics to prove the piezo-photocatalytic effect? …… Therefore, more efforts should be devoted to in-situ characterizations, simulations, and theoretical calculations to reveal more details about the piezo-photocatalytic mechanism.
- Improve the energy utilization from mechanical energy to chemical energy during piezo-photocatalysis. For the recent studies, the directions of the stress applied on piezo-photocatalysts were random, resulting in a relatively low piezo-potential and a weak piezo-photocatalytic effect. If the direction of stress is similar to the polarization direction, the piezo-potential generated on the piezo-photocatalyst can be enhanced. More strategies can be carried out from this aspect to enhance the piezo-photocatalytic effect.
- Develop practical applications of piezo-photocatalysts. The main applications in piezo-photocatalysis are pollutant degradation and water splitting, and they are laboratory-scale experiments. A possible practical application of piezo-photocatalysts is water remediation, where solar provides irradiation and water waves applies stress/stain on piezo-photocatalysts. Other applications should be pursued to make piezo-photocatalysis a useful and practical solution.

Academic activities related to this thesis

Abroad study:

Institut National des Sciences Appliquées de Lyon (INSA Lyon), March-June 2022 (four months), Supervisor: Lecturer Guilhem Rival

Publications:

1. **Yin, Jiayi**, et al. "PVDF-TiO_2 core-shell fibrous membranes by microwave-hydrothermal method: preparation, characterization, and photocatalytic activity." *Journal of Environmental Chemical Engineering* (2021): 106250.
2. **Yin, Jia-Yi**, et al. "Effects of Solvent and Electrospinning Parameters on the Morphology and Piezoelectric Properties of PVDF Nanofibrous Membrane." *Nanomaterials* 12.6 (2022): 962.
3. **Yin, Jia-Yi**, et al. " Piezoelectric field enhanced photocatalytic efficiency of PVDF/TiO_2 core/shell nanofibrous membrane via coaxial electrospinning.", submitted.

Conference:

2022 MRS Spring Meeting & Exhibit, "A Flexible Piezoelectric PVDF-TiO_2 Nanofibrous Membrane for Intelligent Photocatalytic Performance", Conference, Oral Presentation